Swansea University
Prifysgol Abertawe

Cronfa
Setting Research Free

Swansea University E-Theses

Environmentally assisted fatique crack development in aluminium-based metal matrix composites.

Shields, Julia Diane

How to cite:

Shields, Julia Diane (2003) *Environmentally assisted fatique crack development in aluminium-based metal matrix composites..* thesis, Swansea University.
http://cronfa.swan.ac.uk/Record/cronfa42436

Use policy:

This item is brought to you by Swansea University. Any person downloading material is agreeing to abide by the terms of the repository licence: copies of full text items may be used or reproduced in any format or medium, without prior permission for personal research or study, educational or non-commercial purposes only. The copyright for any work remains with the original author unless otherwise specified. The full-text must not be sold in any format or medium without the formal permission of the copyright holder. Permission for multiple reproductions should be obtained from the original author.

Authors are personally responsible for adhering to copyright and publisher restrictions when uploading content to the repository.

Please link to the metadata record in the Swansea University repository, Cronfa (link given in the citation reference above.)

http://www.swansea.ac.uk/library/researchsupport/ris-support/

Environmentally Assisted Fatigue Crack Development in Aluminium-based Metal Matrix Composites.

J. D. Shields
B. Eng. (Hons.) M.Phil.

Interdisciplinary Research Centre,
Department of Materials Engineering,
Swansea University.

UNIVERSITY OF WALES SWANSEA
LIBRARY

ProQuest Number: 10798144

All rights reserved

INFORMATION TO ALL USERS
The quality of this reproduction is dependent upon the quality of the copy submitted.

In the unlikely event that the author did not send a complete manuscript
and there are missing pages, these will be noted. Also, if material had to be removed,
a note will indicate the deletion.

ProQuest 10798144

Published by ProQuest LLC (2018). Copyright of the Dissertation is held by the Author.

All rights reserved.
This work is protected against unauthorized copying under Title 17, United States Code
Microform Edition © ProQuest LLC.

ProQuest LLC.
789 East Eisenhower Parkway
P.O. Box 1346
Ann Arbor, MI 48106 – 1346

DECLARATION

This work has not been accepted in substance for any degree and is not being concurrently submitted in candidature for any degree.

Signed.....

Date 21/03/03

STATEMENT 1

This thesis is the result of my own investigations, except where otherwise stated. Other sources are acknowledged by explicit references. A bibliography is appended.

Signed. .....

Date 21/03/03

STATEMENT 2

I hereby give consent for my thesis, if accepted, to be available for photocopying and for inter-library loan, and for the title and summary to be made available to outside organisations.

Signed. .....

Date 21/03/03

Abstract.

Aluminium alloys have been used successfully in a variety of commercial systems due to their unusual combination of properties. These include low density, good corrosion resistance and excellent mechanical properties. However, they also have disadvantages which include a low resistance to fracture and fatigue under load. The addition of reinforcing particles improves these properties, but it may also upset the delicate balance which has been achieved over many years of fine tuning.

This study addresses the areas of uncertainty concerning environmental sensitivity in a leading aluminium based silicon carbide particle reinforced metal matrix composite, under conditions of direct interest to the aerospace industry. The materials studied are 2XXX series aluminium alloys, AMC225, mechanically alloyed and powder blended conditions. The environments to which they have been subjected include immersion in 3.5% sodium chloride solution, from zero to 72 hours and a fog atmosphere of the same composition.

It has been found that soaking the materials in this salt solution has a significant detrimental effect on fatigue performance, even after relatively short soaks of 8 hours. The LCF performance is independent of processing route in the T4 condition alloys. Lives to failure are dramatically reduced on the introduction of a saline environment, in which the process of corrosion pitting is implicated.
Sensitivity to a salt fog environment is independent of waveform frequency.
A "long crack" trend has been defined for $\Delta K > 8 MNm^{-3/2}$, which corresponds to the Paris regime, with Paris exponents of $m=3.57$ and $c=3.49 \times 10^{-11}$.

Contents

Part 1. Literature Review

Chapter 1

Chapter 2

Chapter 3

Chapter 4

Chapter 5

Part 2. Aims

Part 3. Experimental Procedures.

Part 4. Results.

Part 5. Discussion.

Part 6. Conclusions.

Part 7. Further Work.

Part 8. References.

CHAPTER 1.

1. Metal Matrix Composites.

A composite may be defined as a heterogeneous mixture of two or more homogeneous phases which have been bonded together.

Composites are generally categorised by their matrix material, of which the three major types are ceramic, polymer and metal. They may then be sub-categorised by the reinforcement geometry (particulate, whisker or fibre) and overall composition (polymer-polymer, metal-ceramic or other combinations of matrix-reinforcement).

Metal matrix composites (MMC's) are classified by the type of reinforcement and the matrix material itself, which as its name suggests is a metal or alloy. The reinforcement material is generally a ceramic.

1.1 The Matrix Material.

The matrix material is chosen for it's load bearing properties, resistance to fatigue, light weight, toughness and corrosion resistance(1). Typical choices for these materials include titanium, aluminium and magnesium alloys, as well as copper, lead and iron to a lesser degree. The most common of these however is aluminium due to its remarkable combination of good corrosion resistance, low density and exceptional mechanical properties.

Of particular interest in this project are the 2XXX series wrought aluminium alloys. Most aluminium alloys corrode at a higher rate during their first twelve months of exposure to the atmosphere, during which time the protective oxide layer will thicken and slow the rate of attack. For the case of the 2XXX series alloys, the rate does not decrease. This

peculiarity is also evident when the 2XXX series alloys are immersed in water as, unusually for aluminium alloys, they do not exhibit good corrosion resistance. Impurities in the water may also degrade the corrosion resistance of these alloys. They are particularly sensitive to the presence of chloride particles, as will be discussed later.

Another factor of significance when selecting a matrix material is the effect the reinforcement addition may have on its properties. The properties of aluminium alloys have been refined by small changes in their alloying elements over a long period of fine tuning. It should be of some concern that the addition of a reinforcing phase may disrupt this fine balance.

1.2 Reinforcement Material.

The choice of reinforcement material is not so obvious.

One of the key properties in design is stiffness or rigidity. The material property related to this feature is the 'specific modulus' which is the elastic modulus divided by the density. Engineering materials such as steel, aluminium and titanium, have similar specific moduli, whereas organic materials have lower modulus to density ratios. This has meant that, to gain bending stiffness without excessive weight, designs using lower density materials must increase the section size.

Boron and carbon, which are covalently bonded, have significantly higher specific moduli than conventional engineering materials. Boron carbide and silicon carbide also have high fractions of covalent bonding and therefore, also high specific moduli.

Other properties for which the reinforcement material is chosen include, tensile strength, density, melting temperature, thermal stability, compatibility with the matrix material, the coefficient of thermal expansion, size and shape, and most importantly cost.

These materials however, are very brittle, and cannot be manufactured in large sections. Their brittleness also makes them highly sensitive to cracks and flaws and weak in large sections. In fact, unless high strength is also attained, these materials cannot be used in

engineering structures. The necessity for strength and toughness under tensile loading, together with reproducibility of properties are the reasons that metal alloys are accepted as the prime materials for large dynamic structures. It seems apparent, therefore, to combine these two classes of material in some way, in order to amalgamate the best properties of each, with the minimum of their disadvantages.

Improved response to dynamic loads in composite materials is obtained by absorbing the loads with the elastic member of the composite rather than the plastic (ductile metal) member, which would undergo cumulative damage. Reduced crack sensitivity is obtained by redirecting cumulative damage in the material in directions that do not reduce the load carrying ability. The composite system is designed to take advantage of the high specific moduli of covalent materials and to minimise the effect of cumulative damage in inelastic solids under dynamic loading conditions which lead to failure.

The recent development of high purity silicon carbide[2,3,4], which can be produced in various ways, including the pyrolysis of rice husks, has lead to significant engineering interest although the importance of carbon (in the form of graphite), boron and alumina reinforcements should not be overlooked.

1.3 Reinforcement Geometry.

In discussing the reinforcement, it is also important to consider the geometry of the ceramic additions. The three major types of reinforcement shape are long or continuous fibre reinforcements, short fibre or whisker reinforcement and particulate reinforcements, as illustrated in figure 1. Each has its own unique set of advantageous and disadvantageous properties.

1.3.1 Continuous Fibre Reinforcement.

Currently, a wide range of long or continuous fibres, suitable for incorporation with aluminium alloys, are available including boron, silicon carbide, alumina fibre and

graphite fibres[5]. Continuous fibre reinforcement improves many properties of aluminium alloys, but is complex and expensive to fabricate, some of the production routes are discussed later in this chapter.

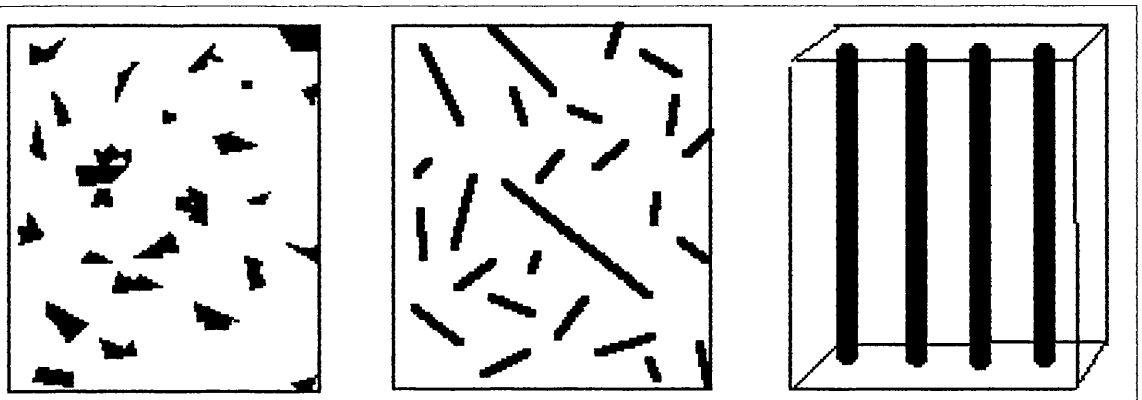

Figure 1.

Continuous fibre reinforced metals are often compared to carbon fibre reinforced plastics (CFRP's). The specific stiffness values of MMC's are significantly superior to those of polymer composites[5]. However, relatively poor transverse strength, coupled with their higher density results in the MMC's exhibiting comparatively inferior specific tensile strengths.

This highlights another disadvantage of fibre reinforced materials. Increases in stiffness, tensile strength, shear strength and Poison's ratio are achieved in the fibre direction. The partial contributions of the fibre and the matrix are approximated by the rule of mixtures;

$$\sigma_{cl} = v_p.\sigma_f + (1 - v_p).\sigma_m$$

where,

σ_{cl} = material tensile strength,

v_p = fibre volume fraction,

σ_f = fibre tensile strength,

σ_m = matrix tensile strength.

This is accurate for the longitudinal direction, but not for the transverse sections, where the matrix carries the brunt of the load and the fibres effectively reduce the load bearing area. This results in the transverse properties being approximately equal to the matrix alloy tensile properties. In other words, significant anisotropy is apparent in the material properties according to the direction in which the fibres are placed.

1.3.2. Whiskers or short fibre reinforcement.

In considering the inhomogeneous response associated with both whisker and particulate strengthened metal matrix composites, several factors must be examined, these include; aspect ratio, morphology and orientation. Possible strengthening mechanisms for these materials include;

- high dislocation densities generated by differences in coefficients of thermal expansion, which in the case for aluminium alloys and silicon carbide can be as great as a factor of 10. Where, Al=23.6*10^{-6}/^{0}C and SiC whisker=2.3*10^{-6}/^{0}C[6].
- small subgrain size as a result of high dislocation densities[7,8]
- residual elastic stress
- differences in texture
- load transfer which is the classical composite strengthening mechanism
- dispersion strengthening.

The difference in coefficients of thermal expansion results in the particle being in compression, and the matrix in tension, these stresses may even exceed the matrix yield strength[9].

In whisker reinforced materials, the major stiffening and strengthening mechanisms in operation are the high dislocation density and the impedance of subgrain growth by the fibres[8]. The dislocation density is dependent on the morphology of the reinforcement phase, but has no effect on the matrix dependent composite stiffness and stress/strain response.

Whisker reinforcement offers enhanced mechanical properties over particulate strengthening only when the aspect ratio (length to diameter ratio) is above a critical value, given by[10],

$$l/D_{crit} = 10,$$

defined by; $l/D_{crit} = \sigma_{uf}/2\tau_m,$

where, l = length

D = diameter

σ_{uf} = ultimate fibre strength

and $2\tau_m$ = matrix shear strength.

If the whiskers are damaged during processing such that this aspect ratio is less than 10 then the benefits are lost. As a result, more care must be exercised in the manufacture of whisker strengthened MMC's than for particulate strengthened MMC's, increasing the price of these materials.

1.3.3 Particulate Strengthening.

This programme focuses on particulate strengthened composites. These include composites with a large volume fraction (typically of the order of 20% or greater) of hard reinforcing dispersed phase, but not the class of dispersion hardened metals which have a considerably lower volume fraction of dispersoid. In addition, the particle diameter and the interpartical spacing are much greater in composites, typically 1μm as opposed to 0.01-0.1μm distances used in dispersion hardened alloys.

Particulate reinforcement, being three dimensional, can produce isotropic properties since symmetry along the three orthogonal planes can be obtained. This, however, does

not assure homogeneity as indeed, the properties are not only sensitive to the constituent properties, but also very sensitive to the interfacial properties and the distribution of the reinforcement.

The strength of particulate composites is dependent on the diameter of the particles, inter particle spacing and the volume fraction of the reinforcement, and the matrix material, especially the work-hardening coefficient which increases the effectiveness of the reinforcement.

The mechanical properties of aluminium alloys can be improved by strengthening mechanisms at elevated and ambient temperatures. These improvements are dependent on solution heat treatment, aging and the dispersion and morphology of the reinforcements. The enhancements include increases in elastic moduli, proof stress, tensile strength and wear resistance, with the additional ability to tailor the coefficient of thermal expansion and damping characteristics.

1.4 Interface Properties.

Resin based materials now have an historical, widespread recognition and acceptance, mainly due to their relative ease of manufacture and comparatively cheap price. This is not true however for carbon fibre reinforced materials.

In the case of metal composites the temperature of fabrication is greater than that generally used in the fabrication of polymer/resin based composites and the elastic modulus coefficients are one or two orders of magnitude greater. Thus both mechanical (stress) and chemical compatibility are much more serious problems.

It is important to mention that there must be some interaction between the two components to allow a good bond between them, so wetting should be promoted. However, it is also recognised that control over the chemical reactions is necessary.

Chemical compatibility problems in metal composites can be overcome in two ways, either by using low temperature (solid state) fabrication techniques or by selecting thermodynamically stable component phases that are in equilibrium with each other.

Another consideration to be taken into account is the chemical compatibility between the matrix and the reinforcement.

"Excessive interaction can lead to undesirable stable interfacial compounds. With respect to SiC particle reinforced aluminium composites, four hypothesis have been proposed concerning this interface reaction:

i) An SiO_2 layer forms at the interface.

ii) An Al_4C_3 film forms at the interface.

$$3SiC + 4Al \Rightarrow Al_4C_3 + 3Si$$

iii) The interface is formed by adhesion between the SiC and aluminium.

iv) $SiCuAl_2$ forms at the interface, but also at the grain boundaries".

It has been reported that exercising proper control will effect the formation of a very strong interfacial bond.(*11,12*)

For case ii), the addition of excess silicon to the melt will reduce the formation of Al_4C_3(*11*).

In low silicon alloys, if the melt exceeds 710^{0}C, Al_4C_3 formation occurs. The reason this compound is undesirable is that it increases the viscosity, reduces corrosion resistance and degrades the mechanical properties of the casting. Excessive formation of Al_4C_3 renders the melt unusable."(*10*).

The problem caused by thermal mismatch can be addressed by selecting a reinforcement phase with a similar coefficient of thermal expansion or by using a ductile matrix which yields up all the differential strain necessary in thermal cycling.

1.5 Advantages of Metal Matrix Composites.

Metal matrix composites have several advantages which outweigh these processing problems and are significant in their utilisation as structural materials. These advantages relate to the same metallic properties which have lead to the general primacy of metal alloys for use in engineering. They include a combination of the following;

- high strength
- high modulus
- high toughness and impact properties
- low sensitivity to thermal shock and changes in temperature
- high surface durability and low sensitivity to surface flaws
- high electrical and thermal conductivity
- excellent reproducibility of properties
- excellent technological background with respect to;
  a) design
  b) manufacture
  c) shaping and forming
  d) joining
  e) finishing
  f) service durability information.

1.6 Processing Techniques.

The production routes for MMC's are determined by the type of reinforcement phase. The mechanical aspects, such as blending, being defined by the reinforcement geometry and the thermal aspects, such as melt temperature, being defined by the composition of the reinforcement and its compatibility with the matrix material.

Manufacturing techniques used to fabricate continuous fibre MMC's are numerous, including diffusion bonding of plasma monotapes, liquid metal infiltration of a fibre preform, hot pressing of melt infiltrated fibre rows, electrochemical plating, hot rolling of fibre arrays and metal foils, and explosive welding. Of these, the first three are the most widely used production methods with diffusion bonding and hot pressing being employed for sheet or simple tubes and liquid metal infiltration techniques for more complex three dimensional components.

For bonding of plasma monotapes, monotapes are produced by coating fibre mats in the

matrix material, generally by a deposition process, such as vacuum plasma spraying, chemical coating, electrochemical coating, chemical vapour deposition, or physical vapour deposition. The matrix binds the tape into a monotape of adequate thickness, which is then stacked and compressed into a sufficiently dense composite.

There are two similar solid state fabrication methods, matrix coated fibres (MCF) and foil-fibre-foil (FFF)[61].

The MCF method involves fibres coated with the matrix material being stacked as required and consolidated by diffusion bonding processes.

The FFF process entails the consolidation of alternating layers of matrix foil and fibre mats made with aligned monofilament fibres. It should be noted that before foil-fibre assembly, the foil should be thoroughly cleansed of oxides and contaminants, to ensure good bonding between the two materials[5,61].

Generally, a composite produced by these methods is not fully dense at this stage and a final consolidation process is required to remove porosity and gaps between fibre and foil. This is usually carried out by diffusion bonding under a hot press or hot isostatic press.

1.6.1 Processing Techniques Used for Discontinuously Reinforced MMC's.

These two types of reinforcement tend to have the same or similar processing techniques, although some are less suitable than others for whisker strengthened materials as whisker damage during processing needs to be avoided.

Discontinuously reinforced materials are generally fabricated using a rapid solidification process as this allows different compositions from the equilibrium and composition ranges of the phases formed, resulting in microstructurally and compositionally flexible materials, so a range of properties is available for any one group of MMC's[5]. As Rohatgi et al[14] stated 'rapidly solidified composites possess a much smaller dendrite size and fewer SiC particles in each interdendritic boundary, resulting in a more homogeneous distribution. Rapidly solidified structures therefore give the best particle distribution due

to finer dendrite size and limited particle settling'.

These rapid solidification processes can be divided into three major categories according to the temperature of the metal matrix during processing:

- Solid phase processes.
- Liquid phase processes.
- Two phase (solid/liquid) processes.

This report focuses on the solid phase processes.

There are three key processes for particulate reinforced metal matrix composite fabrication in the solid phase: ingot metallurgy, powder metallurgy and mechanical alloying[61].

Ingot metallurgy involves the mixing of the reinforcement with molten metal followed by casting.

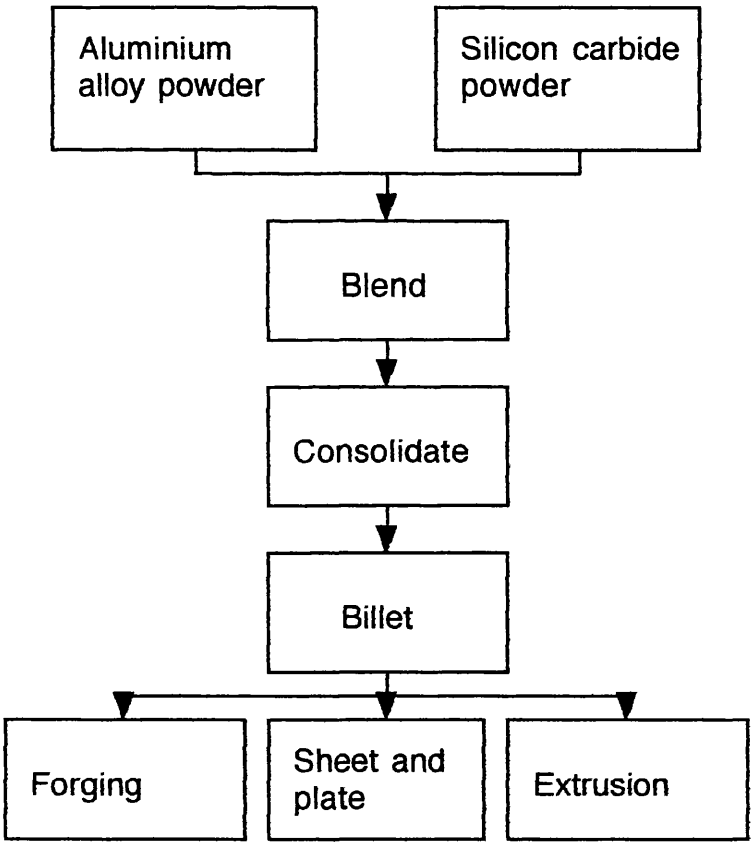

Figure 2. Powder metallurgy route.

The powder metallurgy route is summarised in figure 2. The ceramic is blended with the oxide free, pre-alloyed powder, canned, degassed and consolidated in a billet either by hot pressing or hot isostatic pressing. This process should be carefully monitored as

SiC fracture can occur at comparatively low strains as the compaction temperature is increased[15,16]. It is then extruded or forged into the required geometry. This process usually turns out billets, so secondary processing is often necessary in the form of extrusion, rolling or forging, to obtain the required geometry. It has been found[13] that although the particles are aligned in the extrusion direction, the distribution remains homogeneous. One of the advantages of this method is the ability to exploit the improved properties of advanced rapidly solidified powder technology in the composite. "This route appears to confer higher overall strengths, but lower tensile ductility of the product compared with liquid phase processing techniques[61]."[5,16]

The mechanical alloying route entails the pure metal powder and its alloying elements being mechanically alloyed in a high energy balling mill with the carbide filler to produce the discontinuously reinforced metal matrix composite. During this process, the occurrence of heavy working leads to repeated welding, fracturing and re-welding of the particles. The product is then consolidated to a suitable shape. This process is of particular benefit when manufacturing materials with large alloying additions for the prospect of improving the mechanical properties at elevated temperatures.[5,61]

1.7 Applications of MMC's.

The two major factors involved when considering the replacement of an old material are the possible improvement in performance and a reduction in price. These requirements however are not necessarily compatible. The compromise then would be a trade off between the possible increased performance and the increase in the price.

The use of these materials is intrinsically linked to their properties and thus a thorough understanding of the way these materials behave as well as their application is essential to apply them in the most profitable manner.

The importance of the introduction of composites to the sports and leisure industry should not be underestimated. The popularity of carbon fibre squash rackets and fishing

rods and boron fibre reinforced aluminium tubing in bicycle frames, as well as the introduction of particulate reinforced aluminium tennis rackets and golf club[1] available today is responsible for the creation of mass production of many of the materials now in use in more technically advanced areas. This creation of a mass production reduces the cost of manufacture for industries which previously would not have considered the use of composites due to the price.

1.7.1 The Automotive Industry.

The need for lighter, more fuel efficient engines has lead to the reconsideration of MMC's for many engine components. The unique properties that these materials offer over conventional materials make them ideal candidates for consideration as a replacement material in the automotive industry.

The cost of these components is of paramount importance when considering the use of MMC's, as well as weight reduction. Their application to the automotive industry stems from the successful application of short fibre preforms to selectively reinforce the crown and ring groove in diesel engine pistons[2,5]. The increased abrasion and wear resistance of MMC's also makes these materials suitable for use in compressor bodies, vanes and rotors, piston sleeves and inserts, connecting rods, cylinder heads and clutch components. The reduction in thermal expansion when using these materials also allows a closer fit in the cylinder bore resulting in an increase in fuel economy and wear resistance[5]. This property is also of benefit in clutch plates and brake disks.

However their cost is a major drawback, meaning that financial gain can only be made at present by replacing already expensive components, of which there are few.

1.7.2 Aircraft and Aerospace Applications.

In contrast to the automotive industry, the aerospace industry considers the primary concern is weight saving. The landing gear of an aircraft, or the skids of a helicopter are

dead weight when the craft is in flight, consequently, the importance of a reduction in size and weight is clear. The use of MMC in the non-load bearing areas of the space shuttle such as the cargo bay would be an obvious advantage.

Boron fibre reinforced aluminium pylon skins have been introduced for use on DC-10 aircraft [10], but the major use of MMC's in the aerospace industry is in military aircraft applications. "Without exception all agile fighter aircraft currently being designed throughout the world contain in the region of 40% of composites in the structural mass"[5], with the resultant weight loss allowing the degree of agility essential to todays fighter aircraft.

The need for higher performance materials in jet engines is becoming more imperative as the limitations of the present materials are being reached, yet the demand for better performance is as high as ever. It seems that the best way to achieve this would be to increase pressure ratios and reduce the number of compressor stages, along with a reduction of blade tip clearance and an increase in operating temperatures.

The possibility of space satellite applications also arises as high specific strength and stiffness is required, along with high dimensional stability. MMC's can also be of great value for structures such as microwave guides, optical mirrors and communications antennae where solar heating could cause distortion and loss in performance[2,5].

1.7.3 Electronics and Communications Applications.

Electronics and communications applications include the use of MMC's with exactly matched coefficients of thermal expansion in integrated circuits to reduce heat generation.

The reduction in weight with no loss in rigidity of antennae in radar systems is of great importance on naval ships since accuracy and their placement on the highest point to maximise the visible horizon, is important.

Graphite-aluminium composites have high stiffness and very low coefficients of thermal

expansion, making excellent candidates for space applications such as antennas and space telescope where the accuracy of their geometric stability is essential, and their high thermal conductivities resist distortion of components exposed alternately to the light and shade in space. The thermal properties of aluminium SiC particulate reinforced composites have also been taken advantage of in the packaging of microwave circuits. The SiC reduces the thermal expansion to better match that of the ceramic circuit substrate, without significantly reducing the thermal conductivity of the material which is required for heat dissipation from the appliance[5].

1.7.4 Applications For Smart Materials.

With the introduction of these new materials, there comes the added bonus of new and previously unexploited areas of possible use.

The addition of reinforcements to materials has meant that the introduction of sensors and actuators into these materials is possible, their superior strength has meant that a small reduction in their cross-section is not too detrimental to their efficiency. This could enable engineers to measure the amounts of accumulated strain in aircraft components for example. Consequently, the components can be replaced at the point where they are reaching the end of their useful or safe life, instead of the early, or in some cases late, replacements, usually at their service period of so many flights or air-miles. This in turn leads to a reduction in price of maintenance and an increase in the aircraft safety. There are many other ways in which these smart materials may be employed, making the lives of engineers easier and those of the users safer, although it must be stated that any possible detrimental effects on their properties must be considered[5].

1.8 Mechanical Properties and Fracture of MMC's.

Before a proper understanding of MMC monotonic tensile properties can be attained, it is necessary to understand the mechanical properties of ductile materials.

1.8.1 Tensile Testing of Ductile Materials.

Tensile testing of ductile materials always produces a curve of the form seen in figure 3, where stress is plotted against strain.

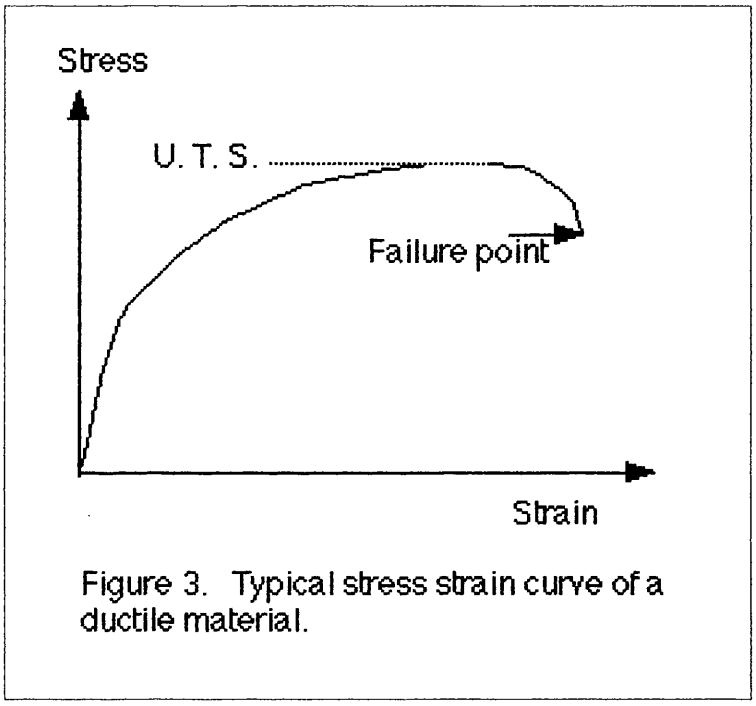

Figure 3. Typical stress strain curve of a ductile material.

The first stage of the curve is a straight line, the gradient of which gives the value of the elastic modulus. Elastic deformation is immediately reversible on the removal of the load. Where the curve begins to deviate from this line is the onset of plastic deformation, also called the yield strength. This is non-reversible deformation, as this is where enough energy has been put into the material to overcome some of the dislocation pile-ups, where the easy glide of dislocations along their planes has been interrupted by either a grain boundary, or a particle blocking the glide path. Due to the increasing numbers of dislocations within the material, there is also a phenomenon called work

hardening taking place. This stage of the stress strain curve continues until the onset of necking at the Ultimate Tensile Strength (UTS). Here, the increase in the rate of cross-slip has reduced the rate of work hardening. This stage is particularly pronounced in materials with a high stacking fault energy, such as aluminium[17]. Necking of the material manifests itself as the gradual decrease in the cross-section of the material over a small portion of the gauge length. The final stage of the curve is the failure point. This is the point at which the specimen gives way in a catastrophic manner.

On observation of a tensile test, ductile fracture surface, a cup and cone effect can often be seen. It may also exhibit a dimpled appearance. As the material becomes more brittle, the fracture surface takes on a more faceted appearance. It has been observed that particulate strengthened MMC's tend to exhibit features of both failure modes on their surfaces[18]. The dimpled appearance is caused by the mechanism by which the material fails. For ductile fracture, this occurs by a process of void initiation and coalescence. Several mechanisms of void formation and coalescence have been investigated, resulting in the conclusion that voids generally form where deformation is inhomogeneous.

1.8.2 Fracture of Ductile Materials Containing Second Phase Particles.

Where there are second phase particles present, this appears to be the preferred initiation site[19,20,21,22,23] although this is disputed by Davidson [24] and Arsenault et al [18] who concluded that the void nucleation occurs at subgrain boundaries or in the material adjacent to the particle/matrix interface. The phenomenon of dimpling is examined more closely by Tien et a[25], under the influence of hydrogen transport. He concluded that the role of the hydrogen in this case is most likely to weaken strong interfacial bonds between the particle and the interface. The evidence for void formation is supported by authors of several papers on composite materials[7,21,22,23,26,27,28,29,30,31] who claim that their formation occurs either by particle fracture or by the separation of the interface between

the particle and the matrix, although Flom and Arsenault[32] and Manoharan[33] found no evidence of void nucleation at SiC particle interfaces. It has been proposed that the initiation of cracks and voids is due to residual stresses from thermal mismatch, elastic stress concentrations where inclusions encourage local stress increase, and the stress distribution in the matrix where large stress gradients may exist between matrix material immediately adjacent to the reinforcement and the body of the matrix material[12,22]. It has also been observed[34] that these stresses are largest at the surface in quenched specimens. Of particular interest, they quoted that a T4 heat treatment would be expected to induce an approximately parabolic through thickness macroscopic stress variation in sheet metal.

Workers have noted that the fracture surfaces of composite materials appear to have larger dimples associated with the SiC particles, and many other small dimples between these in the matrix material[7,32] and interparticle spacing is proportional to dimple size[35].

The final failure of the material, however, is the coalescence or connection of these voids. When a material is stressed, microcracks form throughout the material, but are easily held up by grain boundaries or inclusions. The critical stage of cracking is the linking up of these microcracks to form a crack large enough to propagate. It has been suggested that these voids may be considered to behave as microcracks and as such, when enough of these voids have coalesced, they form a void large enough for unstable propagation to occur[19,36,37]. Gerberich[37] also suggests that the fracture of brittle second phases ahead of the crack tip add to the problem of sub-critical crack growth. This means that the addition of brittle second phases may theoretically have a detrimental effect on the properties of metals and their alloys. Edelson and Baldwin[38] suggest that hardening is a function of the mean free path between particle additions, and embrittlement (or ductility) a function of the volume fraction, which is in agreement with other work[32].

Another factor to consider in the fracture of composite material is the crack behaviour at the interface between the two different matereials of the matrix and reinforcement. Work

by Swenson and Rau[39] suggests that failure in the interface is most likely when the crack is proceeding from the matrix to the particle. Leverenz[40] suggests that the stress intensity factor at the crack tip is increased in this circumstance. He also concludes that a difference in Poisson's ratio between the two materials has a negligible effect on the stress intensity factors. This is disputed by Swenson and Rau, who conclude that a difference in Poisson's ratio causes significant changes in the relative intensities of the stress components. Based on their final conclusions, Hancock[41] suggests that for the case of a crack initiating in a particle and touching the interface, the situation is quite complex. A crack may grow away from the particle in opposite directions, or if growth does not occur at nearly equal rates at all sites surrounding the particle, the mode of crack growth would restore cylindrical symmetry to the crack.

Probability distributions for the strength of composite materials have been proposed for continuous fibre composites[42], but this type of analysis for particulate strengthened MMC's has yet to be fully tackled.

M. Gensamer[20] examined steels of various compositions and found that the strengthening effect of even coarse dispersions outweighs the effect of dissolved alloying elements. In fact the effect of dissolved elements is insignificant in comparison to the strengthening effect of fine dispersions. He also states that "strength is not sensitive to local variations in composition and structure; the alloy averages its strength over considerable volumes", it depends on composition in solid solutions and the mean spacing of particles in an aggregate structure and not on the shape of the particles.

J. M. Papazian and P. N. Adler[43] states that, "the addition of SiC whiskers or particles causes an increase in the monotonic response of 0.2% yield and UTS of precipitation hardened 2124 Al alloy, regardless of the matrix microstructure, as well as increasing the modulus and work-hardening rate. They also state that for a given volume fraction of SiC, whisker reinforcement always had a greater influence on the modulus than particulate and that the "primary strengthening mechanism in the 2124 composites is precipitation hardening due to the traditional age-hardening precipitation reactions. The major effect of

the SiC is to increase the elastic modulus and the work hardening rate". They suggest that the properties of the matrix alloy should be the focus of attempts to increase the composite's resistance to plastic flow. Other workers however[33], propose that for a high strength aluminium alloy, the UTS and yield stress is decreased with the addition of reinforcement.

Several workers have concluded that the strength of a monolithic alloy is increased with increasing proportion of reinforcement phase, up to a critical point[38,44,45,46], or a decrease in particle size and increased volume fraction[43,46,47]. The fracture toughness of MMC's has been shown to increase with increased volume fraction of SiC or particle spacing[32,33,48]. Rees[46] states that for a given volume fraction, the smaller the particle, the more strength is imparted. It has been reasoned that the increase in strength of the composite materials compared to their corresponding monolithic alloys is due to microstructural refinement[46], caused by the SiC particles pinning effect[7,49,50,51]. Another suggestion for the improved mechanical properties is the increase in dislocation density, due to thermal mismatch between the matrix and reinforcement phase.[8,28,29,46,52,53,54,55,56,57,58] Christman and Suresh[59] also observe that other strengthening mechanisms must be in operation as the formation of dislocations by cold working does not increase strength to the same extent. This is in agreement with other work[16,60]. With an increase in the dislocation density and the pinning effect of the reinforcement both in operation, the work hardening rate is higher in the reinforced alloys[30,43,54]. It has also been observed however that the addition of reinforcing particles reduces the ductility and toughness[8,15,33,38,46]. It should also be mentioned that these additions also significantly decrease the aging time of the material[16,53,62], although Shakesheff[63] disputes this. He also concludes that the toughness of Al-Cu-Mg MMC's is reduced by artificial aging. Workers have noted that the fracture toughness is greatest at the solution treated condition and that aging is detrimental to this property[64,51]. Manoharan et al[33] conclude that their underaged specimens exhibited a fracture initiation toughness twice that of the overaged specimens and as the SiC particle content

increased, so the initiation toughness decreased. Also, the underaged composite crack growth toughness was twice that of the overaged condition which was associated with a change in local fracture mode from particle fracture to failure near the SiC/matrix interface (respectively).

1.8.3 Strain Rate Dependence.

Studies carried out on the dependence of properties of MMC's on strain rate have been conducted at elevated and room temperatures. Tensile testing of Al_2O_3 particulate strengthened 2014Al composite at room temperature resulted in increased peak load, deflection, ductility and total fracture energy at high strain rates. This result was reflected in the unreinforced material, although to a lesser extent[65]. This is in agreement with work by Pickard et al[21] who also conclude that the failure strain increases with strain rate in 2124Al SiC whisker reinforced composite. They also state that the failure mode changes as the strain rate is increased. The lower strain rates resulting in void formation and coalescence, and the higher strain rates exhibiting particle cracking followed by ductile coalescence.

The work conducted at elevated temperatures at a high strain rate appears to confer a degree of superplasticity on the material. Nieh et al[66] observed that at elevated temperature, 'as the strain rates increased, the tensile ductilities increased'. Further more, at increasing strain rates, elongation to failure values increase correspondingly. In a later work[67] the mechanism for failure was concluded to be due to the presence of a liquid phase (possibly from the presence of a low melting point region due to solute segregation) is responsible for the high strain rate superplastic behaviour. This is in agreement with subsequent work[68]. The phenomenon is also noted to be characteristic of typically fine structured materials, such as aluminium MMC's. A maximum room temperature strength can be achieved by compression of the metal matrix composite at a temperature just below the solidus line of the matrix alloy[68].

CHAPTER 2.

2. Fatigue of Materials.

The word *fatigue* is a well accepted term for describing the deformation and failure of materials under cyclic loading conditions. It is the "progressive localised permanent structural change which occurs in a material subjected to a fluctuating strain, at a stress below the tensile strength of the material."(70)

Cyclic deformation in ductile solids can cause cyclic strain hardening, or softening(69). That is to say, a rapid increase/decrease (respectively) in the flow stress with increasing number of cycles. As the number of cycles increases, this hardening/softening effect decreases until saturation, where there is no change in peak stress or strain with each cycle. One of the most visible features of cyclic saturation in a pure metal single crystal is the appearance of persistent slip bands (PSB's). These are slip steps which have become apparent on the surface of the material due to the localisation of slip along certain slip bands or planes and reappear after surface polishing. These slip bands have been shown to be softer than the matrix material and to appear at the same time as the onset of the plateau region of the cyclic stress-strain curve, indicating that the entire deformation takes place in the PSB's during saturation in this region(70). On the addition of aluminium alloying element to pure copper sample, the stacking fault energy was reduced, which reduced the initial hardening rate(70). Cyclic stability has been observed in 2124 aluminium matrix SiC partical strengthened MMC material(3,6)and several workers have noted that the addition of SiC particulate reinforcement to an aluminium matrix reduces the notch sensitivity under fatigue loading with R = 0.1(72, 73).

Composites are inhomogeneous by definition, containing numerous internal boundaries which separate constituent materials that have different responses and resistances to the long term applications of external influences.

The three major types of damage caused to these materials on the application of such external forces are(74):

- Constituent damage; micro-cracking of particles,
  chemical degradation,
  plastic deformation,
  crazing of the ceramic.
- Boundary separation; debonding or delamination,
  interphase cracking,
- Inhomogeneous deformation; yielding of boundary material,
  discontinuous deformation gradients.

2.1 Mechanisms of Fatigue Initiation.

The development of a fatigue crack consists of three major stages, these being initiation, propagation or growth, and failure. Initiation occurs at maximum local stress and minimum local strength and is usually defined as, 'the formation process of microcracks having less than detectable length, say 10^{-3} mm to 2.5×10^{-2} mm'[16,75]. Research into the initiation process has concluded that the presence of a constrained volume is a necessity, generally, these occur at or near the surface of a specimen[41,76,77,78], especially at inclusions and discontinuities and pre-existing flaws. Initiation may also occur in regions of high stress concentrations. These can be caused by thermal, mechanical or chemical treatments. In compression, these residual stresses have a favourable effect, but in tension, a detrimental effect. This means that fatigue crack initiation is highly dependent on the surface condition of a specimen[41] where the triaxial stresses imposed on the interior of the specimen no longer hold. As Laird and Duquette conclude[79] 'fatigue crack initiation either in the presence or absence of aggressive environments does not occur by the same mechanism for every material', hence the current problem in producing an effective model for all fatigue failures.

The first stage of initiation has been shown, for the case of a pure metal single crystal, to develop from the formation of slip bands[70]. As slip continues during the fatigue cycle, intrusions and extrusions emerge on the surface of the specimen. These are known as

"Persistent Slip Bands" or PSB's, because they do not polish away. The generation of a microscopic crack, or series of microscopic cracks propagating perpendicular to the stress direction[76,77], is the final stage of the initiation phase.

Lusak and Koss[80] found that initiation of a fatigue crack in particle reinforced aluminium MMC's occurred under high stress amplitudes either from the fracture of a reinforcing particle, or in a matrix ligament separating a subsurface particle from the free surface. As particle size increases, the particle cracking mechanism becomes predominant. This has been supported by other work[47,81,82,83,84].

Chang Gil Lee et al[84] state that void initiation in 2124 aluminium alloy matrix composites occurs by cracking of coarse manganese containing particles, and that in particulate reinforced material, voids initiate at the side of the reinforcement and propagate along the interface, although in their study, the most apparent void initiation mechanism in particulate strengthened material was particle cracking. The deformation of the MMC as cyclic loading continues may either become localised, or dispersed throughout the matrix. Llorca et al[35], concluded that plastic strains and void formation at inclusions occurred throughout the matrix in the particulate strengthened composites, conversely, the whisker strengthened composites tested showed localisation of these phenomena in the vicinity of the reinforcement. It should be noted that in commercial systems, the distribution of particles is not entirely uniform and the location of crack initiation may well be altered by particle clusters. Several workers have suggested that these clusters form a likely initiation point for fatigue cracking[47,82,83].

In the examination of the locations of crack nucleation, it is also important to consider the possibility of environment-related mechanisms in operation. These will be discussed further in the next chapter.

2.2 Crack Propagation.

The initiation phase is followed by propagation of the crack through coalescence of the microscopic cracks and voids and subsequent growth[69]. The crack gradually lengthens with each wave cycle along the planes of maximum shear, often producing a characteristic step-like advance, where propagation is opposed by the surrounding microstructure.

The principle driving force for fatigue crack propagation under small scale yielding is the stress intensity factor, ΔK, which is given by;

$$\Delta K = Y\Delta\sigma(\Pi a)^{1/2}$$

where, Y is a factor dependent on the component and crack geometry,

$\Delta\sigma$ is the stress range (maximum stress minus the minimum stress) and

a is the crack size.

At low stress intensity and threshold conditions, ΔK_{th} is apparent. This is the value of the stress intensity factor range below which, fatigue crack growth is not supposed to occur. However, it is only relevant for short or long crack growth behaviour.

Many attempts have been made to produce a universal model to predict the growth rate, but due to the number and diversity of the influencing variables, no one model can be relied upon for all conditions. Microstructural variation and poor particle size uniformity in commercial systems create problems for prediction of time and form of failure. For much of its life, a long crack is found to behave according to the Paris law;

$$da/dN = C\Delta K^m;$$

where, da/dN is change in fatigue crack length per load cycle,

ΔK is the stress intensity factor range, such that $\Delta K = K_{max} - K_{min}$

C and m are constants denoting functions of material properties and microstructure, fatigue frequency, mean stress or load ratio, environment, loading mode, stress state and test temperature.

It is important to note that stable fatigue crack growth occurs at stress intensity factor levels where;

$$K_{max} = \Delta K/(1-R)$$

which are well below the quasi-static fracture toughness.

In the Paris region, experiments on crack growth have confirmed a power law relationship of this form, especially in aluminium alloys with different combinations of stress range crack length and differing specimen geometries. Often, striation formation is apparent in this region in the matrix materials, but not so much in the composite material. The microstructure has very little effect in this region of fatigue crack growth rate. Llorca et al[4] state that composite properties are degraded at high ΔK and that under these conditions, more broken particles were observed in the fracture surface. This has been confirmed by other workers[81,85].

Figure 4 shows a typical plot of da/dN against ΔK for engineering alloys, which generally exhibit a sigmoidal form.

In region I, the initiation/small crack propagation, the average growth per cycle is less than one lattice spacing and fatigue crack growth is generally influenced by the microstructure, the mean stress and the environment.

Region II, propagation stage, is also termed the Paris region, and behaviour is generally dictated by the Paris law. This is the intermediate region of crack growth and is generally affected by the environment, mean stress, microstructure, and cycle frequency.

Region III, propagation to failure, is the high ΔK range where crack growth rates increase rapidly causing catastrophic failure. This region is influenced by microstructure, mean stress and thickness of the specimen.

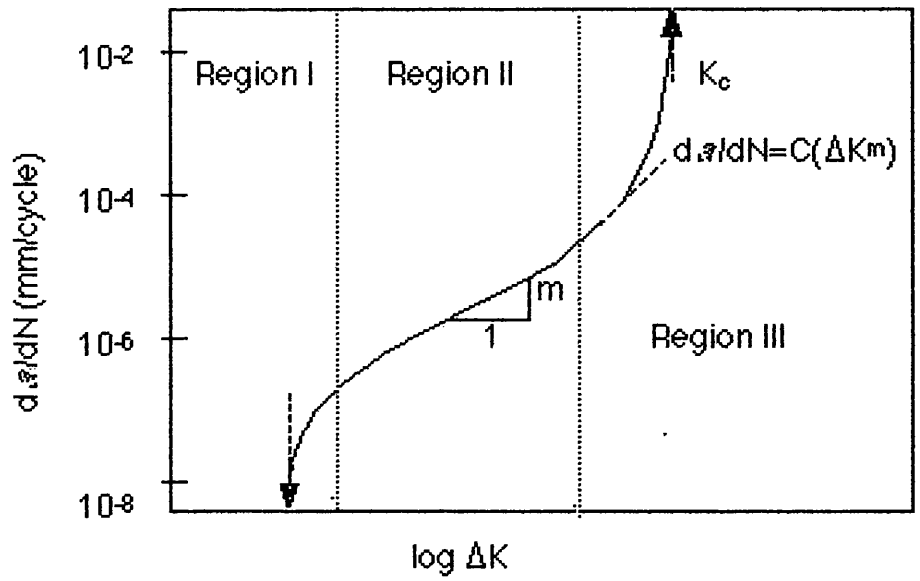

Figure 4. Typical plot of crack growth rate against stress intensity factor for an engineering alloy.

Manabu and Eto[48] conclude that at high stress intensity factor range (ΔK) fatigue crack propagation rate in 2024 Al alloy is determined by constituent (e.g. Cu_2FeAl_7) spacing. At low ΔK, it is controlled by dispersiod (e.g. $Cu_2Mn_3Al_{20}$) spacing.

The propagation of a fatigue crack occurs along the path of least resistance. In a particle reinforced metal matrix composite, if there are few small particles, and the specimen is under low stress, then the crack will tend to propagate through the matrix material with debonding of the particles from the matrix. Cracking of particles under these conditions is uncommon. As the stress and the particle volume fraction are increased, particle cracking becomes more prevalent[4,47,83]. Particle cracking is also more likely as the number of cycles increases[4]. Work by Corn[86] has shown that the propagation of a crack, tends to a preferred crack path, using axial fatigue, the crack path follows a/c .0.9, where a is crack depth and c is half crack length. This work has been supported by other workers for commercial aluminium alloys[76,77]. Toda et al[87] also concludes that the presence of microcracks in the region of the crack tip as it propagates may deflect the crack path and hence retard growth.

The appearance of the fracture surface is highly dependent on the ductility of the material. As in monotonic tension testing, the more ductile materials exhibit a dimpled fracture surface and with increasing brittleness, a more faceted appearance.

2.3 Effect of Stress on Fatigue of MMC's.

Methods for characterising the fatigue life in terms of maximum stress, stress amplitude or mean stress have been determined (detailed in Standards E466-E468 of the American Society for Testing and Materials (Philadelphia)) for fully reversed fatigue cycles. The maximum or mean stress is plotted against the number of cycles to failure (N_f), resulting in what is commonly referred to as an S-N curve. Under constant amplitude loading conditions, some materials exhibit a plateau at the high cycle end of the plot, below which samples may be cycled indefinitely without causing failure. This stress amplitude is known as the fatigue or endurance limit. Many high strength steels, aluminium alloys and other materials which do not strain-age-harden, do not generally exhibit a fatigue limit[70]. In these cases, the endurance limit is defined as the stress amplitude which the specimen can support for at least 10^7 cycles. However, Bathias[88] concluded, from work on some aluminium based MMC's that this fatigue limit was inaccurate as he found that many of his specimens broke above this value. If this curve is redrawn on a log-log scale, with true stress against the number of cycles, a linear relationship is commonly observed[3].

It must be clarified that these procedures relate to the total life of the specimen, which means to say the initiation and propagation of the fatigue crack in a carefully prepared 'defect-free' material. The fraction of the fatigue life which is expended on initiation of a crack may vary from 0%, for specimens containing severe stress concentrations, to 80% for defect free smooth specimens of high purity.

Plumtree et al[76] found that crack initiation can occur below 10^7 cycles at stresses well

below the endurance limit of a material. However, the growth of these microcracks can easily be impeded by grain boundaries. They also stated that due to less constraint, they found that larger surface grains facilitated PSB formation and ensuing intrusion formation.

2.4 The Effect of Load Ratio on Fatigue of MMC's.

The load ratio of the test is described by $R = \sigma_{min} / \sigma_{max}$. Therefore, R = 0, describes zero tension fatigue, R = -1, fully reversed loading and R = 1, denotes static load. This can have a significant effect on fatigue crack growth.

Mean stress in fatigue can also be represented in terms of constant life diagrams. The most well known of which are;

Gerber, $\sigma_a = \sigma_{fs} \{1-(\sigma_0/\sigma_{UTS})^2\}$ where σ_a= stress amplitude ($R \neq 0$), σ_{fs} = fatigue strength (for a fixed life for R = -1 and σ_0 (mean stress of the fatigue cycle) = 0), σ_{UTS}= ultimate tensile strength.

generally a close approximation for most engineering alloys;

Goodman, $\sigma_a = \sigma_{fs} \{1-(\sigma_0/\sigma_{UTS})\}$

which matches experimental data for brittle metals, but provides a conservative estimate for ductile alloys and;

Soderberg, $\sigma_a = \sigma_{fs}\{1-(\sigma_0/\sigma_y)\}$ where σ_y = yield strength.

which provides a conservative estimate for fatigue of most engineering alloys.

It should be emphasised that these stress based characterisations are only relevant for constant amplitude fatigue loading, which is a highly unlikely condition for in-service components.

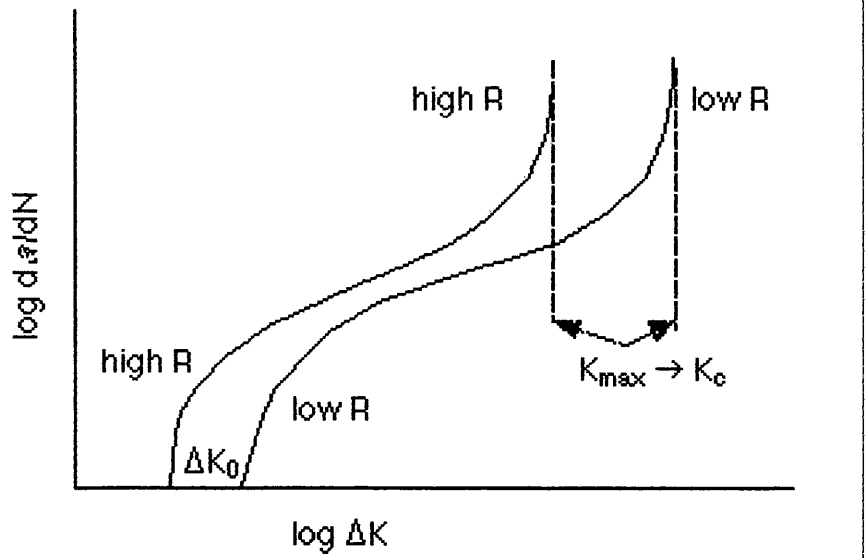

Figure 5. Chart showing the effect of load ratio, R, on fatigue crack growth behaviour.

Figure 5 * . shows the variation of crack propagation rates as a function of ΔK and load ratio, R. In both regime I and III, load ratio can exert considerable effect on the crack growth behaviour. Regime III is largely influenced by load ratio due to K_{max} approaching the fracture toughness or critical stress intensity, K_c, of the material.

$$K_{max} = \Delta K/(1-R) \rightarrow K_c.$$

Since the stress intensity range values where K_{max} approaches K_c, are lower for high R ratios, final failure occurs at lower stress intensity range values at higher load ratios. Bache et al[71] however found no R value dependence in the particle reinforced material. There are several other factors which may alter the fatigue characteristics of a material, including environment, processing route, heat treatment, previous load history, specific local composition and surface condition of the component or sample[89]. Changes in any one, or a combination of these can cause a change in the fatigue response.

Work conducted by Wang and Zhang[5] concluded that extruded MMC's did not show any improvement over the unreinforced material, as the cast MMC's did. Hochrieter et al[7]

* Reproduced from 29, p. 220.

concluded that addition of particle reinforcement reduced fatigue life in most cases, although all their testing was carried out on extruded MMC's. This is also contradicted by the work of Bonnen et al[90]. They did conclude however that the homogeneity of the particle distribution, which is chiefly controlled by the production route, determined the efficiency of the reinforcement, which is in agreement with Bathias[88].

If the surface of the specimen is rough, then the fatigue life is lowered as this introduces local areas of higher stress intensity, facilitating the initiation step. Johnson and Oberg[91] also concluded that an aluminium alloy could be substantially weakened by the application of even a low stress over the course of just 100 million cycles. If the stress is subsequently raised a failure below the normal fatigue curve for that material ensues. However, workers have found that the endurance of aluminium is not affected by the frequency at which the test is operated in a given strain range[92]. Some of these factors will be discussed further, later.

The high growth rate region is far more sensitive to microstructure, load ratio (R), and stress state, but propagation rate is too fast to be generally affected by environmental conditions. At high stress intensity, more static fracture modes begin to operate. These include, cleavage, intergranular separation and striation growth. These cause a marked sensitivity of propagation rate to microstructure.

2.5 Crack Retardation.

Retardation of fatigue cracks can occur through crack closure, crack bridging or trapping, and crack shielding due to phase transformations, dislocations and micro-cracking. Crack closure can occur through one of, or a combination of several different mechanisms including plasticity induced crack closure, oxide induced crack closure and roughness induced crack closure.

2.5.1 Crack Closure.

Some of the general points of crack closure as stated by Suresh[70], are summarised below.

'1) Crack closure is generally more dominant at low stress intensity and R ratio due to the smaller minimum crack opening displacements of the fatigue cycle.

2) A characteristic size scale is associated with each closure process. For oxide induced crack closure, it is related to the oxide layer thickness of the fracture surface and for particle induced crack closure, it is related to the size of the particles. When the size of this characteristic closure dimension becomes comparable to the crack opening displacement, premature crack face contact occurs which has a marked effect on the rate of fatigue crack growth.

3) When establishing crack closure levels the standard optimum rate of load reduction is generally selected carefully, but arbitrarily. If it is too slow, an artificially high threshold value may be found, due to oxide formation. If it is too fast, premature crack arrest may occur due to overload effects.

4) Different methods for detecting crack closure may result in different estimates of closure due to the number of variables involved, including specimen size and geometry, crack size stress state and location with respect to the crack tip and also environmental and microstructural effects.

5) The breakdown of similitude due to crack closure means different levels of crack closure may be observed in the same material for differing crack sizes with the application of identical stress intensity values.

6) Bulk measures of crack closure can not distinguish between the different closure mechanisms and therefore can give no indication of how many or which mechanisms may be operating at any one time.'

Some of the crack closure mechanisms which may be in operation in MMC fatigue crack growth include; plasticity induced crack closure, oxide induced crack closure and

roughness induced crack closure.

Llorca et al[4] specifically ascribes the difference in crack propagation rate of composite and base matrix alloy to the effects of crack closure in the composite material.

2.5.2 Fatigue Crack Deflection.

Crack deflection in the near threshold region (mode I) can retard crack growth rates by several orders of magnitude. Periodic deflections in the crack path have three major effects.

1) An apparently larger driving force is required for the propagation of a deflected crack at the same rate that the corresponding straight crack would propagate.

2) Measuring along the mode I growth direction, for the same effective driving force, a deflected crack has an apparently slower rate of growth than a straight crack.

3) The small mismatches that can be created by deflection, can lead to crack closure mechanisms coming into operation, amplifying the apparent driving force for the deflected crack propagation.

Microstructure modification induced crack deflections and reduce the apparent driving force for fracture. Some microstructure design methods may actually increase crack growth rates by reducing the intrinsic resistance of the material to fatigue crack initiation and growth. This method of crack retardation in MMC fatigue is widely recorded in the literature[7,70,81].

2.5.3 Crack Bridging.

Crack bridging occurs in unidirectionally strengthened fibre reinforced MMC's, if the fibre strength is sufficiently high. The tensile crack extends through the matrix and the crack face is bridged by unbroken fibres. This promotes apparent resistance to fatigue crack

growth.

The influence of particles on fatigue fracture may occur by either deflecting the crack tip and causing a reduction in the effective stress intensity factor, (K_{eff}), or trapping or bridging of the crack front. The accompanying geometric changes of the crack front can lead to apparent improvement in fatigue crack growth resistance.

2.5.4 Crack trapping.

Similarly to crack bridging, the interaction of the crack front with hard second phase particles may effect the geometry of the crack front and the crack growth rate. This may come about in one of two ways. Firstly, impenetrable particles deflect the crack, reducing the effective stress intensity. Secondly, particles may 'trap' (bridge) the crack front, again altering the geometry of the crack front and leading to apparent improvements in fatigue strength, depending on particle distribution, size and toughness.

2.5.5 Crack tip shielding.

This process may occur by one of several methods including dislocation pile-ups, microcracking and phase transformations. The effect is to reduce the driving force of crack growth by 'shielding' the crack tip from far-field stresses. These methods are summarised diagrammatically in figures a) to i) below.

Aluminium MMC's retard crack growth in one or a combination of these ways.

Aluminium alloys reinforced with particles or whiskers of silicon carbide generally exhibit better near threshold fatigue crack growth characteristic than the unreinforced metal matrix alloy if fatigue failure occurs predominantly within the ductile matrix[93,94]. Deflection by the brittle particles and enhanced crack closure and crack trapping contribute to this improved fatigue resistance in the composite. However, if the particular combination of processing conditions, particle size, particle concentration and aging

treatment promotes particle fracture or interfacial separation, the fatigue crack growth

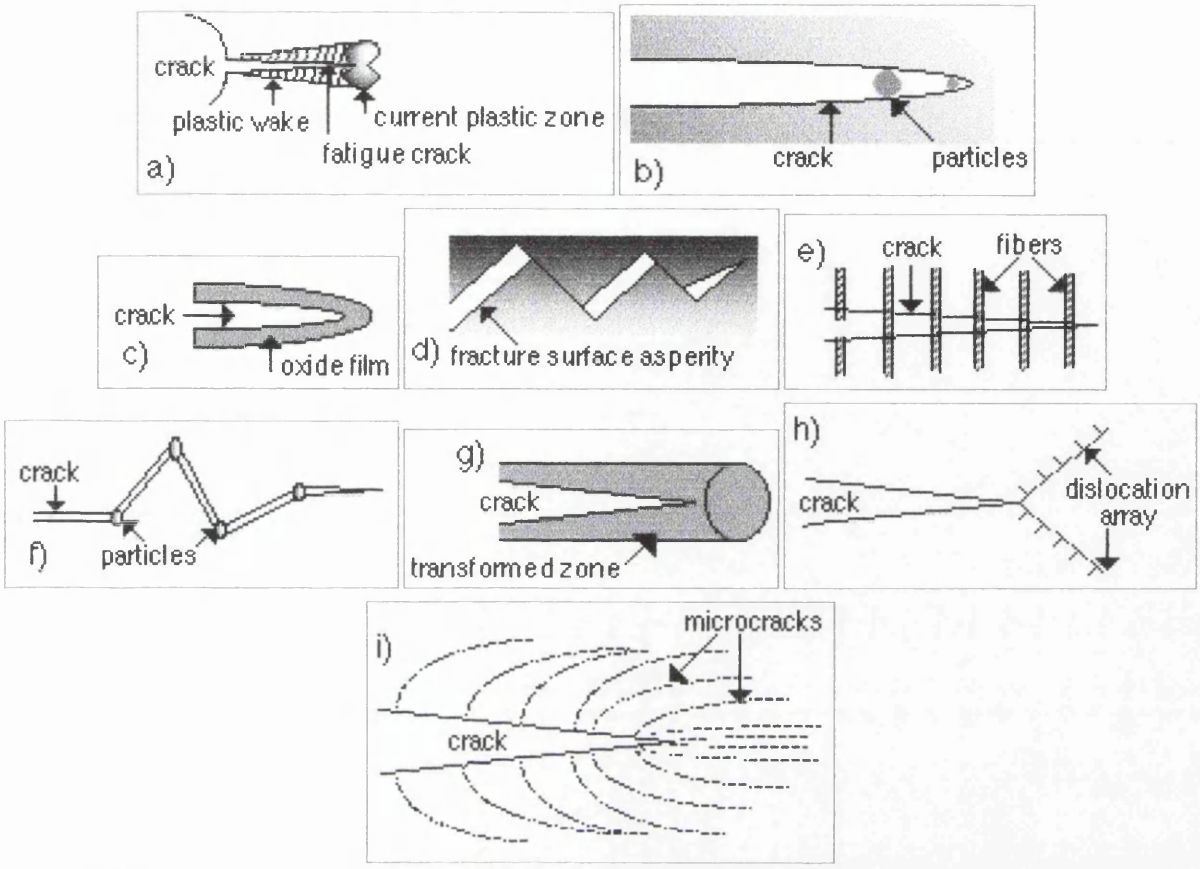

a) plasticity induced crack closure, b) crack bridging/trapping by particles, c) oxide induced crack closure, d) roughness induced crack closure, e) crack bridging by fibers, f) crack deflection, g) transformation induced crack closure, h) crack shielding by dislocations, i) crack shielding by micro-cracks.

resistance of the composite can be significantly lower than that of the matrix alloy[70]. Similarly, the low cycle fatigue properties of the composite can also be inferior to the matrix. Hochrieter et al[95] mention that reduction of fatigue crack propagation rate should be encouraged by employment of crack closure mechanisms. This is observed in Al-Si alloy with 20vol% SiC particle addition at 23^{0}C[85], whereby the interaction of the crack tip and the reinforcing particle resulted in crack tip deflection around the particle, resulting in roughness induced crack closure and hence a reduction in fatigue crack growth rate.

CHAPTER 3.

3. Corrosion and its Implications.

Corrosion is "the degradation of metals by an electrochemical reaction with the environment."[96]

There are many causes and types of corrosive attack, depending upon a variety of factors. The metals themselves are imperfect in their structures, including vacancies, substitutional defects, interstitial defects, various types of dislocations, voids, cracks and inclusions. These later three, termed 'volume defects', play a particularly important role in corrosion mechanisms.

3.1 Aqueous Corrosion.

The general theory of aqueous corrosion applies to all corrosion processes, but the effect, under varying conditions, differentiates the different types of corrosion.

The basic "corrosion cell" consists of an anode, cathode, an electrolyte and an electrical connection between them. The anode generally corrodes by loss of electrons from its neutral metallic atoms to form positive ions, which may either remain in solution or react to form insoluble corrosion products. The cathode consumes electrons produced at the anode, often by the process;

$$2H^+ + 2e^- \rightarrow H_2$$

although other types of cathodic reaction are also possible.

The electrolyte is the conductive solution which carries the electrons between the anode and cathode. Typically it contains dissolved salts such as sodium chloride (NaCl).

The circuit is completed by an electrical connection between the anode and cathode. If they are both part of the same material, this serves as a physical connection.

On the introduction of a metal in to an aqueous solution one of three things may occur.

1) The metal will corrode, resulting in metal dissolution.

2) The metal will acquire immunity, whereby the potential is lowered, preventing dissolution or,

3) passivation of the metal surface occurs, whereby the potential of the metal is raised as it is covered with a protective film, removing it from direct contact with the solution.

This is illustrated schematically below, in figure 6.

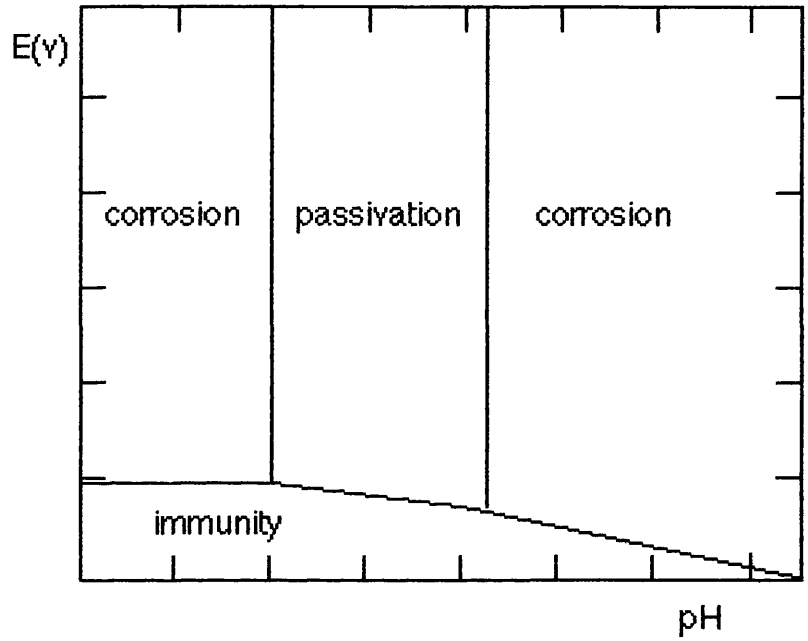

Figure 6. A general Pourbaix diagram to show typical behaviour of Aluminium.

Aluminium forms a protective film which renews itself immediately following damage and is thus highly corrosion resistant. The oxide has one and a half times the molecular volume of aluminium and thus is in compression so there may be some substrate deformation, but no rupturing.

It should also be mentioned that some aluminium alloys are more susceptible to corrosion and to specific types of corrosion. Of particular importance in this report is the fact that the copper containing 2XXX series alloys are particularly susceptible to corrosive attack when immersed in water. Research suggests that these alloys are at their most

noble at copper contents between 2 and 3%[97].

Aluminium initially oxidises to aluminium hydroxide which subsequently ages to hydrated oxide, or a mixture of oxides. Environmental factors such as temperature and solution turbulence can seriously affect corrosion resistance. Surface to volume ratio, the heat capacity of the surface, the surface finish, alloying additions and the presence of surface defects are all dictated by the aluminium alloy itself. Composition, volume, location and potential of microconstituents compared with aluminium solid solutions have a direct influence on the amount, form and distribution of corrosive attack. For example, $CuAl_2$ is cathodic to the matrix and produces corrosion damage around the precipitate particles, and Mg_2Al_3 is anodic to the matrix and is therefore a subject of corrosive attack. Murty et al[97] noted that the increase in copper content of an aluminium alloy caused local thinning of the oxide layer in the vicinity of the θ-phase (Al_2Cu) and concluded that this caused 'severe localised corrosion entirely attributable to solidification-caused inhomogeneity in the distribution of copper'.

Also of interest is the susceptibility of certain heat treated 2XXX series alloys to stress corrosion cracking (discussed further later in this chapter).

Corrosion may be classified into several categories, including; general or unlocalised attack, pitting, intergranular attack, stress corrosion and corrosion fatigue.

General corrosion causes the least weakening. It can occur by a process of a local anode being corroded, becoming cathodic to the surrounding material and repassivating, while a local passive cathode may be undermined by an adjacent anodic area, and become active.

Pitting usually initiates at a weak site on the surface of the metal, such as a flaw in a protective film or a surface scratch. Once initiated, attack continues to occur in that region in preference to others, causing a pit.

Intergranular corrosion occurs when the grain boundaries of a material are more easily attacked then the interiors. This causes intergranular trenches to appear. Stress

corrosion occurs in a metal under combined conditions of an aggressive environment and an imposed load. The appearance can be similar to that of intergranular corrosion, but the attack is localised to grain boundaries running roughly perpendicular to the stress direction. Some alloys exhibit a transgranular failure mode however.

Corrosion fatigue is a result of the combined effect of applied dynamic stress and an aggressive environment. It appears that this particular combination will produce failure in all metals at some point. This is due to the fact that under an alternating or dynamic stress a metal will manufacture weaknesses within its structure which are susceptible either to the stress component or the aggressive environmental component. Stress corrosion and corrosion fatigue cause the most weakening.

It should be noted that it is often not possible to predict the type of failure which will occur in a corrosive environment. Prediction may be best addressed by assessing the probability of a certain type of failure as proposed by Roberge[98].

When analysing the corrosion properties of aluminium based MMC's there are several additional factors to consider, including; whether or not the particles may interrupt the growth of the oxide film[97] and thus hinder repassivation; galvanic coupling between the reinforcement and the matrix; selective corrosion at the interface and corrosion of matrix defects from the manufacture of the composite.

Interfacial phase formation during processing (between the matrix and reinforcement) if strongly anodic or cathodic to the matrix may suffer potential corrosion voids, or crevices may form from volume changes. If the reinforcement is an electrical insulator (alumina, boron and silicon carbide) little or no galvanic reaction with the aluminium matrix is expected, unlike that with graphite which is highly electrically conductive.

Corrosion of Al-based MMC's may be induced by defects, impurities or segregation in the oxide film, due to whisker or particle addition. It has been suggested that the introduction of second phase particles (SiC) into an aluminium matrix make a 'very significant contribution to the resistance, even at low volume fractions'[99], which is thought to be due

to the high dislocation density, induced by the additions. Strain fields are generated during processing where coefficients of thermal expansion differ, thus higher dislocation densities exist at the interface encouraging second phase precipitation during aging. Fine precipitates can be observed along dislocations which reduce in density with increasing dispersion[100]. These also pose the possibility of preferential corrosion sites.

In electrochemical tests, the corrosion potentials (the minimum electrical current at which the corrosion process may begin) of the 2024-Al 20wt%SiC MMC and the matrix alloy are similar[101,102] and in some cases, additions may actually increase the corrosion resistance[103,104] suggesting that corrosion potential is unaffected by silicon carbide presence. This is also supported by the work of Pinto and Zschech[105]. Harris et al[106] however, conclude that the presence of CuAl. and CuMgAl. precipitates in 2124-based discontinuously reinforced composites promote pitting attack at SiC-matrix and intermetallic-matrix interfaces.

3.2 Bimetallic Corrosion.

This type of corrosion is also called dissimilar metal corrosion or galvanic corrosion, although the latter name is somewhat misleading as all aqueous corrosion is caused by the galvanic effect.

In salt spray conditions, accelerated corrosion behaviour has been observed in Al-2024 base alloy, but much less than in the 20vol% SiC Al-2024 composites[101]. The degree of corrosion increased proportionally to the SiC concentration in the matrix, attributed to galvanic action between the SiC and the matrix material[106]. This has been disputed by other workers[100,107] and instead the proposal that as SiC concentration increases, active precipitate concentrations arise due to the high strain fields associated with SiC, has been put forward[101].

Other work[107] has suggested that the susceptibility of this copper containing alloy is

directly related to the amount of copper it contains.

The effects of aeration and chloride ion concentration have been studied. In deaerated conditions and chloride free environments, galvanic current was negligible. The corrosion rate of a MMC is increased in aerated conditions[101,108,109]. In aerated NaCl, the corrosion current was only about 2.5 times that of aluminium coupled samples. Other factors probably exert a greater influence on corrosion behaviour than the SiC/Al couple.

3.3 Intergranular Corrosion.

The 2XXX series aluminium alloys of interest to this project are also particularly susceptible to this type of corrosive attack. It has been proposed that this form of corrosion is due to selective corrosion of a crystallographic nature[110] such that the grain boundaries themselves play an important role[111]. As has been pointed out, intergranular corrosion does not decrease with the increasing purity of a sample[58], indicating that selective attack due to impurities is unlikely. However, others have suggested that the grain boundaries may be selectively attacked due to the precipitation of impurities from the metal grains during solidification[112]. If these impurities are anodic to the dominant metal, the result could be selective corrosion at the grain boundaries or precipitate free zones (PFZ's) adjacent to them with the bulk matrix remaining relatively unaffected. In 2XXX series alloys, CuAl precipitation may occur at grain boundaries, causing attack to be concentrated at PFZ's. Galvele et al[113] concluded that the mechanism of intergranular corrosion is most likely to be due to a difference in breakdown potentials of grain boundaries and grain interiors, as opposed to the difference in standard electrode potential of these areas.

Several studies have been carried out on the role of hydrogen in this form of corrosion[25,89,114]. These studies show that the hydrogen produced during the corrosion process may serve to further weaken the material ahead of the crack tip due to its transport into the material through dislocation sweep and diffusion along the grain

boundaries(115). Hence the intergranular mode of failure.

Generally, aluminium alloys are less susceptible to intergranular corrosion when in the overaged condition.

3.4 Pitting Corrosion.

Pitting represents the most common form of aluminium corrosion, particularly in solutions containing chloride ions. It occurs in conditions where the surface film is almost, but not completely protective, such as at a scratch or other mechanically induced break in the protective film, at an emerging slip step (as discussed in chapter 2), or at a compositional heterogeneity, such as an inclusion, precipitate or segregate(116).

Local action in the presence of an electrolyte, usually in near neutral conditions, results in a small discontinuity in the protective oxide film. It is thought that flaws in the film are developed and repassivated constantly, but the presence of aggressive ions hinders repassivation(117).

It has been suggested that the induction time for pitting is proportional to the film/oxide layer thickness(118), but there is no agreement with regard to the effect of potential on pitting, except that there is a critical pitting potential (E_{pit}). It has been suggested that pits on aluminium will only initiate at an electrode potential above that of E_{pit} for aluminium(119,120). Once initiated however propagation can occur below E_{pit}, but above E_{prot} (where repassivation occurs), shown in the graph in figure 7 *

A pit initiation site may occur where a local anode, such as Mg_2Al_3, is surrounded by a matrix cathode leading to metal dissolution. Where an insoluble metal hydroxide is present, the local solution at the anode increases in acidity and the solution in the corresponding cathodic site becomes more alkaline.

---

* Taken from reference **10**

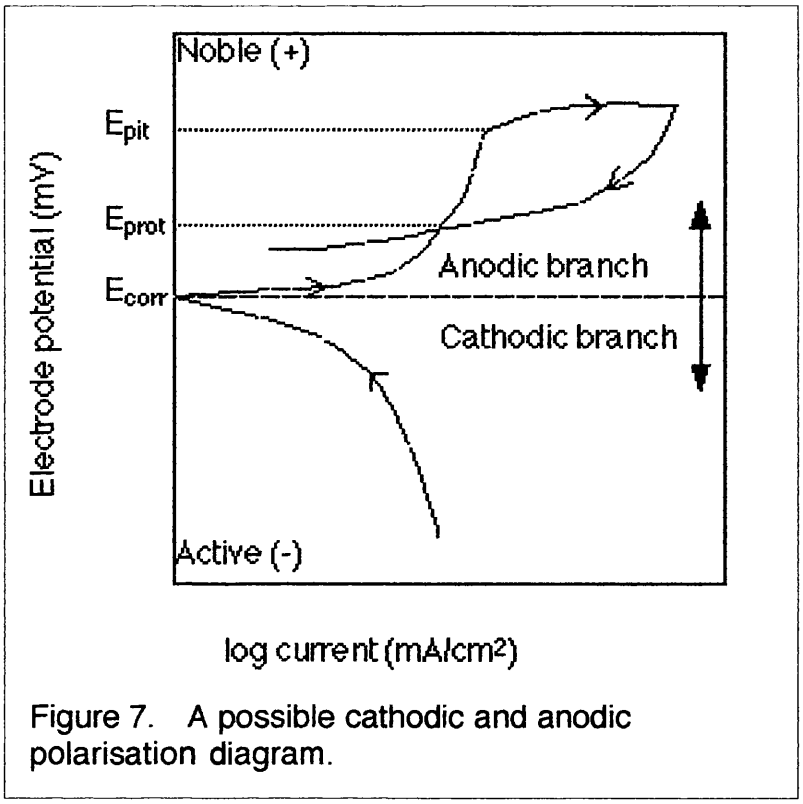

Figure 7. A possible cathodic and anodic polarisation diagram.

Since the cathodic solution is at the surface the degree of alkalinity is very much less than the acidity in the pit and as the pit grows, the cathodic region moves to the mouth of the pit.

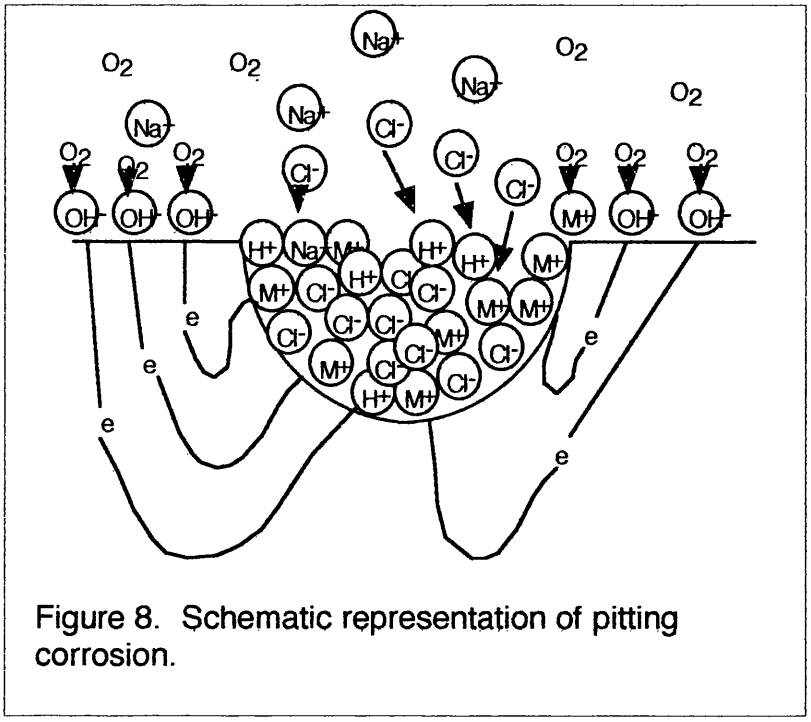

Figure 8. Schematic representation of pitting corrosion.

Insoluble corrosion products build up acting as a diffusion barrier between the oxygen and the anode, while the cathode still has a ready oxygen supply. Termination occurs when the electrochemical processes are stifled by the build-up of corrosion product. This is schematically represented in figure 8.

The reactions taking place in the pit can produce gaseous products such as hydrogen (as described in the previous section on aqueous corrosion), particularly in neutral conditions. This is supported by the observations of several workers that bubbles could be seen to form on the surface of aluminium test specimens [100,101,121].

'The corrosion resistant passive metal surrounding the anode and the activating property of the corrosion products (such as hydrogen) within the pit account for the tendency of the corrosion to penetrate the metal rather than spread along the surface.' [122]

Thompson et al [123] have designed an anodising technique which highlights flaws developing into pits. Further studies are in progress to determine how the flaws, which are influenced by substrate topography, develop by stages into pits that grow in favoured crystallographic directions [3,111,124].

2XXX series alloys are especially susceptible to pitting corrosion[10]. The electrochemical effects encountered in copper-containing aluminium alloys can be greater than in others. This may be partly due to the formation of cathodic $CuAl_2$ precipitates and the potential difference resulting from variations of copper present in solid solution, as suggested by Trzaskoma et al [101] and Brown et al [120]. However, it has been proposed that the primary reason for their poor corrosion resistance is attributable to the deposition of minute particles or films of copper on the alloy surface resulting from corrosion processes[107,125]. These copper 'cathodes' greatly enhance the corrosion of aluminium, resulting in severe attack. If copper ions in solution are out of the range 0.02-0.05 ppm. in neutral or acidic conditions, the pitting threshold of aluminium is exceeded. This form of attack, deposition corrosion, is of greatest concern in acidic conditions (as at the anode) where copper is highly soluble. It has been proposed however that the copper does not

participate to any extent in the corrosion process [125].

SiC particulate and whisker strengthened MMC's exhibit pitting, especially around the SiC, when immersed in water [102]. Metallographic analysis revealed crevice formation at the SiC/Al matrix interfaces, indicating preferential sites for attack. Other investigations report that the SiC/Al interface does not act as a preferential site [101,124,126]. Pit formation was not regarded as substantially detrimental, provided it was not followed by preferential growth and pit propagation.

Wrought extruded rods and SiC in 98.9% aluminium metal matrix model were studied in near neutral deaerated NaCl solution to assess the effect of SiC on pit initiation, structure and growth [126]. The results of the model revealed that pits formed at various sites, but not on the SiC/Al interface. Trzaskoma [126] concluded that the initiation was controlled by microparticles within the matrix and also that the reinforcement addition, if not directly contributed to pit formation, did so by enhancing precipitation of detrimental intermetallic phases [124]. Propagation of pits exhibiting crystallographic features were only observed in the matrix alloy, indicating slow selective attack. In the composite materials, the pits were rounded and smooth, indicating high dissolution rates. From this it was concluded that pit initiation rate was similar for both materials and that the pit propagation rate was higher in composite materials.

The pit size observed on the MMC specimens was much smaller than the matrix alloy counterpart [101,102,124,126]. Pit concentration was also higher and more uniform on MMC's, presumably due to more numerous active sites. Contradictory findings have been reported [70] where fewer pits were observed on 20 vol.% silicon carbide whisker reinforced 2XXX, 6XXX and 7XXX alloys, compared to their matrix alloys. The explanation was based exclusively on pitting around SiC whiskers which, from previous observations, would not appear to be a valid assumption [70]. It can be concluded then that materials and fabrication differences probably account for the disparities between the investigations.

A range of commercial gravity and pressure die casting alloys were subjected to a range

of tests including;

neutral salt spray;

synthetic sea water acetic acid test and

simulated automotive corrosion cycle.

Pit depth was around two to four times greater in the reinforced alloy and no trends were observed between the different test techniques. It was found that gravity die cast alloys suffered preferential pitting at the SiC/Al and Al/Si interfaces. [70]

Typically, metal loss was observed to occur around microparticles in MMC's and base alloys. Newly formed pits exhibited smooth interiors (suggesting that pitting was rapid, in agreement with Trzaskoma [126]) with hemispherical or elliptical openings. In some cases the surface film had been undermined, but it was unclear if it occurred prior to the pitting process as a result of mechanical damage. Work by Trzaskoma [124] is in agreement and suggests that undermining occurs before the pit becomes visible. It should be noted that other work by Trzaskoma [116] also states that tunneling can also lead to features very like those of pits [36]. Pit distribution in the vicinity of the SiC and in the matrix indicated that pitting was not controlled by SiC particles. Micro-particles detected within the pits were found to consist of major alloying components and iron. Alloys prepared by powder compaction and wrought extrusion displayed the same pitting morphology. This suggests that the smaller pits on the composite were due to the SiC inhibiting pit growth, not as a result of the fabrication method. However, there seems no reason to assume that the propagation of pits occurring in the matrix would be impeded by the presence of SiC. Again, pits on the composite exhibited smooth surfaces. In conclusion, we have a two stage growth process:

i) Pit initiation occurred as a result of micro-constituents and resulted in the break-down of the passive film and is the same for alloys and composites.

ii) This was followed by propagation as a result of metal dissolution, but morphological evidence suggests the presence of SiC reinforcement alters the normal growth of the pits.

Typical pit morphologies are depicted in figure 9 [128].

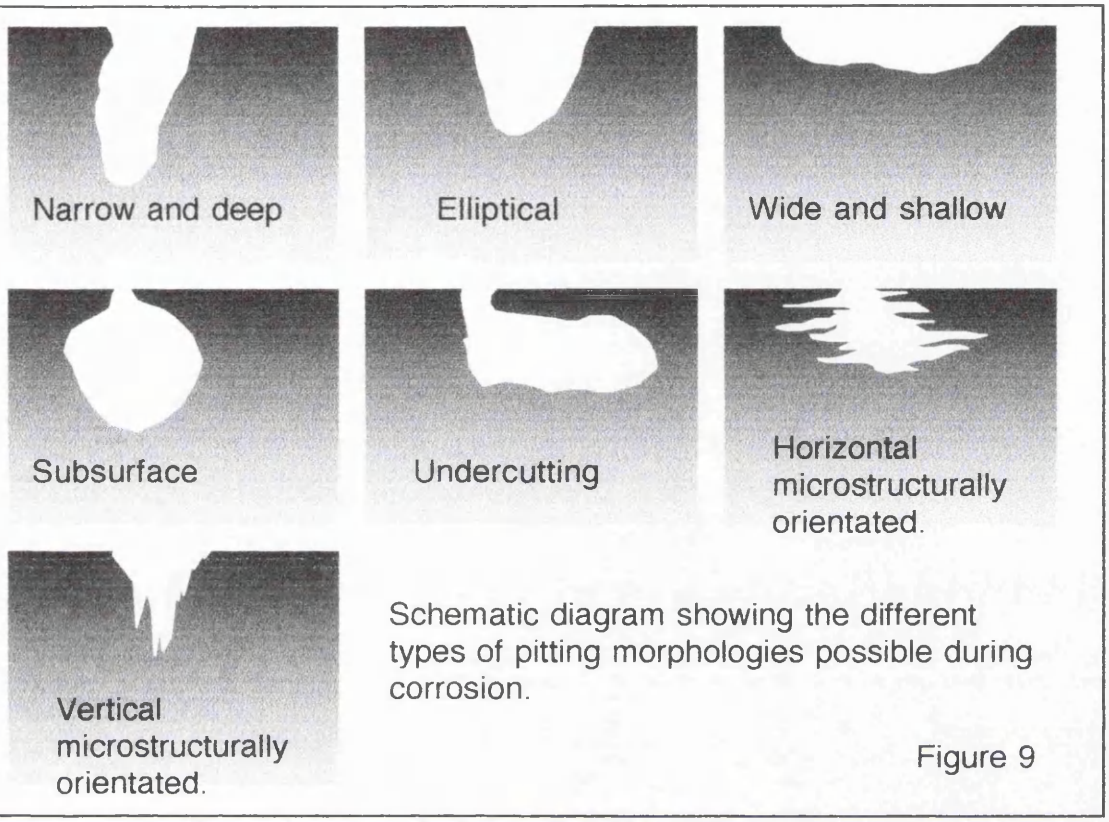

Schematic diagram showing the different types of pitting morphologies possible during corrosion.

Figure 9

Pitting has been observed in the Al matrix at the SiC/Al matrix interface and SiC particle and whisker clusters. It appears that the SiC/Al interface does not necessarily act as a preferential site for attack. Areas for attack appear to be more strongly influenced by the location of active phases in which SiC is thought to play a role.

3.5 Stress Corrosion Cracking.

Stress corrosion cracking (SCC) occurs under sustained elastic tensile stress and a corrosive environment and will result in alloy rupture. SCC occurs in alloys with appreciable amounts of alloying elements, including the 2XXX series aluminium alloys[129]. In aluminium alloys, SCC is usually intergranular and requires an anodic phase at the grain boundaries for crack propagation to occur. Cathodic protection can reduce or eliminate SCC [130] suggesting that it is electrochemical in nature.

The mechanisms proposed for SCC have all been used as the basis for SCC modelling. Localised plastic deformation from applied load is thought to cause disruption of the protective film, promoting electrochemical activity. Sustained selective corrosion due to the inherent tendency of the material to intergranular corrosion, facilitating the ingress of hydrogen into the metal and promotes crack growth [131].

Development of cracking is discontinuous [132]. SCC appears to propagate by a cycle of local cell corrosion followed by mechanical tearing creating a new surface and leading to further corrosion.

Susceptibility to intergranular corrosion is a prerequisite for susceptibility to SCC. Cast aluminium alloys have a very good resistance to SCC. Microstructures tend to be predominantly isotropic, thus not significantly affected by sample orientation. Conversely, the anisotropic structures of wrought alloys result in a marked dependence on specimen orientation [10].

Hydrogen embrittlement is the dominant mechanism of SCC in high strength Al alloys[133]. Hydrogen accumulation occurs at the SiC/Al interface in tensile samples in cathodically charged HCl.

Intergranular corrosion in 20vol% SiC/Al-Si casting alloys in salt spray tests suggests stress corrosion resistance may be reduced, however, in contradiction to this, C-ring samples at loads of 75% of yield strength showed no susceptibility to stress corrosion even after 90 days alternate immersion in 3.5% NaCl [10]. Clearly this area needs more research to resolve this dispute.

The majority of initiation sites for this mode of failure of in service components have been found to be; design induced stress raisers, corrosion pits and fatigue cracks in descending order of scale [129]. A possible reaction for a stress corrosion crack tip for an aluminium alloy exposed to aqueous chloride ions is summarised in figure 10. (*Spiedel and Hyatt (1972)*)

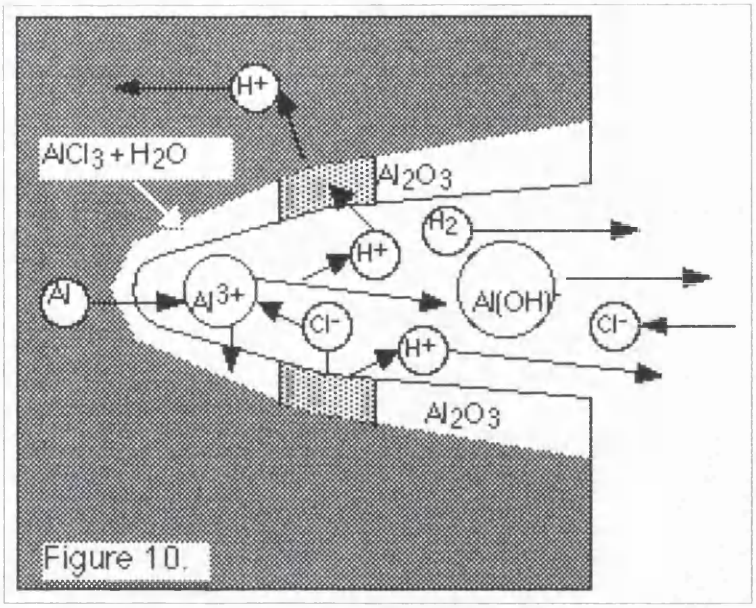

Figure 10. A proposed reaction for a stress corrosion crack tip for an aluminium alloy exposed to aqueous chloride ions.

In summary

1) Reactants are supplied to crack tip. The local solution in this area is generally different to the composition of the bulk solution, resulting in the necessity of reactant transport.

2) Chemical reaction takes place with newly exposed metal. The mechanical fracturing process synergistically interacts with the chemical attack.

3) Adsorption of the deleterious species follows. This includes hydrogen from water, leading to hydrogen embrittlement in the crack tip and accelerated corrosion fatigue crack growth in steel and high strength aluminium alloys.

4) Diffusion of deleterious species to the plastic zone is required. The plastic zone is more susceptible to corrosive attack due to the high concentration of slip bands.

5) Removal of reacted species can occur. Here, the rate of removal is important as the local crack tip chemistry may be affected by the presence of corrosion products and may even alter the local stresses by its physical influence on crack closure [179].

3.6 Exfoliation.

'This occurs in wrought alloys where directionality and elongated grains are apparent, as in rolled or extruded materials. Corrosion proceeds along subsurface paths parallel to the surface. The surface becomes blistered or ruptured by formation of voluminous corrosion product. Corrosion may sometimes proceed along insoluble constituents which have been strung out in the direction of working. Large internal stresses can be generated and thus exfoliation is classed as a form of stress corrosion cracking. However, due to the depth limitation, unexpected structural failures characteristic of stress corrosion cracking, are not the result' (10). Heat treatable 2XXX series alloys are susceptible to exfoliation which, as has been noted, may be detected when examining surface pits (70,124). Robinson (134) has concluded that 'exfoliation corrosion appears to proceed by a stress corrosion mechanism and may be suppressed by applying compressive loads'. Maximum resistance to exfoliation occurs before maximum resistance to stress corrosion cracking in heat treatment, so care must be exercised.

3.7 Corrosion Fatigue.

Corrosion fatigue occurs under cyclic stress and in a corrosive environment. It is dependent on loading, environment and metallurgically interactive variables, consequently there is a wide variety of corrosion fatigue behaviour to be expected from different metal/environment systems. It has been suggested (75) that it is sensible to investigate only specific systems and not to assume results from one system will relate to another. There are however a few similarities between all the extensively researched systems, including:

1) Under corrosion fatigue, the endurance limit of a specimen will be decreased.

2) As the concentration of the aggressive species is increased (up to a certain point), so the endurance limit decreases (109,135).

3) A decrease in cycle frequency increases the crack growth rate (when measured as distance advanced per cycle).[135,136]

4) The initiation process is generally considered to be a pure surface phenomenon and environments which react mainly with the surface of the material are thought to play an important role in the initiation process [109,137,138].

5) Alternating stresses continually disrupt surface films, accelerating corrosion which produces stress concentrations. Hence, the two components cause more damage when acting together than when each acts separately [137,138,139].

6) Several studies have concluded that the environmental factors (mostly due to their time dependence) have a most marked effect in the slow crack growth region [140], and also generally at lower frequencies[141,142].

3.7.1 Initiation.

Dissolution under a cyclic load generally occurs at faces of steps (formed by plastic deformation during a cycle) at the pit surface [143]. The important parameters, according to Pyle et al [143], being the height of the step and the rate of dissolution. The height being of importance because it is a factor in the determination of the magnitude of the crack produced by dissolution in one cycle.

A corrosion fatigue crack will usually initiate at pits or sites of intergranular corrosion [137] on aluminium in chloride containing environments. Initiation occurs normal to the stress direction, but pitting is not a prerequisite in humid air. Several mechanisms have been proposed for the initiation of a fatigue crack [75], including; formation of corrosion pits and consequent stress concentration at the base of the pit, electrochemical attack at plastically deformed areas of the metal with the undeformed metal acting as the cathode, rupture of the surface film with attendant electrochemical attack at the ruptured sites and lowering of the surface energy of the metal due to the adsorption of a specific species from the environment.

It has been proposed by Uhlig [144] that the effect of the corrosion process above the critical rate is to induce or accelerate the plastic flow of the stressed metal and hence to accelerate the formation of PSB's. This effect explains the joint action of the environment and applied stress to produce the maximum observed damage.

Pitting is not a prerequisite for corrosion fatigue. Although it has been observed that those materials susceptible to pitting are also susceptible to corrosion fatigue, corrosion fatigue cracking is also observed where no pitting has occurred. It has been noted that a corrosion fatigue crack does not always initiate at the surface, but can occur near the surface this has been attributed to triaxial tensile stress rupture which cannot occur at the surface. This is succinctly explained in a paper by Haigh and Jones [145]: 'The reductions of fatigue strength often observed when water or other reagents act upon the surfaces of test-pieces during the continuance of fatigue tests are attributed only in a small degree to superficial actions, such as corrosion or notching, and chiefly to diffusion into the metal of foreign substances that provoke chemical or physical change under cyclic stress.' Radetskaya's work [146] on how the state of the surface effects corrosion fatigue concludes that not only is the surface topography of importance, but also the underlying material properties, particularly the state of residual stress. This is most likely due to the effect the residual stresses have on the hydrogen transport processes.

In the discussion on work carried out by McAdam [139], U. R. Evans observes that there are probably several mechanisms in operation during the corrosion fatigue process which may expedite the weakening effects of the corrosion process on fatigue properties. These mechanisms include the build-up of corrosion product, which excludes oxygen and impedes film repair, thereby allowing continuation of pitting. In aluminium, this corrosion product is 1.5 times the volume of the metal and thus, congestion is likely to occur in one of three ways,

(1) to disrupt the metal surrounding the pit,

(2) to force out the corrosion product from the pit, or

(3) to clog the pit and stifle further pitting.

The cyclic component acts on this by aiding film disruption, assisting expulsion and diminishing clogging. The effects of these principles will be discussed further later in this chapter.

It has been found that the initiation of a corrosion fatigue crack can occur at around 10% of the total life of a specimen (147) as compared to 90% in a specimen tested in lab air.

3.7.2 Propagation.

Propagation is influenced by the stress intensity range, load frequency, stress ratio, electrode potential, environment and metallurgical variables (148).

It has been observed (149) that the fatigue of copper in an aggressive environment will increase the height, breadth and number of PSB's, although crack initiation was generally confined to grain boundaries. It was also noted that there is a relationship between cyclic plastic strain, repassivation rate and corrosion fatigue failures.

Figure 11* shows a graph of the idealised response of corrosion fatigue crack propagation rate as a function of the cyclic crack tip stress intensity factor. Mechanisms for stress corrosion cracking, corrosion fatigue and hydrogen embrittlement overlap to some extent, but the crack tip path is generally intergranular in stress corrosion failure and transgranular in corrosion fatigue failure (111,137,141,150). Additions to aqueous solutions which can accelerate SCC growth also accelerate corrosion fatigue growth. True corrosion fatigue crack growth rates cannot be quantitatively estimated by the summation of fatigue crack growth rate in an inert environment and SCC crack velocity under the environment in question (151). At high stress intensities, stress corrosion can dominate overall crack growth per cycle in a corrosion fatigue condition (called stress corrosion under cyclic loading). The change from corrosion fatigue to stress corrosion (denoted by a gradient change in da/dN vs. ΔK) under cyclic loading does not necessarily coincide with K_{1scc}, it can occur at much higher intensities (151).

* Reproduced from Suresh (70).

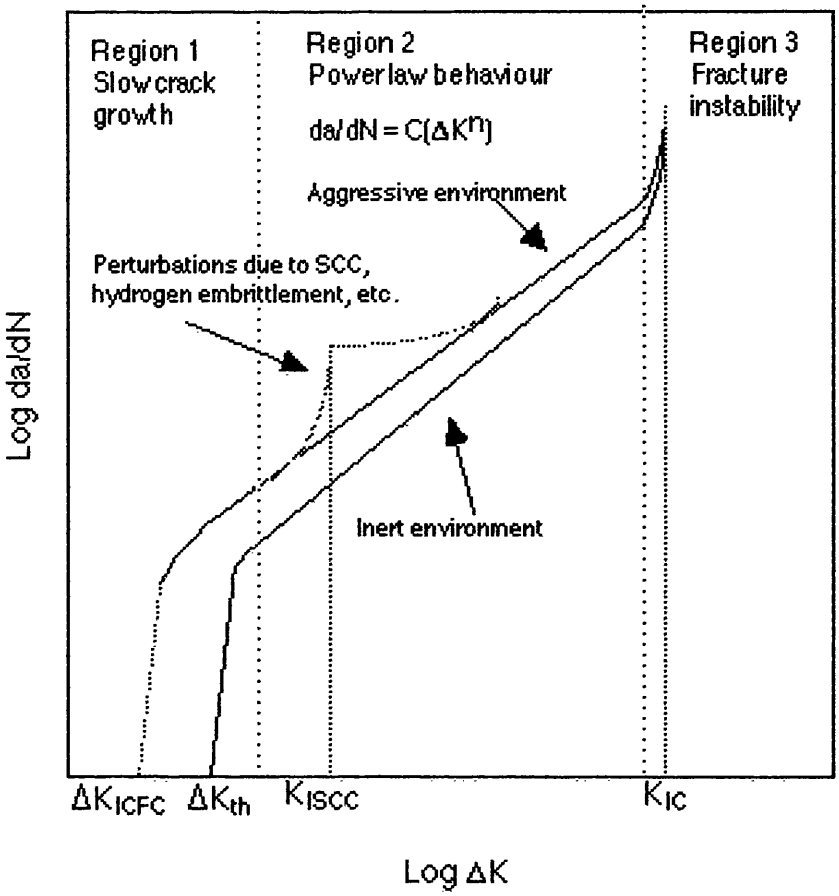

Figure 11. Corrosion fatigue crack propagation rate as a function of stress intensity factor.

A correlation between the surface reaction and the dependence of fatigue crack growth response (below K_{Iscc}) as a function of test frequency and vapour pressure has now been established for several systems, including aluminium-water vapour. Work by Shiozawa (140) has shown that in the low stress intensity factor region environmental factors, such as hydrogen embrittlement have a prevalent role because crack growth rate is slow and the corrosion mechanisms have time to operate. 'For alloy environment systems with 'fast' reaction kinetics, such as the Al-H_2O vapour system, environmental effects are most apparent at low pressures and high frequencies', Wei (152). This study presents a model based on an assumption that enhancement of the fatigue crack growth rate is a result of hydrogen embrittlement, where the hydrogen is a product of reaction between the fatigue crack surface and water vapour (also agreed by Shiozawa (140)), and

as such, the cycle-dependent component of corrosion fatigue crack propagation rate is proportional to this hydrogen production. This means that for these 'fast' systems, there must also be a factor of transportation of environmental elements to the advancing crack tip, in the crack growth rate [82,131,136,154,147,149,152,153]. Marcus et al [155] propose that the rate controlling process is not the transportation of the aggressive environment to the crack tip, or the diffusion of hydrogen ions into the material ahead of the crack tip, but that water vapour was the most aggressive environment and oxygen exerted a minimal effect on aluminium alloys.

As the stress intensity factor increases, Shiozawa[140] proposes that the unpredictable rapid growth of the crack tends towards the normal curve. These observations imply that accelerated testing procedures should be used with caution. Holroyd and Hardie [136] suggest that a simple superposition model such as the one proposed by Wei may be suitable for predicting corrosion fatigue cracking only in some materials.

Trockels et al [141] concluded that there was a strong dependency on frequency and waveform, mainly due to the time dependent processes of hydrogen embrittlement and repassivation. As the frequency decreases, so the time for environmental attack at the crack tip increases. As the frequency reduces below 1Hz however, the slower repassivation process is thought to have more influence, and the propagation rate decreases again. Trockels found that high frequency tests exhibited microscopically brittle fracture surfaces, explained by the effect of hydrogen embrittlement of slip or cleavage planes, in the plastic zone ahead of the crack tip. Low frequencies exhibited more typical ductile fracture.

A review by Gangloff [156] highlights the occurrence of non-steady state crack growth which is unique to corrosion fatigue, and the problems associated with crack closure in modelling corrosion fatigue cracking and the formulation of predictive models, maintained by other work [157,158]. Work by Evans and Lu [150] also observes anomalous short fatigue crack growth behaviour under corrosion fatigue, which they attribute to crack closure, local chemical-electrochemical conditions at the crack tip and interaction of the

crack with microstructural features. Gangloff [156] states that the major experimental problem is the 'lack of methods to probe mechanical and chemical damage processes local to the corrosion fatigue crack tip'.

It is as well to mention however that the acceleration of corrosion fatigue crack growth rates by moisture and sodium chloride solutions may not always be the case. In the presence of chloride ions, especially at high stress, crack blunting can occur resulting in a reduction of the crack growth rate by as much as a half compared to that in air [159,160].

In summary, there appear to be three categories of corrosion fatigue crack growth:

A) An interactive action of both corrosive and cyclic parameters at all but the most rapid crack growth rates where mechanical aspects dominate because cracking is more rapid than the chemical and transport processes involved in corrosion fatigue.

B) No environmental effects are exhibited below K_{1scc}, but above this value, SCC effects contribute substantially to the cyclic crack growth component.

C) Intermediate and extremes of the A and B cases can be observed which appears to be typical of most alloy environment systems. Below K_{1scc}, Type A is prevalent and above K_{1scc}, type B mechanisms are more evident [161].

The fatigue life of 20vol% SiC whisker reinforced MMC is an improvement on the matrix alloy in laboratory air and salt-laden moist air, although salt-laden moist air reduces the lives of both materials[47].

SiC particle reinforced MMC shows a reduced life at a given stress in air for lives below 500,000 cycles, compared with the matrix alloy. In moist air the cross-over point is 100,000 cycles. At higher cycles, similar results are observed for both the unreinforced and particle reinforced alloys in laboratory air.

SiC whisker reinforced MMC's exhibit a superior resistance to fatigue in terms of stress-life than SiC particle reinforced MMC's. The S-N type test is an indication of crack initiation and thus this study only really examines the environmental effect on fatigue crack initiation. The environment exhibits a far greater effect on propagation.

If the fibre/matrix bond is strong, the fibres ahead of a propagating crack may be expected to fail in a brittle manner. In the case of a weak interfacial bond, the energy required to pull the fibres from the matrix may be sufficient to hinder crack propagation. Although a sensitivity to aqueous environments results in faster crack propagation, there were no differences in fatigue crack growth rates of 20vol%SiC whisker/AA6061 samples tested in distilled water and aqueous NaCl. The mechanism of crack growth in the reinforced alloy is therefore determined by the presence of the SiC particles which concentrate strain in the weaker surrounding matrix and act as crack nucleation sites [162,163].

3.7.3 Effects of Material Processing.

It seems reasonable to assume that fabrication and heat treatment affect corrosion behaviour of MMC's more than conventional aluminium alloys due to strain fields and dislocation densities generated during the fabrication of the MMC's. Early work, however, contradicts this.

The reinforcing phase has a strong influence on the dissolution and precipitation of secondary phases, and thus the explanation previously discussed appears to apply: namely, the lowering of E_{pit} for MMC's occurs as a result of enhanced second phase precipitation, with a corresponding depletion of copper from solid solution. The observed increase in the E_{corr} could be due to the presence of course cathodic intermetallic particles on the MMC surface.

Recent work suggests that the corrosion behaviour of MMC's is largely governed by their process history. Some contradictory results may be due to the degree of solution aeration which may be a primary factor controlling the corrosion characteristics of MMC's. Exterior surfaces of extruded SiC whisker reinforced MMC's are more susceptible to corrosion than the core. Elemental segregation between the surface and the core may account for localised attack, but not the enhanced general deterioration of the surface. It is possible that the internal strain energy from fabrication and sample preparation

accounts for this anomaly

Further work in this area has lead to the conclusion that raising the weight percentage of the silicon carbide particles, processing at higher extrusion rates and an increase in solution treatment time raised E_{corr}, even though void content increased. Silicon carbide was thus not thought to play a role in determining the pitting behaviour of MMC's.

Increase in aging time results in a more active E_{pit}. This is due to a decrease in copper content of the matrix through precipitation of $CuAl_2$ and $CuMgAl_2$, i.e. E_{pit} is dependent on alloying elements present in solid solution and not precipitate particles. Unreinforced materials have more active E_{pit} potentials than MMC's reinforced with whiskers at increasing aging times, except at 120 hours where they are very similar. This is probably due to preferential precipitation at and along the SiC/Al interface. Since SiC whiskers are aligned in the extrusion direction, a large number of precipitates are located away from the metal solute interface, reducing the corrosion sites on the MMC surface in comparison to the unreinforced material. At longer aging times, the larger precipitates generate a less protective oxide layer because of inherent discontinuities at the precipitate/oxide/electrolyte interface. This holds true where precipitation is largely in the vicinity of the reactive SiC/Al interface. Although this interface is a site of preferential attack, it is not exclusive. Pit initiation occurs with and without a high density of SiC in deaerated environments.

Rawdon[164] found that sheet Duralumin behaved very differently for cold water quench as compared to hot water quench. He found that the hot water quenched material was more susceptible to intercrystalline attack (which has a marked detrimental effect on ductility) and that this form of attack predominated throughout the test, whereas the cold water quenched specimen initially suffered preferential attack at the grain boundaries, but this changed to pitting (which has a particularly marked detrimental effect on tensile strength) as corrosion proceeded.

Rawdon [164] stresses the importance of frequency [136,156,157,158]. By using a low frequency, the effects of the corrosion component may be more accurately observed.

Fatigue performance of AA2014 and 20vol% SiC particle AA2014 were compared using a fracture mechanics approach [156]. Fatigue crack growth rate (FCGR or da/dN) is a function of crack tip stress intensity range, Δk. It is then independent of geometry and can be used effectively in design. FCGR's were determined using compact tension specimens under constant load amplitude and rising Δk conditions at room temperature in lab air and 3.5wt% NaCl and 3.5wt% NaCl + 0.5wt% sodium dichromate, in both under and overaged conditions.

In the underaged condition, the FCGR was higher in air than the dichromate containing solution. In the overaged condition, the effects of the environment on MMC behaviour were more apparent.

At a given Δk , FCGR in chromate solution is greater than the FCGR in sodium chloride which in turn is greater than FCGR in air.

Intermetallic precipitates surround the SiC particles in the overaged MMC (called matrix shielding) which may largely account for the differences of FCGR's in air between under and overaged MMC's.

In aqueous NaCl and chromate solutions this shielding was overcome due to an increase in matrix environmental attack, resulting in increased FCGR's for overaged MMC's. Unreinforced alloys were more resistant to fatigue crack propagation (lower FCGR's at a given Δk and higher apparent Δk_{th}) compared with the MMC samples. Thus it can be concluded that MMC's are particularly sensitive to chloride ions.

In short, fabrication and heat treatment of aluminium MMC's can exert significant influence on corrosion behaviour and must be carefully controlled to allow valid comparison with unreinforced material and to ensure that susceptibility to attack is minimised.

3.8 High Temperature Degradation.

After prolonged oxidation, AA6061 alloy developed a coherent stable film of magnesium aluminate ($MgAl_2O_4$) which provided a barrier against further oxidation[165]. The respective composite material showed no evidence of magnesium aluminate, but magnesium oxide and silicon carbide. The combined interaction of silicon carbide and sodium chloride (crystal coating before soak) caused continual disruption of the oxide film. Thus, it appears that surface protection is necessary if an MMC is required for high temperature saline conditions. This is in agreement with work by Suresh [47].

3.9 Corrosion Protection.

Corrosion protection may be implemented in one of, or a combination of several ways. By design, environmental change and the employment of barrier coatings. Designs should be considered with respect to the effect of possible corrosive elements either being channelled in to or through areas of high stress or trapped in areas were corrosion will weaken an essential structure.

The basic approaches to prevention of metallic corrosion also apply to the protection of MMC's. These include, the selection of a more resistant alloy, an improvement in component design, cathodic protection by;

a) use of sacrificial anodes

b) use of impressed current

c) use of Alclad products,

the application of coatings which can be inorganic, organic or metallic, the application of inhibitors, the alteration of the environment by;

a) adjustment of pH and temperature

b) agitation or movement

c) deaeration,

or the use of non-metallic linings

The main causes of unexpected corrosion are, improper material selection especially the selection of material in contact with the aluminium, and poor sealing of contact surfaces leading to crevice corrosion.

3.9.1 Cathodic Protection.

Cathodic protection can be implemented by various electrochemical means, involving the a sacrificial anode or impressed current. Although zinc is an appropriate material for aluminium protection, Al-SiC_p composites require other means as its mechanism of protection restricts their useful life. Theoretical electrode potential to prevent corrosion is affected in practice by environmental fluctuations and cathode protection distance ('throwing power'). Careful control ensures good protection and minimises overprotection which can lead to alkali attack (cathodic corrosion).

3.9.2 Chemical Conversion Coatings.

Aluminium oxide film is non-porous, so to increase the oxide film thickness compounds which slightly dissolve the film are incorporated into the solution to sustain the reaction at the metal surface, i.e. chromate or phosphate radicals in acid or alkaline solutions. These coatings are classified as oxide, chromate or phosphate, according to their composition and are usually followed by paint or another organic coating. In comparison to anodising, it is quick and cheap, but also thinner and less durable.

A chemical conversion coating is formed by means of a chemical reaction between a metal surface and a solution, where the metal forms a compound found in at least part of the coating.

On immersion of aluminium into boiling water, the porous oxide layer can thicken where

the water can reach the metal surface. Chemical oxide coatings follow this same principle.

Figure 12 shows a schematic representation of the structures of pretreated films.

a) shows a chromate pretreatment and b) shows a chromate/phosphate pretreatment.

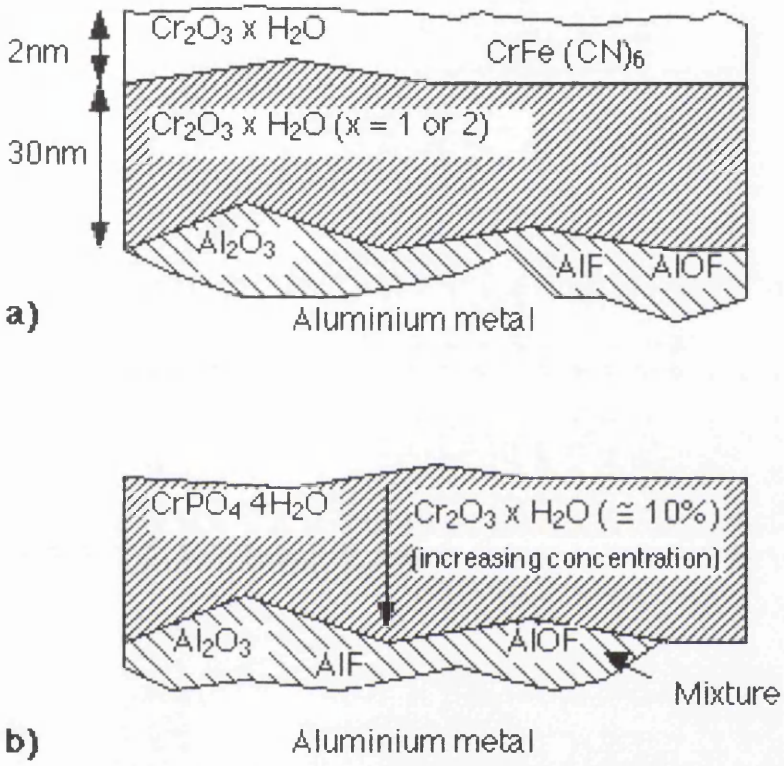

Figure 12. Schematic representation of conversion coating structures.

Immersion of a component in a 3% sodium carbonate and 1.5% sodium chromate solution at 90 to 100°C for three to five minutes is the basis of what is called the Modified Bauer-Vogel (MBV) process.

The composition of the coating is between alumina and aluminium hydroxide,

$Al \Rightarrow Al^{3+} + 3e^-$

$3H_2O + 3e^- \Rightarrow 3OH^- + 3/2H_2$

$2Al^{3+} + 6OH^- \Rightarrow Al_2O_3.nH_2O + (3-n)H_2O$

Chromate inhibits alkaline solution attack on metal oxides and alloying elements, e.g.

$2H_2O + 2Al + 2CrO_4^{2-} \Rightarrow Al_2O_3 + Cr_2O_3 + 4OH^-$

The final coating is porous and provides a good base for paints and topcoats.
Topcoat durability can be enhanced by treating the coated surface with silicate for improved abrasion resistance, or chromate solution for corrosion resistance. Alkaline oxide coatings are rarely used compared with chromating and phosphating treatments.
Acid chromate, acid chromate/phosphate and acid phosphate solutions are more complex coating processes in terms of the reactions occurring in the solution during film formation.
In practice, corrosion resistance of chromate coatings is superior to chromate/phosphate and phosphate coatings in salt spray conditions below 60^{0}C due to the chromium being leached from the coating to protect the metal. Above 60^{0}C the chromium compounds are rendered insoluble and thus protection decreases.

3.9.3 Anodising.

This is an electrochemical process which converts aluminium to aluminium oxide where aluminium is the anode in the electrical circuit. The low conductivity of aluminium oxide ensures that the metallic substrate polarises anodically leading to oxide thickening. The resultant oxide layer is thin and non-porous at the metal/oxide interface, but possesses a porous outer layer.

Anodising is classified according to the acid electrolyte used, often sulphuric and chromic acids. Further improvement of corrosion resistance for surfaces anodised by these acid is to seal the surface by hydrating the aluminium oxide coating causing swelling, and thus pore closure. Organic topcoats are often used, especially where anodising is for decoration.

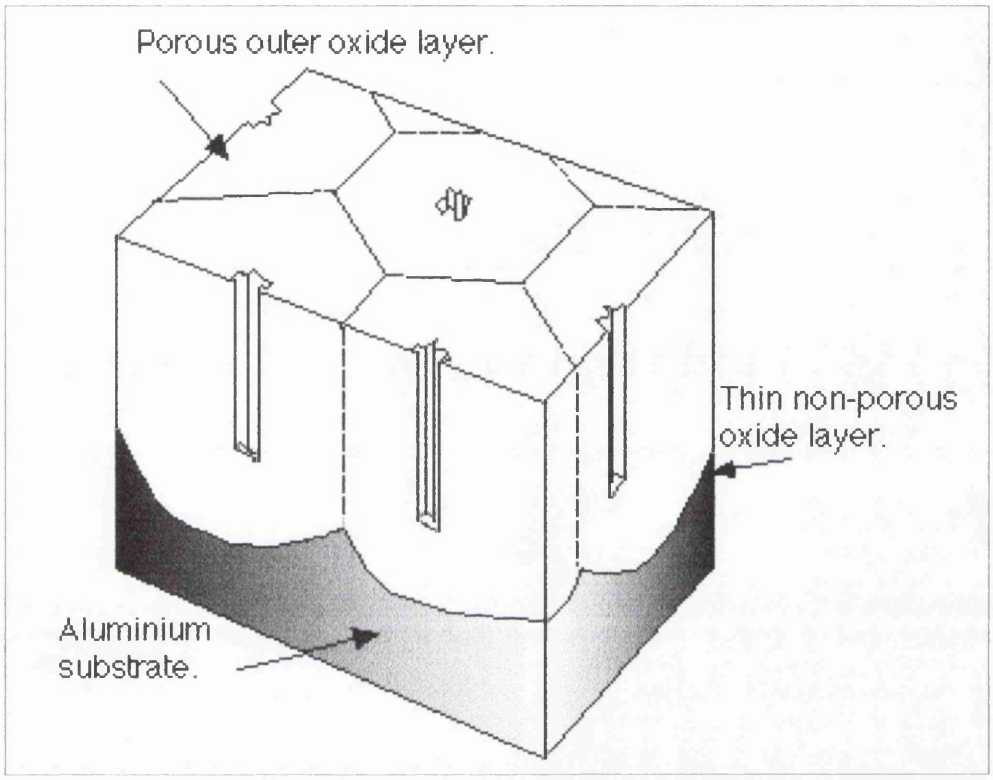

Figure 13. Showing the cellular structure generated by anodising [43].

CHAPTER 4.

4. Testing Procedures.

4.1 Tensile Testing.

This type of testing is generally carried out on rectangular or round cross section specimens, but Roebuck (165) observes that the rectangular cross section specimens in conjunction with two longitudinal strain gauges generally generate a more accurate response for MMC measurements. He also noted that the use of knife edged contact points on a non-ductile material such as MMC can cause inaccuracies of unacceptable levels and notes that the development of effective non-contacting extensometry is required. Care should also be exercised when setting the specimen into the test rig as misalignment may cause vast inaccuracies.

4.2 Corrosion Fatigue Testing.

Corrosion fatigue testing is usually carried out on samples of a specified geometry in order for ease of machine design and comparison of results between researchers. However, this is not a necessity and in some cases structural components or prototypical hardware has been subjected to fatigue testing. The samples upon which this type of testing are generally carried out are simple configurations with well defined states of loading (159). Most corrosion fatigue experiments load the specimen either in bending or uniaxially. Torsional and complex multiaxial states are uncommon.

The rotating beam machine produces a constant moment in the test section with fully reversed sinusoidal loading on the surface as the specimen rotates. Hourglass cylindrical specimens are used either with or without a circumferential groove. This type of testing is restricted only to cylindrical specimens for obvious reasons and the mean stress imposed on the specimen is always zero (fully reversed).

A common form of testing procedure is repeated bending of the specimen with a cantilever 3 or 4 point bend loading. Loading is generally mechanical, using a rotating adjustable cam or crank, resulting in a fixed displacement of the specimen. If load control is required, a closed loop electro-hydraulic system may be employed. The test pieces for this type of procedure can be a wide variety of cross-sectional geometries and sheet and plate specimens of rectangular cross section are frequently used. This method is commonly employed because of its simplicity, versatility, reliability and simple implementation, however, if yielding of the specimen occurs, the peak stress and strain are hard to determine. Also, with fixed deflection loading, the applied tensile load decreases as cracking occurs in the specimen, thus reducing the propagation rate (compared to the application of load controlled loading) even as far as crack arrest or non-propagation.

Uniaxially loaded specimens are most commonly used for corrosion fatigue research. The specimens can have a variety of cross-sectional shapes, various mean stresses can be employed and axial stresses and strains within the specimens can be easily measured and clearly defined.

The test machines for axial loading, however, are complex, prone to breakdown and costly to operate, but their advantages are seen to offset these problems. Axial loading can be driven by a variety of mechanisms, the most common of which being mechanical and electrohydraulic systems. The mechanical systems are generally used to conduct sinusoidal axial loading (constant amplitude). Cyclic loading controlled by an adjustable cam, connecting rod and lever with a hydraulic load maintainer (to compensate for small changes in specimen length) is an economical system but is suited only to long life fatigue testing where the cyclic stress strain response is nominally elastic.

The most widely used however is the closed loop, servo-controlled electrohydraulic system. This enables programming of the variable measured by the transducer to follow any waveform produced by a signal generator. In this manner, variable amplitude loading histories may be imposed on the specimen, mimicking more closely real service

conditions.

The most common types of axial load fatigue specimens are circular or rectangular cross-sections, with the test section area either a constant size (resulting in uniform axial stress in the gauge length) or an hour glass profile (resulting in a maximum axial stress at the minimum cross-sectional area). The specimens may be clamped or machined with threads, button-ends, pin holes or bolt holes for connection to the loading fixtures. The specimen may also be fabricated with welds, notches, or a variety of other incorporated fabrication defects and tested in the as machined state with polished or other surface conditions, in order to simulate service applications.

4.3 Crack Growth Testing.

Fatigue crack growth studies employ the machines as described above, with the exception of rotating beam machines. The standard types of specimen used in this type of study include compact tension (CT), centre cracked tension (CCT), single edged notch (SEN), double edged notch (DEN) and surface flaw specimens[165], all of which (excepting the foremost) are also suitable for corrosion fatigue crack growth testing.

Obviously with the introduction of an environmental influence there are other variables to be taken into consideration. The solutions generally employed in the studies of corrosion fatigue include; fresh natural seawater, seawater with the organic species removed, synthetic seawater solutions, brackish water and sodium chloride solutions (generally 3-5 percent by weight [166]). The application of these solutions may also be varied. Tests may involve total immersion of the specimen in the aqueous solution, dripping or spraying onto the specimen surface or alternating wet and dry conditions. Application and testing is generally carried out in polymer chambers in order to prevent contamination with undesired metallic ions and prevent possible oriented galvanic effects.

In the test situation, important measurable variables include; solution composition, flow rate, temperature, percentage of dissolved oxygen, acidity, pressure and electrochemical potential.

The corrosive medium may be applied manually, but with the advent of automisation of spray/fog chambers, this is more convenient for application seven days a week and 24 hours a day.

The polymer spray/fog chamber itself must be rigged up to both a solution reservoir and a compressor or compressed air supply. The chamber itself should contain an atomising nozzle which should not be aiming the spray or fog directly at the specimen. A more detailed account of the test rig and procedures may be found in A.S.T.M. B. 287-74 [167] and A.S.T.M. B. 117-73 [168].

4.3.1 Crack Measurement Techniques.

Many different types of procedure have been developed for the measurement of fatigue crack growth. Some of the advantages and disadvantages of some of the most widely used techniques [70,165,169] are summarised here.

4.3.2 Optical.

Using a microscope to measure the progress of the crack along the surface of a specimen. This is an inexpensive method with no need for calibration, however, it may lead to inaccurate measurement of the crack length as it does not account for crack curvature. It is also time consuming and requires a visually accessible surface.

4.3.3 Crack Opening Displacement Techniques.

This method is expensive for testing in aggressive environments as the clip gauges and

transducers are not very robust. The time dependent, time independent and reversed plasticity effects must be small. However, it does account for crack front curvature and is easily automated.

4.3.4 Back Face Strain Measurements.

Strain gauges measure strain in compact tension or T-type specimens. Changes in crack length of 10 μm can be resolved and the process is easily automated. The cost is high though for aggressive environments and as for crack opening displacement the time dependent, time independent and reversed plasticity effects must be small.

4.3.5 Crack Tip Strain Measurement.

Surface mounted strain gauges measure the the strain close to but behind the crack tip on bend specimens. This inexpensive method is capable of detecting initiation, but is limited in thick specimens where surface events do not reflect crack growth in the interior. Large scale plasticity can be accounted for, but the onset of general yielding makes interpretation difficult.

4.3.6 Electrical Methods.

a) Strain Gauge Filaments.

Electrically conducting wires are attached to the specimen such that the passage of the crack tip fractures them, producing a stepwise change in resistance. This inexpensive procedure is easily automated, but is not suited to aggressive environments. Difficulty also arises in location of the gauges such that they are broken by crack tip passage, and only the crack tip.

b) Direct Current Potential Difference.

A constant direct current is passed through a specimen such that the crack length alters the potential difference between two contact points either side of the crack. This method is robust and moderately inexpensive. Average crack lengths can be produced and the method is well established for certain specimen sizes and geometries. The system is highly stable, suited to automation and small relaxations from linear elastic behaviour are easily accommodated. However, this method does not distinguish between crack extension and changes in the external surface dimensions of the specimen, as in general yielding. Also, although some theoretical calibrations are available, the relationship between the potential difference and crack length are complex and calibration tests are usual. There is also uncertainty over the use of this method in stress corrosion and corrosion fatigue studies as there is a possibility of interference with the electrochemical processes occurring at the crack tip. For decreasing stress intensity/constant crack opening displacement tests, the crack faces may also short electrically, producing a low crack length estimate. Similarly, crack bridging by corrosion products may influence results. This method is not suitable for large specimens. Finally, the loading grips may also have to be electrically insulated from the testing machine.

c) Alternating Current Potential Difference.

Methodology as with the direct current. The calibration for this method is simple for different specimen geometries as there is a linear relationship between the output and the crack length and no test piece size dependence. This method is robust as it does not require the attachment of delicate instrumentation. High sensitivity can be achieved compared to the direct current method and automation and average crack length values are achievable. The most significant advantage of the AC PD system is its ability to reject

noise and drift during signal processing. The major drawbacks to this method are that connecting wire must be carefully situated and not moved during the test procedure because of lead interaction effects and the cost is moderately high. As with the direct current method, crack bridging by corrosion products may influence results and electrical insulation of the specimens is required.

The system has several advantages over the DC PD system. Thermally induced emf, resulting from dissimilar metal junctions are avoided using AC systams. A lower operating current is required to obtain the same measurement sensitivity as the DC system because of the high noise rejection and excellent signal to noise ratio at high gain available with the AC system. Also, the effect on electrochemical processes associated with cracking phenomena are minimised with the AC PD system.

d) Eddy Currents.

The eddy current probe placed adjacent to the cracked surface produces an electrical signal indicating the crack. One system involves a servo-system or stepping motor that moves the probe in such a way that a nil eddy current signal is maintained. This system is easily automated, but, it is expensive and only produces surface measurements.

Other methods of crack measurement include ultrasound measurements and acoustic emission.

CHAPTER 5.

5. Summary of Literature Review.

Incorrect processing of SiC/Al can cause detrimental Al_4C_3 formation, which is readily hydrolysed. This can be remedied in MMC castings by addition of excess silicon.

It appears that the corrosion resistance of SiC/Al MMC's is inferior to that of its base material due to the detrimental effects caused by the particles. Their action as nucleation sites for phase precipitation and hindrance of a coherent, non-porous oxide film growth are thought to be responsible for the increased occurrence of pit formation at and near the reinforcement and its interface.

Looking at the problem at its basest form, the effects of particle addition can be summarised in two different ways.

Either the high dislocation density produced from thermal mismatch yields high degrees of lattice strain, providing sites for preferential stress corrosion cracking, or, SiC hinders crack propagation by stress relaxation due to crack branching.

On the evidence presented in the literature review, it is apparent that despite the strength and stiffness advantages gained in the particle reinforced systems, in-service capabilities could be severely affected by a sensitivity to general environmental conditions and chloride containing conditions in particular.

This sensitivity is a realistic threat considering the known poor response of monolithic aluminium alloys to these conditions, and the discontinuous nature of the metal matrix composites: soft matrix and hard particle reinforcement.

The predictability of this type of corrosion remains a problem. There are indications that the electrochemical nature of the phenomenon may lead to an electrochemically measured predictive solution, but there are some difficulties in this method, particularly that there is a lack of accurate testing procedures and equipment to observe the

processes occurring at the crack tip.

The problems encountered in modelling the processes relate to the physical problem of obtaining the measurements, but also the probability that accelerated testing may well give an inaccurate impression of the environment/component response over a long period of time.

On this basis it is proposed that a major area requiring research is the fatigue response of these materials under a variety of environmental conditions.

Part 2. Aims Of The Project.

The project will encompass the following experimental programme:

Fatigue testing of cylindrical specimens presoaked in a salt solution for various lengths of time. This will determine the optimum presoak time for the specimens tested in the remainder of the programme.

Fatigue testing of specimens in air, salt fog and after a salt solution presoak, in order to determine environmental influence on fatigue performance.

Crack propagation testing in air and salt fog atmospheres employing a direct current potential difference crack length measurement method. The specimens employed will be 10mm x 10mm square cross section with a 0.3mm starter slit. From this, the Paris exponents may be calculated for each test to determine the influence of material type and the effect of an aggressive environment on crack propagation.

Testing will be carried out on base matrix material and both mechanically (Xe) and blended (Xh) materials.

The comparison between the base metal results and composite results will determine the effect of particle addition, which is significant to production as the benefits must outweigh the expense of particle addition.

The comparison between the results of the two alloying techniques will determine their effect. The possible difference in dispersion of the particulate within the base material, the effect of the breakdown of the SiO_2 particles in the mechanically alloyed material and whether these SiO_2 particles have a detrimental effect on the corrosion fatigue properties of the composite materials. There is a significant difference in the cost of production between mechanically alloyed and conventionally powder blended materials, hence the importance of investigation into the benefits of the more expensive processing route in terms of fatigue life in an aggressive environment.

Part 3. Experimental Procedures.

1. Materials.

All the materials were supplied by DERA/Aerospace Metal Composites Ltd. and were of commercial grade. AMC metal matrix composites are formed by powder metallurgy methods. They are high quality, inert gas atomised, aluminium alloy powders plus ultra fine silicon carbide particles with an average diameter of 2-3 μm. The powders are either blended (Xh) or mechanically alloyed (Xe). Both processes allow thorough mixing of the silicon carbide particles with the matrix material and thus a high degree of uniformity of the properties throughout the final product. Consolidation of the material is achieved through solid state compaction by hot isostatic pressing, avoiding the formation of aluminium carbides (eg. AL_3C_4) which can be detrimental to the mechanical properties of the end product. The manufacturing process is carried out in a controlled inert atmosphere to reduce oxidation and maintain the purity of the product.

Secondary processing by conventional wrought methods, such as forging, rolling, machining and extruding, may be carried out to form near net shape of the final product.

The material studied, AA2124, is an aerospace alloy. AMC200 is the matrix material, AA2124, with no further additions. AMC225 is a silicon carbide reinforced material with 25 volume % silicon carbide particles in an AA2124 matrix. Table 1 shows the composition of a typical AA2124 alloy and the AMC200 base material.

The material was supplied in the form of 25mm diameter extruded bar stock. Representative sections were prepared and examined using optical and scanning electron microscopy to confirm particle size, volume fraction and distribution were within the manufacturers specifications.

Element	Cu	Mg	Mn	Others	Al
AA2124 weight %	3.8-4.9	1.2-1.8	0.3-0.9	<1.1	Remainder
AMC200 weight %	3.86	1.51	0.59	<0.18	Remainder

Table 1.

1.1. Heat Treatment of the Materials.

The bars of material in the as supplied (T1) condition were cut to length, typically 80 and 110mm length blanks, and some were given a T4 heat treatment. This required heating to 505°C for 2 hours, followed by cold water quenching and natural aging at room temperature for 5 days.

This resulted in the six conditions of alloy summarised in table 2.

Alloy designation	Processing route	Heat treatment	SiCp
AMC200	Mechanical alloying	T1 and T4	-
AMC225Xe	Mechanical alloying	T1 and T4	25%
AMC225Xh	Powder metallurgy	T1 and T4	25%

Table 2.

2. Pit Characterisation.

Discs were cut transversely from the bars and half were ground using 240, 320, 600 and 1200 grade grit paper for three minutes each, then polished to a mirror finish on a polishing cloth with 1mm diamond dust. All the discs were then degreased and soaked in 3.5wt% sodium chloride (NaCl) dissolved in distilled water, for various lengths of time, from zero up to 168 hours (1 week). The discs were rinsed in ethanol on their removal from the

solution and dried in warm air. These discs were examined on the Reichart light microscope which is calibrated so that measurements of the pit depths can be taken by focusing between the surface of the material and the pit bottom. Pit depths were noted and recorded for each of the soak times and photographs taken of the surfaces of the specimens.

Blended BP217 material, from an earlier batch of I. R. C. material, was also examined. This material is similar in composition to the AMC225 material, with SiC particles typically of 2-3 μm in diameter and at a volume fraction of 17 vol%. Some of these disc specimens were also cut in half diametrically and polished to a mirror finish. These specimens were then cleaned and examined using the J.E.O.L. JSM6100 scanning electron microscope and photographs taken of the pits found in cross-section.

3. Test piece Design.

Two test piece designs conforming to relevant testing standards and commonly used at IRC Swansea were employed during this investigation. A plain cylindrical specimen, as shown in figure 14, was used to investigate load controlled low cycle fatigue response.

A square cross-section corner crack design (figure 15) was used to investigate fatigue crack growth response.

All the specimens were machined using poly-crystalline diamond tooling under CNC machine control.

4. Fatigue Testing Procedure.

Each of the material types underwent fatigue testing under varying conditions. The sample type is depicted in figure 14. The R-value (minimum stress/maximum stress) was 0.1 and the frequency was 1 Hz, under a simple sinusoidal waveform on an Instron servo-hydraulic

testing machine. Additional testing included frequencies of 10Hz, 0.1Hz and an R-value of 0.5.

Tests involving prior soaking of the specimen were degreased, completely immersed in the 3.5wt% sodium chloride solution (as previously specified) at laboratory

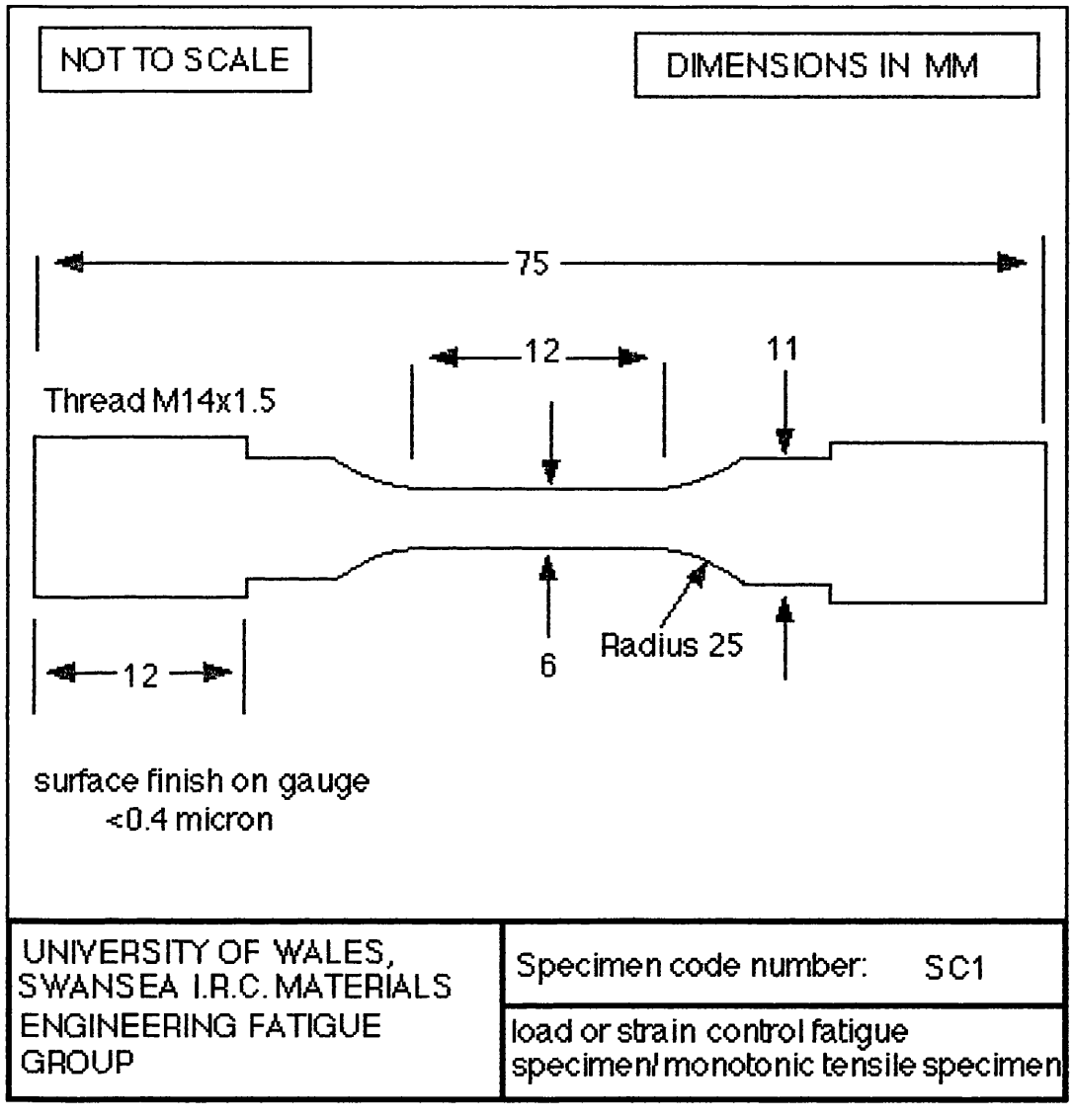

Figure 14. LCF specimen design

temperature and under zero load. They were then rinsed in ethanol, immediately dried in warm air and tested. The intention of the soaking treatment was to introduce environmental damage in the form of corrosion pitting. The testing procedure employed complies with British standard BS3518(180).

Tests involving a fog atmosphere were also degreased before testing in a salt spray chamber from C & W specialist equipment Ltd., (model SSHC). The test rig complies with ASTM B117, BS 390 F12 and DIN 50.021 standards. The chamber monitored and controlled the flow rate of the salt solution (as previously specified) at 0.1 litres per minute and a temperature of 20^0 C($\pm 1^0$ C).

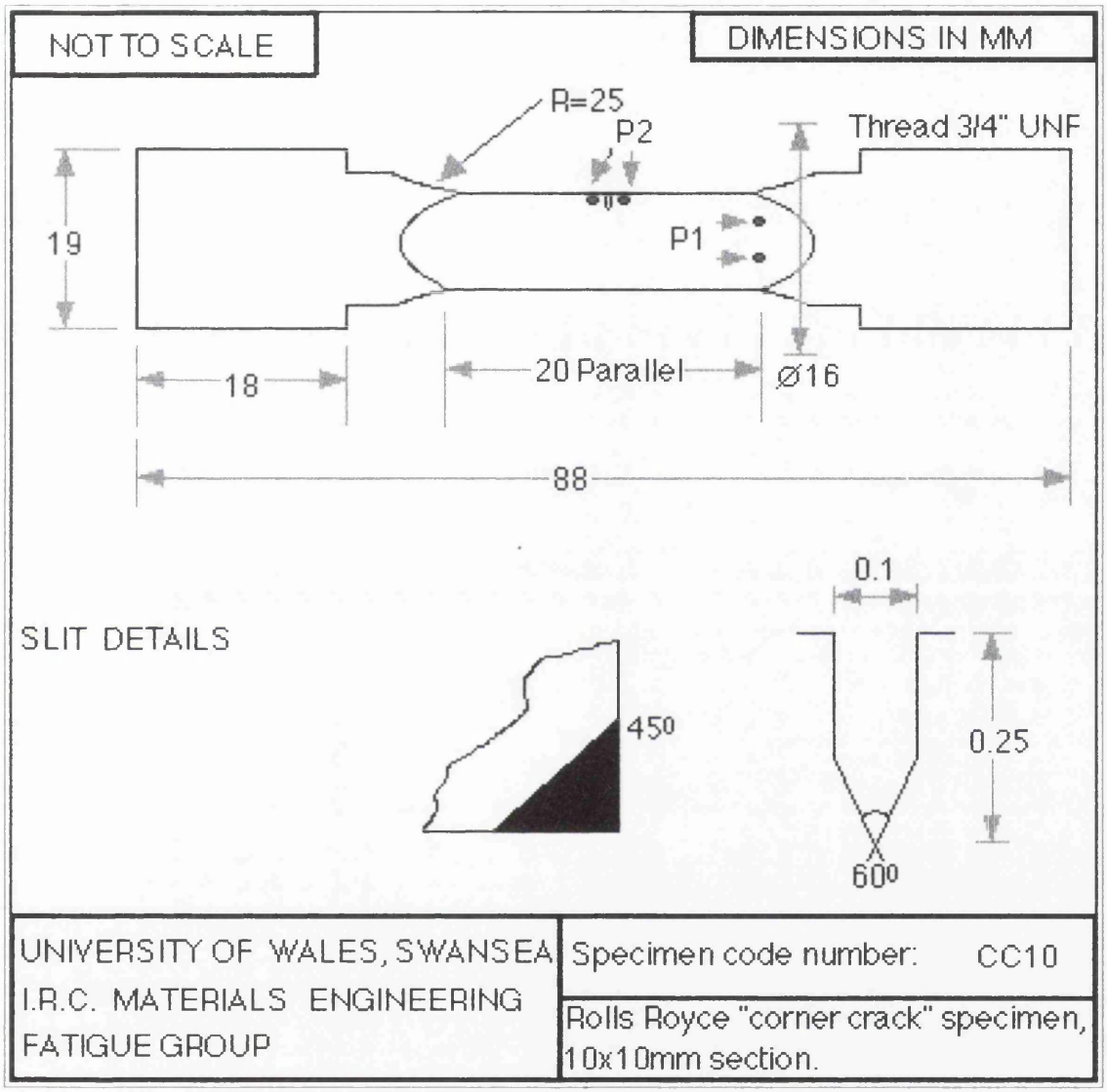

Figure 15. Corner crack specimen design.

P1- The reference wire position. P2- The slit wire position.

4.1. Summary of the Fatigue Testing Programme.

AMC225Xe T1, tested in air, a salt fog atmosphere and in air after a 24 hour salt presoak.

AMC225Xe T4, tested in air, a salt fog atmosphere and in air after a 24 hour salt presoak.

AMC225Xh T1, tested in air, a salt fog atmosphere and in air after a 24 hour salt presoak.

AMC225Xh T4, tested in air, a salt fog atmosphere and in air after a 24 hour salt presoak.

AMC200 T1, tested in air.

AMC200 T4, tested in air and a salt fog atmosphere.

AMC225Xe T4, tested in a salt fog atmosphere at an R-value of 0.5.

AMC225Xe T4, tested in a salt fog atmosphere at 10 Hz and 1 Hz.

Another set of tests involved soaking AMC225Xe T4 specimens in the NaCl solution for 8, 24 and 72 hours, and each of these soak times was fatigue tested at 450 MPa and 350 MPa on a Mayes servo-mechanical "screw" testing machine at a frequency of 1 Hz using a simple sine wave form and an R value of 0.1. These results were plotted as life to failure (number of cycles completed) against the soak time. Similar tests examining the fatigue behaviour of the blended BP217 material, from the earlier batch of I. R. C. material, was also examined and the fracture surfaces observed as above.

5. Crack Propagation Testing.

The corner crack (CC10) specimens were tested in compliance with BS6835[181]. Potential drop monitoring was carried out using 0.3mm diameter , insulated probe wires which were attached to the specimen by means of a 50 Watt spot weld (Hughs Aircraft Company VTA-60) The welding current was set at 2-2.5 amps. The specimen dimensions and probe wire positions for the potential drop techniques are shown in figure 15. Electrical connections were checked using a resistance meter on an Avometer multimeter. This was repeated after the specimen had been placed in the servo-hydraulic set-up. Crack growth was monitored from the starter split with the aid of a pulsed direct current potential drop

current supply set at 50 amps. A load controlled 1Hz sinusoidal waveform at R=0.1 was employed exclusively throughout these fatigue crack growth tests which were conducted in laboratory air and 3.5% NaCl fog. A range of maximum stress levels (175 to 250MPa) were used. A record of Pd voltage as a function of cycles was recorded throughout each test. Cracks were interrupted prior to complete specimen rupture and acetone replicas were employed to measure the crack lengths. Since the potential difference monitoring system being employed reasonably insensitive with respect to the specimen design using the materials under consideration, there was a minimal difference between life to total failure and any arbitrarily defined cycles to initiation, especially since the stress levels involved are at the upper limitations of the fatigue properties of the materials.

Optical measurements were taken in some cases in order to assess crack path-particle interactions, grain size-crack path interactions secondary cracks and crack path deflections. Other advantages of this system are that it is relatively inexpensive and does not require complicated calibration. However, there are disadvantages. The system only provides surface crack measurements which does not account for crack curvature and may be unrepresentative of the behaviour, particularly in inferior specimens. The method is also time consuming and requires the specimen surface to be accessible and in a well cleaned condition. It is usually necessary to stop the test to take photographs and to clean the surface of the specimen with grinding paper and acetone. This may affect the crack propagation process and provide invalid data. The optical system used consisted of an Olympus OM2 35mm camera mounted on a Zeiss metallographic microscope. From the negatives, crack length could be obtained from an enlarged image of the crack profile, using a standard 35mm enlarger. The optical system was used in the detection of crack initiation, crack growth and crack particle interactions using CC10 specimens.

6. Fractography.

All fatigued specimens were kept in a desiccator until they could be examined in the electron microscope. The fractured specimens underwent sonic cleaning in ethanol for several minutes. They were then rinsed and dried in warm air before insertion into the electron microscope. Particular attention was paid to the initiation points and pitting on the sides of the specimens. Some photographs were taken as a permanent record of any interesting features.

It is important to note that due to the testing procedure used for the fog atmosphere tested specimens, it was not always possible to prevent the fracture surfaces from corroding after the failure of the specimen. In many cases this was severe enough to make fractographic analysis difficult or impossible as it is difficult to remove the corrosion product without damaging the underlying structure. Even where corrosion product removal was possible, however, the surfaces show little of the original fracture features as these were obscured by the subsequent corrosion process.

7. Tensile Testing.

These tests were carried out using the SC1 specimens (figure 14) on a Mayes Servo-mechanical "screw" testing machine, using a surface mounted extensometer set to a 10mm gauge length on the central region of the specimen gauge. The specimens were tested to failure when loaded at 1mm per minute.

1. Results of Mechanical Testing.

The individual stress/strain graphs for each of the alloys can be seen in appendix 1.

Figure 16 below summarises the stress/strain response of all of the materials tested.

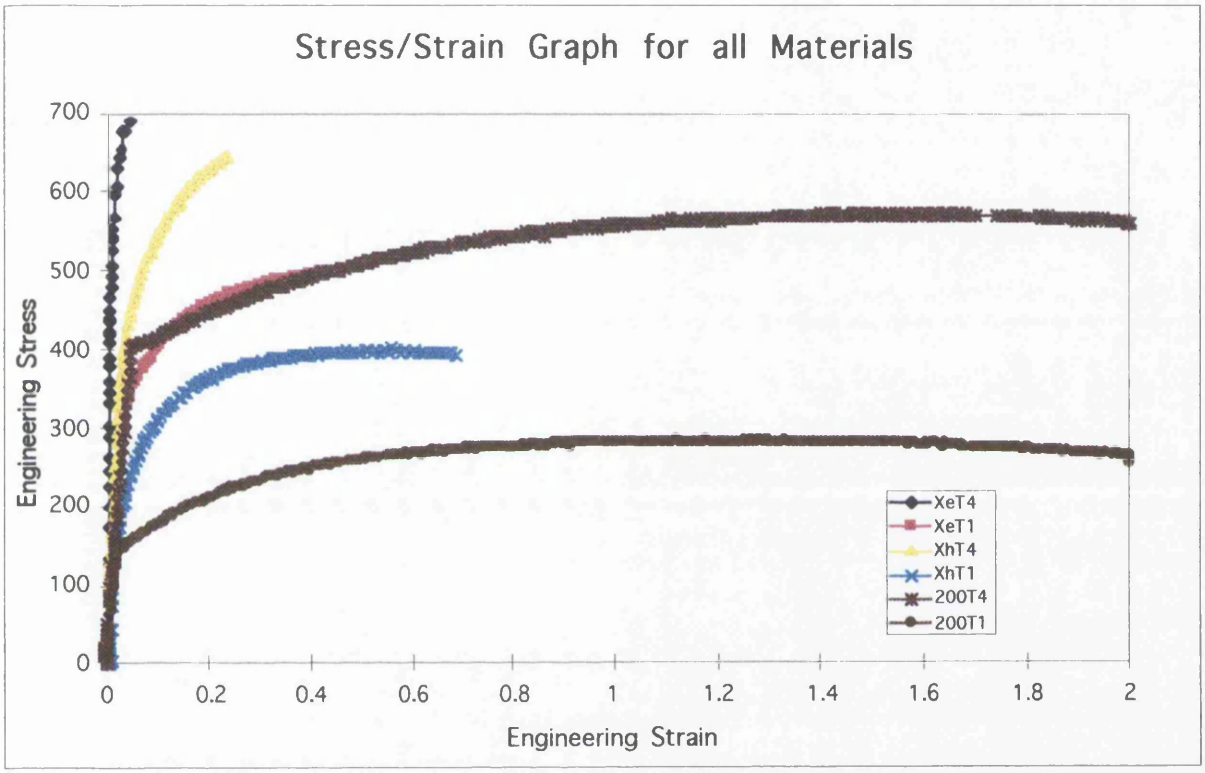

Figure 16.

The key information measured from these graphs is recorded in Table 3.

Material	E (GPa)	UTS (MPa)	Y.S. (MPa)	strain to failure
200a-T1	78	290	142	2.00
200a-T4	74	570	405	2.00
Xe-T1	119	500	220	0.43
Xe-T4	160	700	470	0.04
Xh-T1	12 2	400	140	0.69
Xh-T4	119	640	360	0.23

Table 3.

2. Results of Load Controlled LCF Testing.

The results for all load controlled LCF tests are tabulated in . LCF testing was carried out in air, after soaking in a saline solution or in a saline fog atmosphere under 10, 1 and 0.1Hz sine waveforms and R values of 0.1 and 0.5. The data have been plotted in the form of S-N curves in order to make relevant comparisons between the data sets. The peak stress is plotted against the number of cycles undergone by the specimen. Where R-ratio is variable between data sets, a stress range graph has been plotted in order to accommodate the fact that stress range is the driving factor in fatigue crack growth.

2.1. Results for Baseline Data, AMC225Xe Material.

The results from AMC225Xe T4 heat treated material have been plotted in figure 17 (p.88). The best fit curve has been superimposed "by eye" as the number of data points available is too few to enable a meaningful statistical fit.
This data describes a typically sloping curve with an endurance limit of approximately 465MPa.

2.2. Heat Treatment Effects.

The effect of heat treatment has been illustrated in figure 18 (p.88), where data for air tested T1 and T4 materials have been plotted. The T4 material shows a stronger fatigue response at the high stress/low cycle end of the fatigue curve. This becomes less apparent at lower peak stresses. The T1 material was found to have an endurance limit of about 350 MPa, approximately 75% that of the T4 condition.

Figure 19 (p. 89), showing Xh response to heat treatment displays a similar response to heat treatment as the Xe material, with the T4 condition exhibiting a stronger fatigue

resistance, and an endurance limit below 400 MPa. The endurance limit for the T1 material is about 300 MPa.

The effects of heat treatment on fatigue resistance for the base alloy are shown below in figure 20 (p.89). Again, it is clear from the graph that the T4 heat treatment confers a greater fatigue resistance on the base alloy.

2.3. Effect of Processing.

The effects of processing presented in figure 21 (p.90) show a close correlation between the powder blended and mechanically alloyed materials. The blended T4 material shows a slightly weaker response at high values of peak stress which is reflected in the T1 material, compared with its mechanically alloyed counterpart. The base material is significantly weaker when compared to the corresponding heat treated composite materials, with endurance limits of 200 (T1) and 350 (T4) MPa.

The T1 treated alloys, all of which display a lower fatigue strength than the T4 treated materials, show a similar trend with the blended material exhibiting a slightly higher strength than the base alloy and the mechanically alloyed material.

2.4. Environmental Effects.

Figure 22 (p. 90) shows the fatigue response of mechanically alloyed T4 composite tested in air, salt fog and after a salt solution presoak. The fatigue strength of the alloy is significantly reduced on exposure to saline conditions. The presoak data display a considerably greater degree of scatter than those in the fog environment. Table 15 in appendix 2 summarises the fatigue lives of specimens tested after a presoak in saline solution. This data also demonstrates this effect and shows that there is a marked effect on fatigue strength after only 4 hours soak time, and reaches a peak effect by 24 hours. The unpredictability of the severity of the pits is discussed later in the chapter.

The Xh material shows a similar response (figure 23, p.91), with respect to environmental

effects, as the Xe material. The test specimens exposed to saline conditions display a marked reduction in fatigue strength. In the low cycle region, the fatigue strength for the fog tested data shows a stronger fatigue response than the presoaked specimens. This response is reversed in the high cycle region, where the fog tested samples have a weaker fatigue response than the presoaked samples.

The Xe T1 material (figure 24, p.91) displays comparable fatigue strength between fog and air tested samples in the low cycle region with a significant reduction in strength in the high cycle region.

The fog tested data also crosses the presoak data, as with the Xh T4 material. It should also be noted however that the Xe T1 material was tested twice at 350MPa after a 24 hour presoak in salt solution. These data points are plotted and it can be seen that there is some degree of scatter (17000 cycles and 55000 cycles) in this data.

Figure 25 (p.92) shows a dissimilar pattern to the previous data, with the presoaked data exhibiting a greatly reduced fatigue resistance compared with the air tested data at the low cycle end of the curve, but a very similar response in the high cycle region.The effect of environment on the base material was also examined. This gives a baseline for comparison in order to examine the effects of the particulate addition in the matrix materials with respect to environmental factors.

The T4 base material tested in air (figure 26, p.92) displays the strongest response. The rest of the data display very similar, significantly reduced fatigue response. The T4 base material tested in a salt fog atmosphere has a significantly reduced response with respect to the air tested data. This effect is not so marked in the T1 data.

Figure 27 (p.93) shows a summary of the overall effect of the salt fog environment on each of the alloy type. All the material tested in a fog atmosphere display comparable fatigue strength, irrespective of heat treatment, alloy type and processing route. All of the data lie within a narrow band in the graph, and allowing for scatter in the results, it then appears that there is no significant difference in fatigue response in a saline fog atmosphere.

2.5. Frequency Effects.

The effects of various waveform frequencies are shown in figure 28 (p.93). Mechanically alloyed (Xe) T4 material was tested in a saline fog atmosphere at 10Hz, 1Hz and 0.1Hz. These data are well below the fatigue strength of the air tested baseline data. There is a negligible effect of frequency on fatigue life with respect to the number of cycles to failure.

2.6. Effects of R-ratio Variation.

On examination of R-ratio effect, it was noted that an R value of 0.5 in a fog atmosphere generates a higher S-N curve than that of 0.1 under the same conditions (figure 29, p.94). Figure 30 (p.94) shows the effect of R-ratio where stress range is plotted against the number of cycles to failure. As would be expected, the higher the stress range, the lower the fatigue strength of the material.

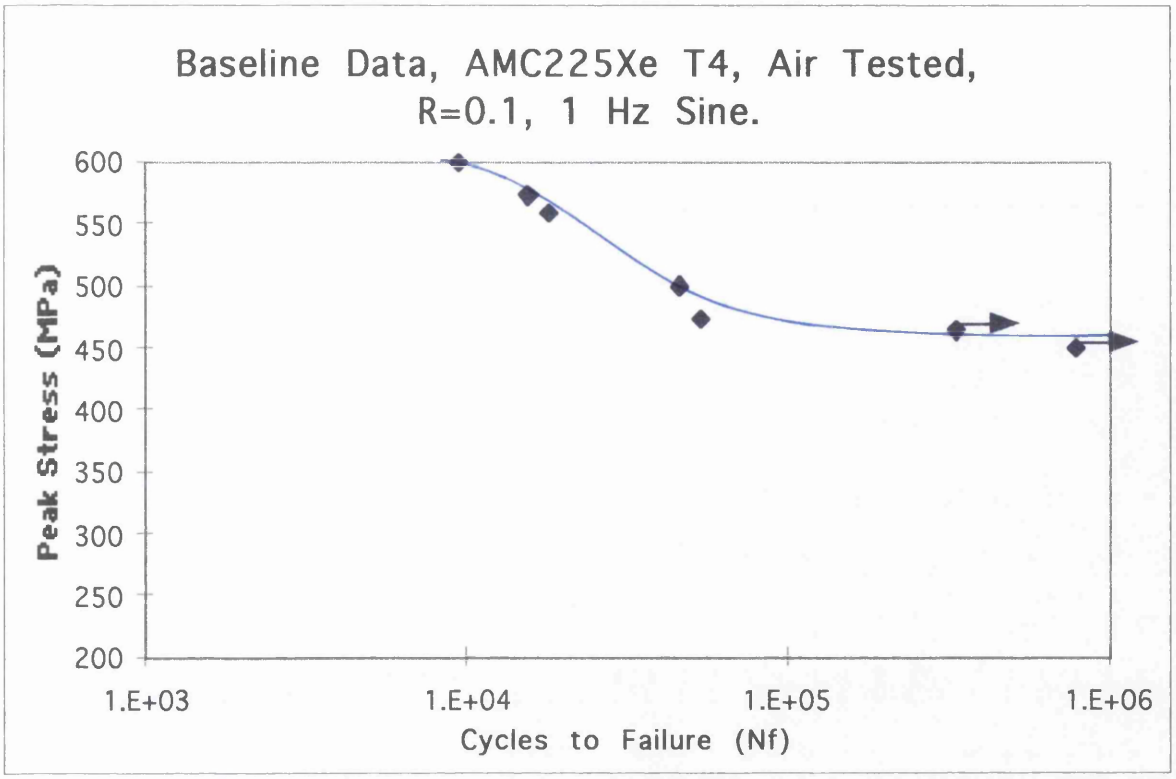

Figure 17.

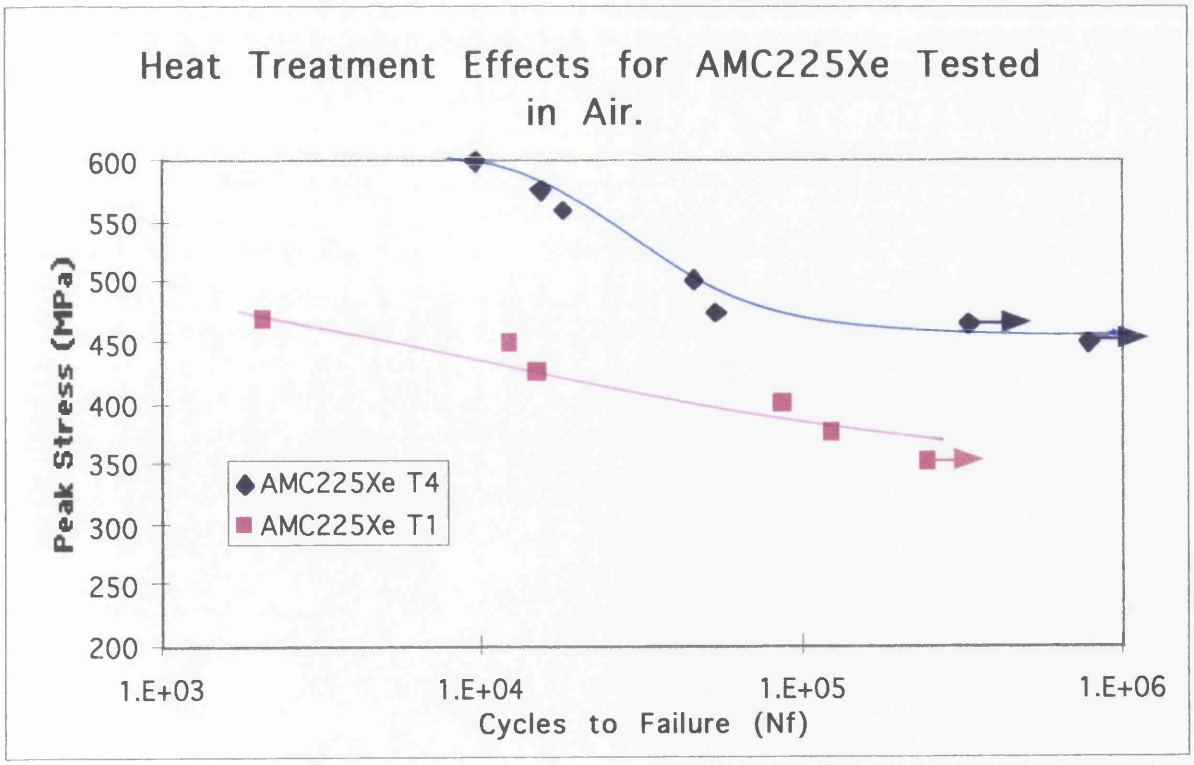

Figure 18.

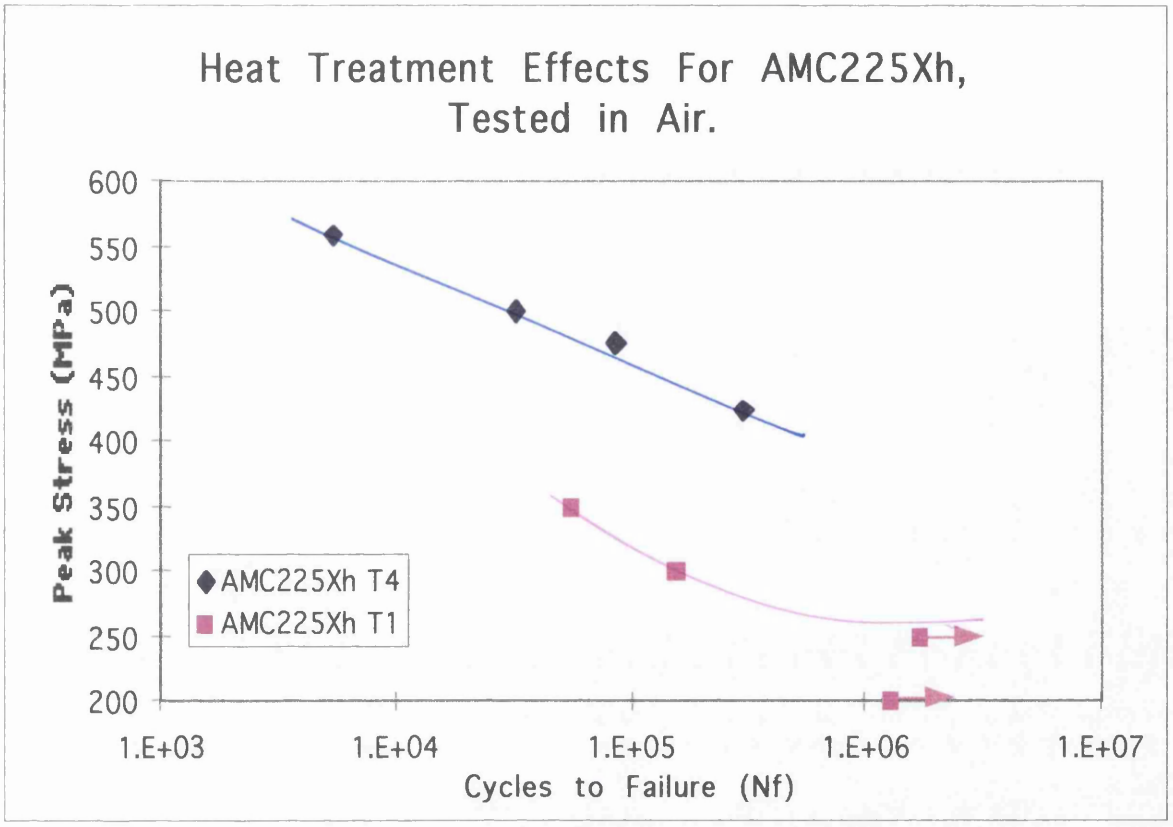

Figure 19.

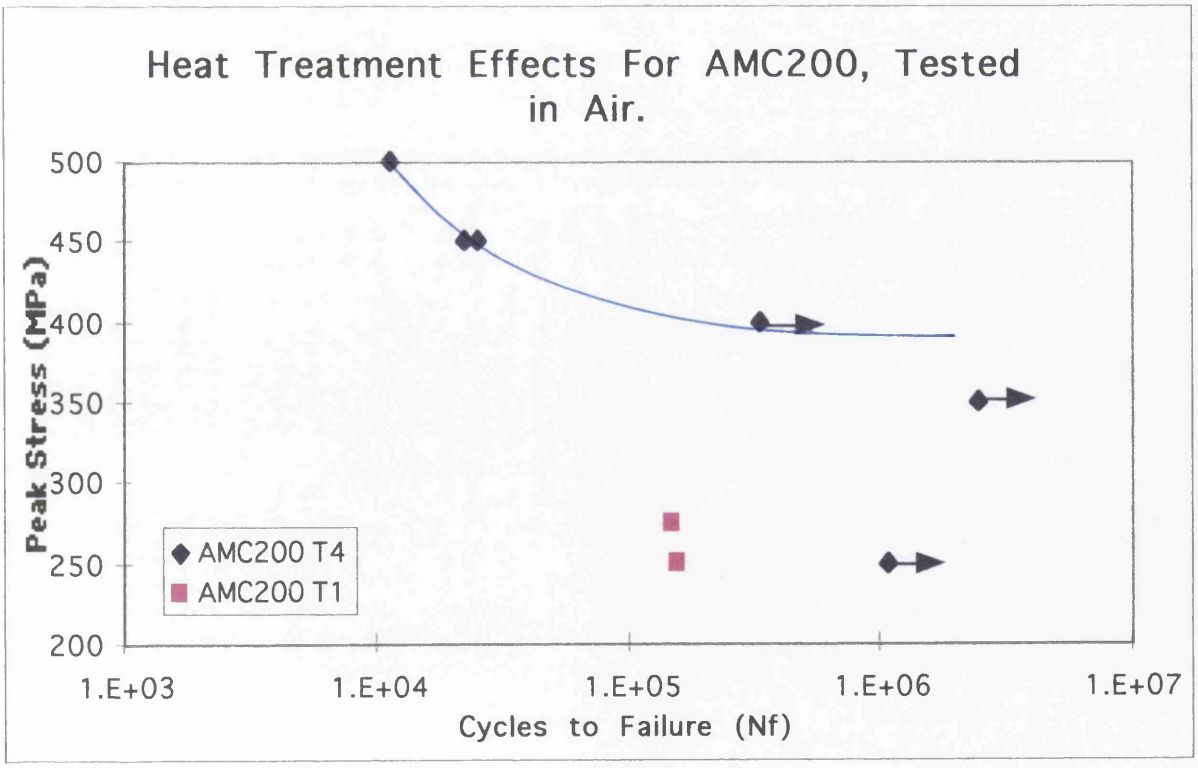

Figure 20

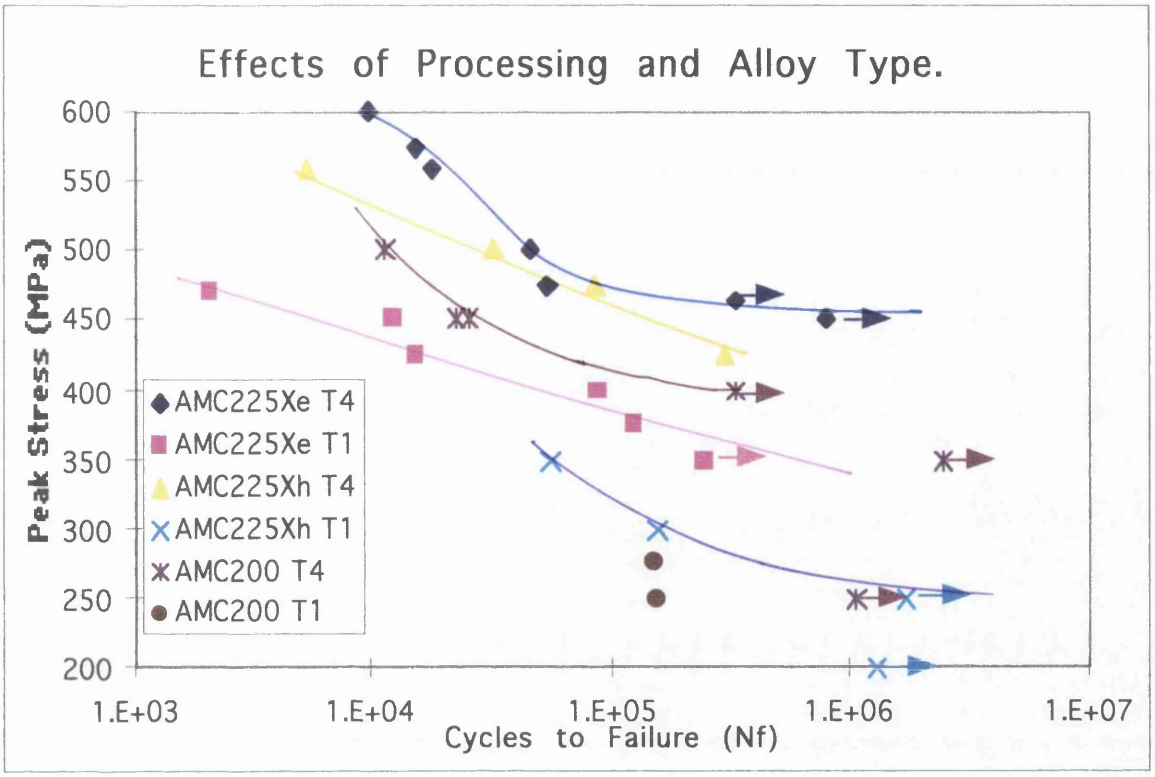

Figure 21.

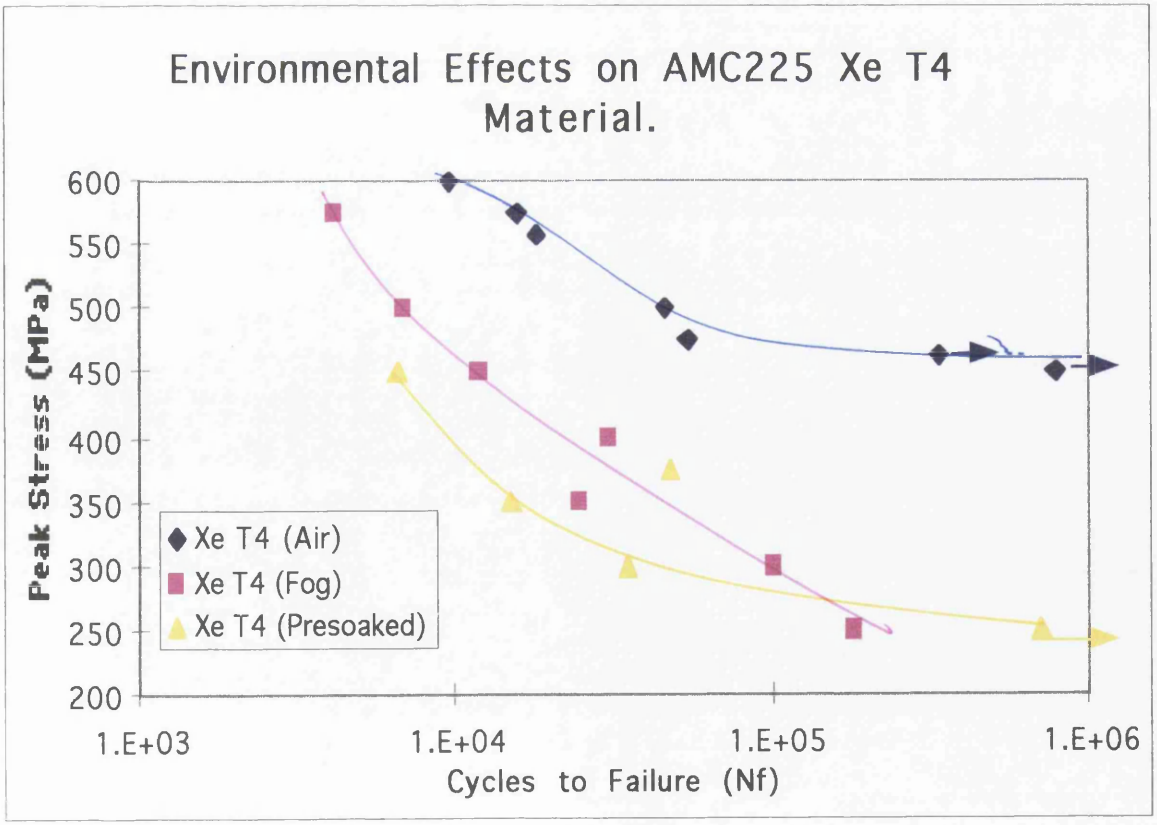

Figure 22.

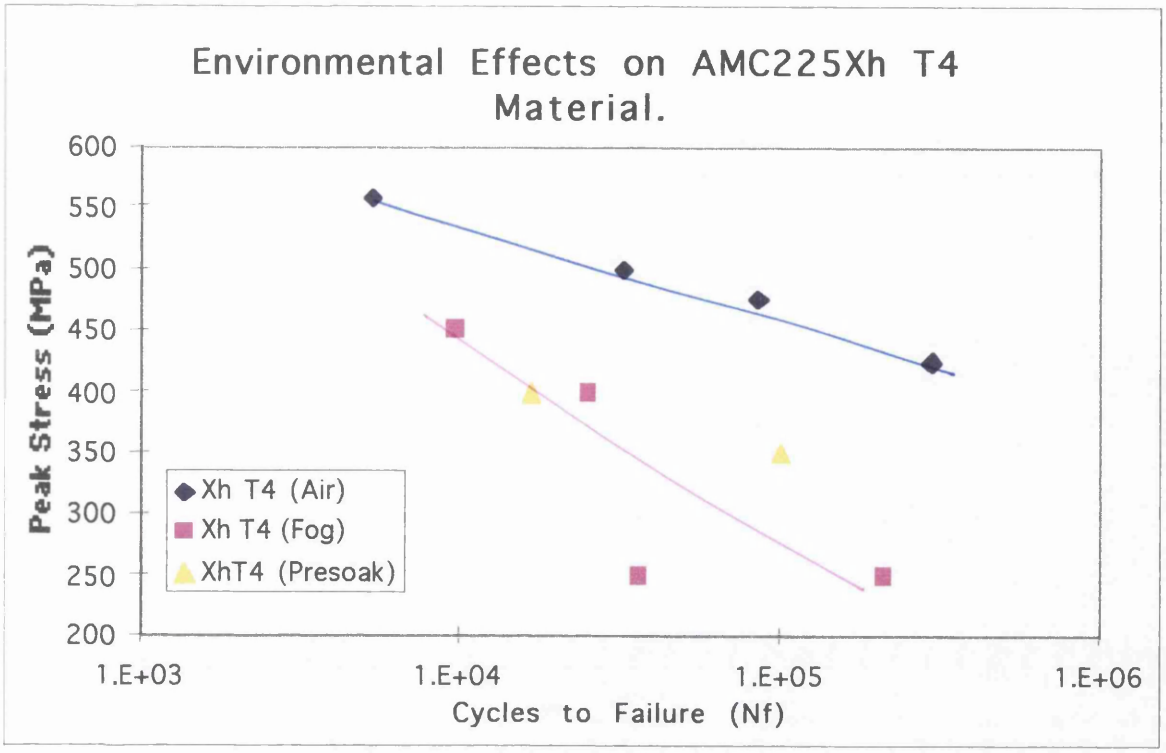

Figure 23.

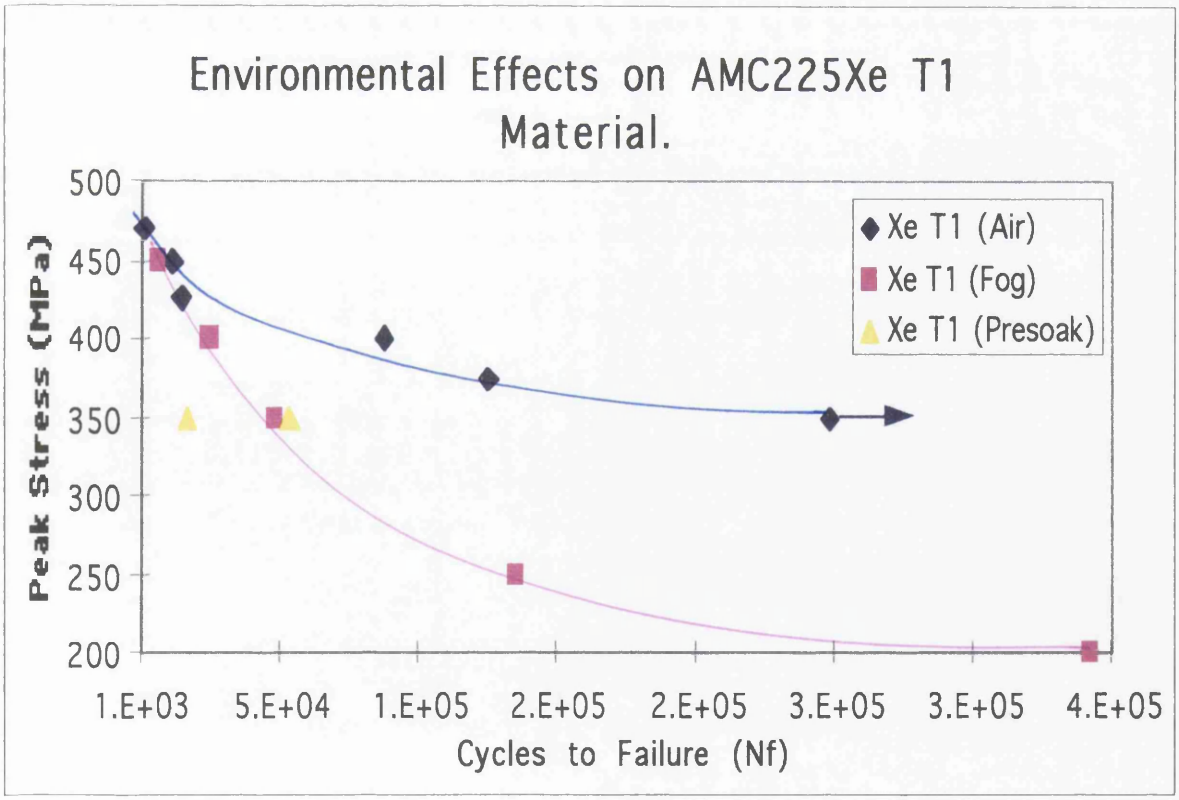

Figure 24.

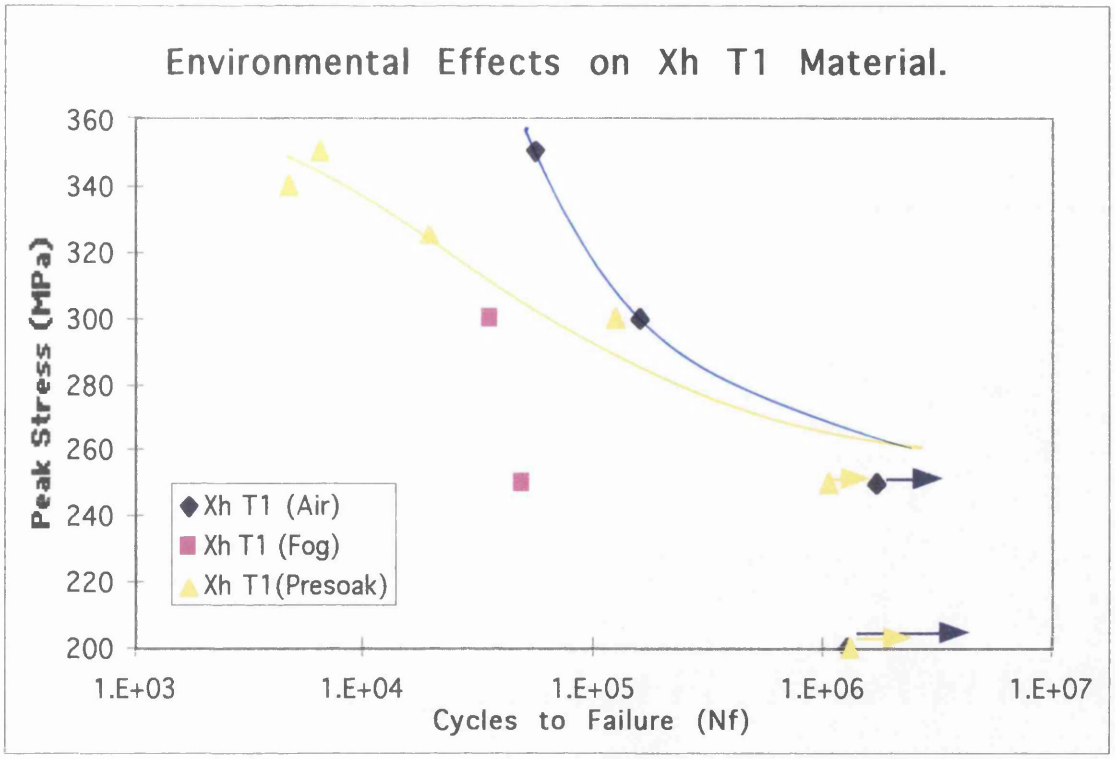

Figure 25.

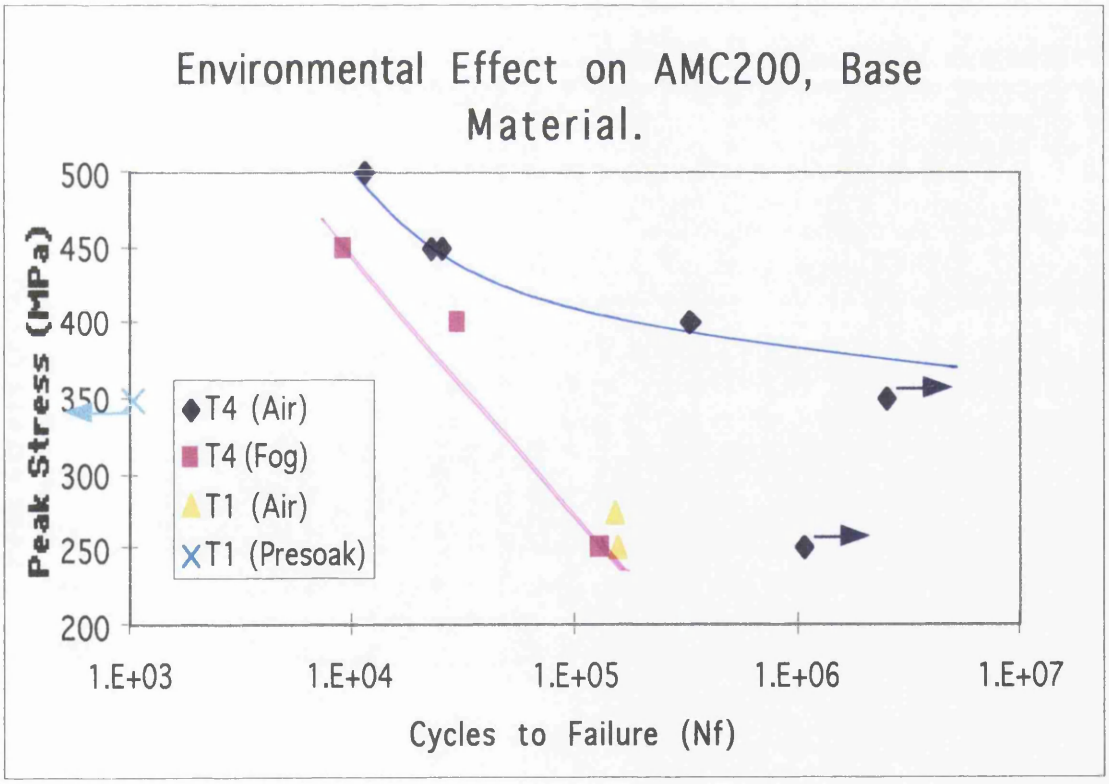

Figure 26.

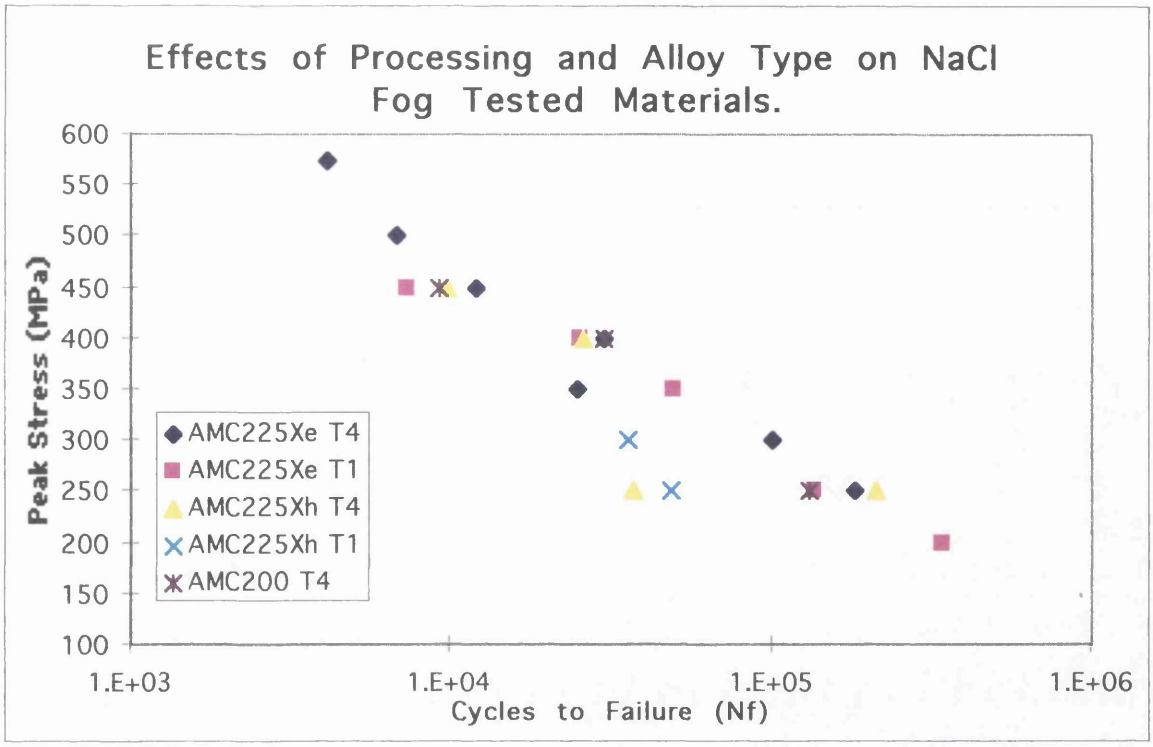

Figure 27.

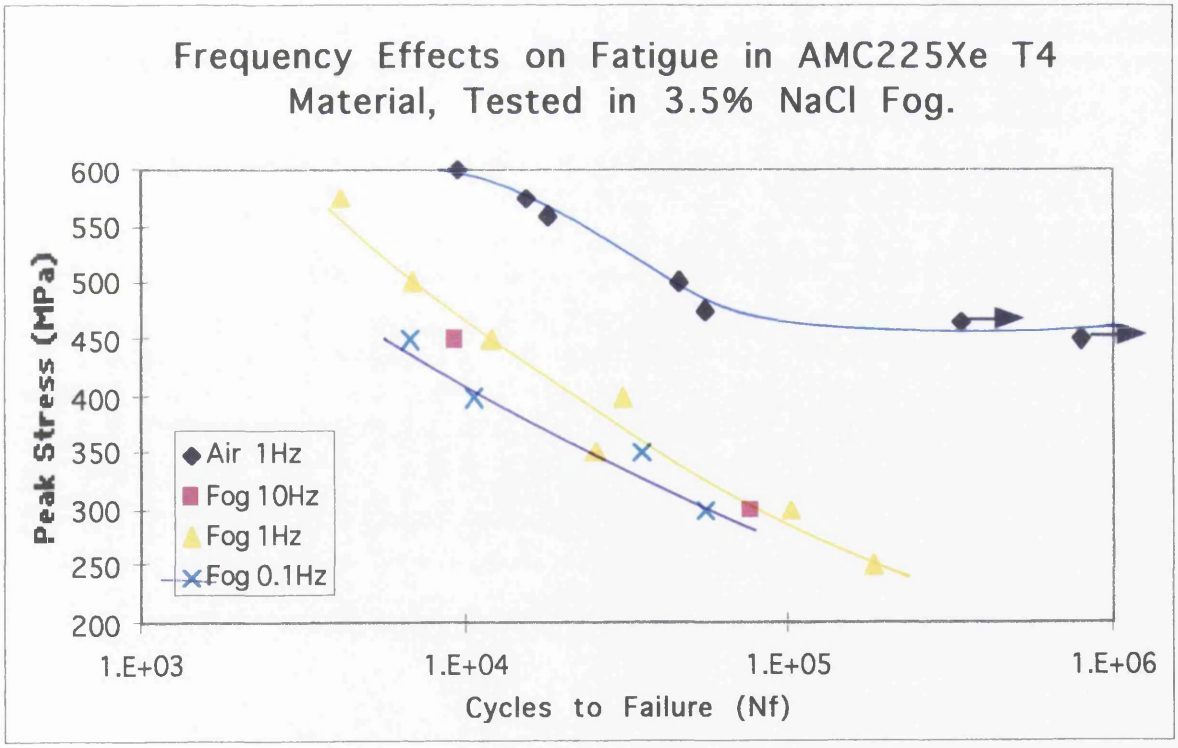

Figure 28.

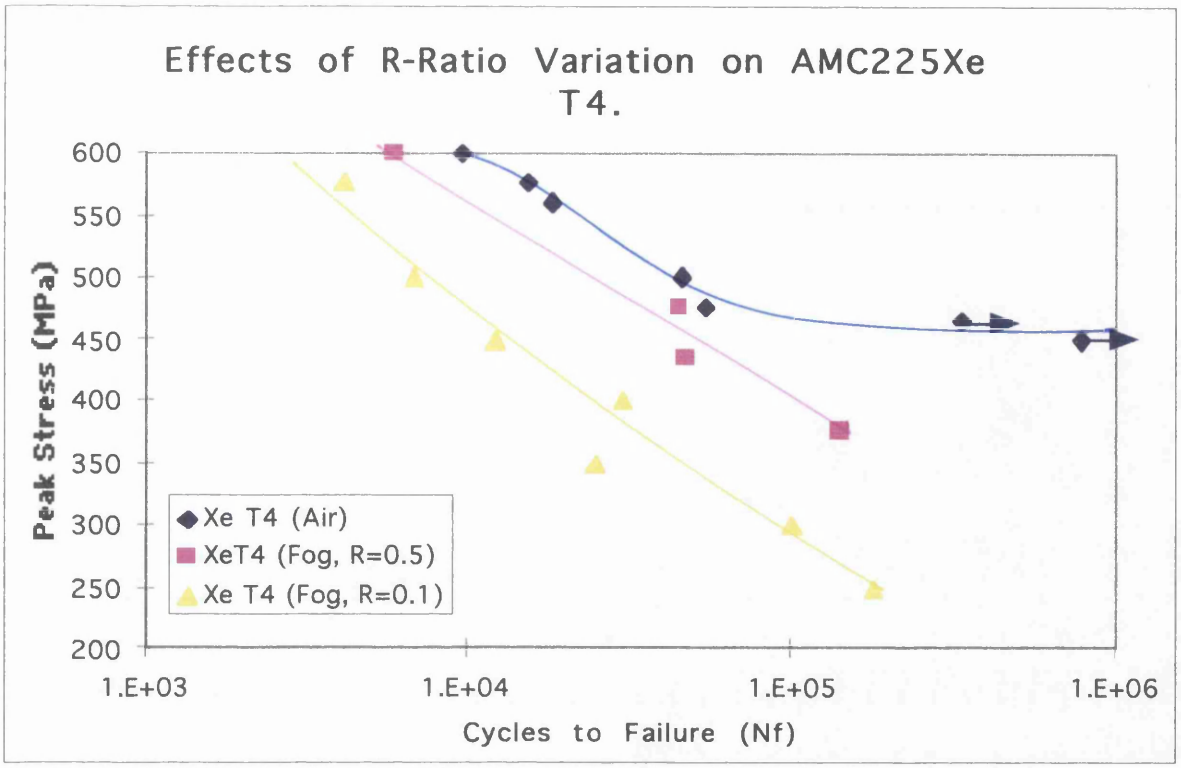

Figure 29.

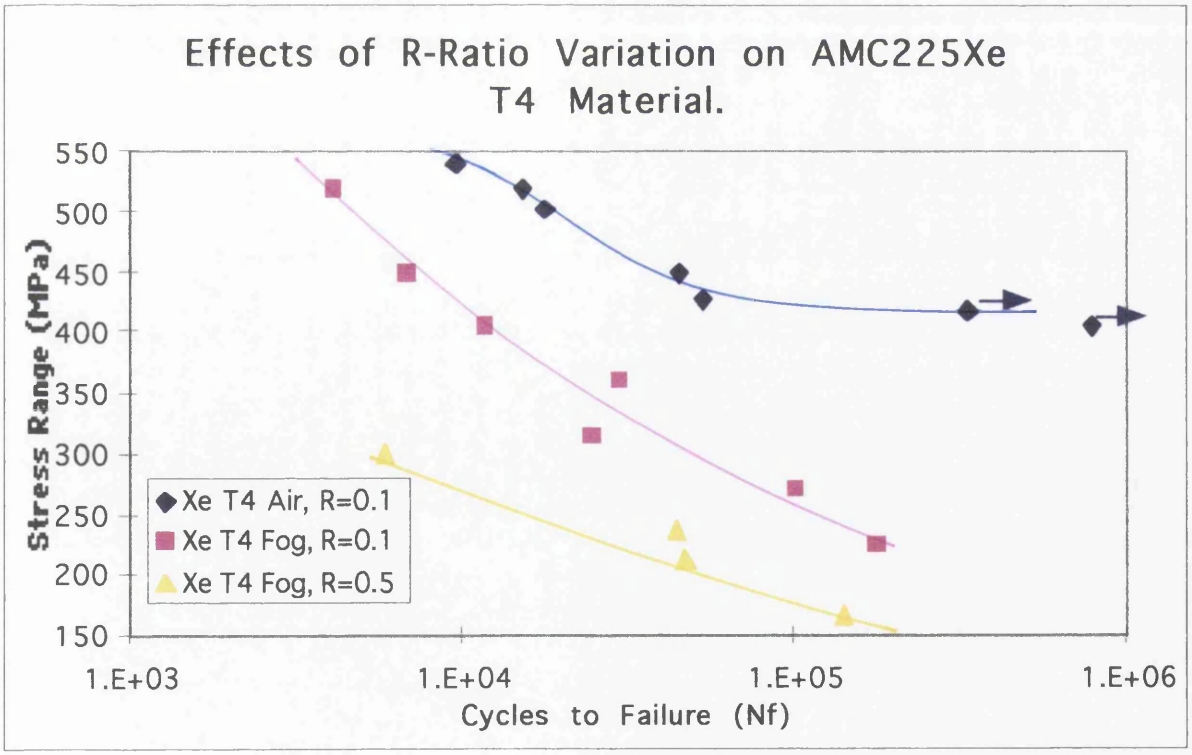

Figure 30.

3. Corrosion Effects.

3.1 Pit Formation with respect to Immersion Time.

Figure 31 shows a histogram of pit depth frequencies in AMC225Xe T4 material, measured after various NaCl solution presoak times. There is a large degree of uncertainty in the prediction of pit depth with respect to soaking times. Longer soaking times produce more pits overall with more deeper pits. It should be noted that deep pits can be observed in as little as 24 hours. At 48 hours, no pits deeper than 20 μm were observed and the greatest frequency of pit depths was found to be 5-10 μm. This histogram was produced from small areas on a number of test pieces and as such can only give an indication of the results expected from a more comprehensive survey.

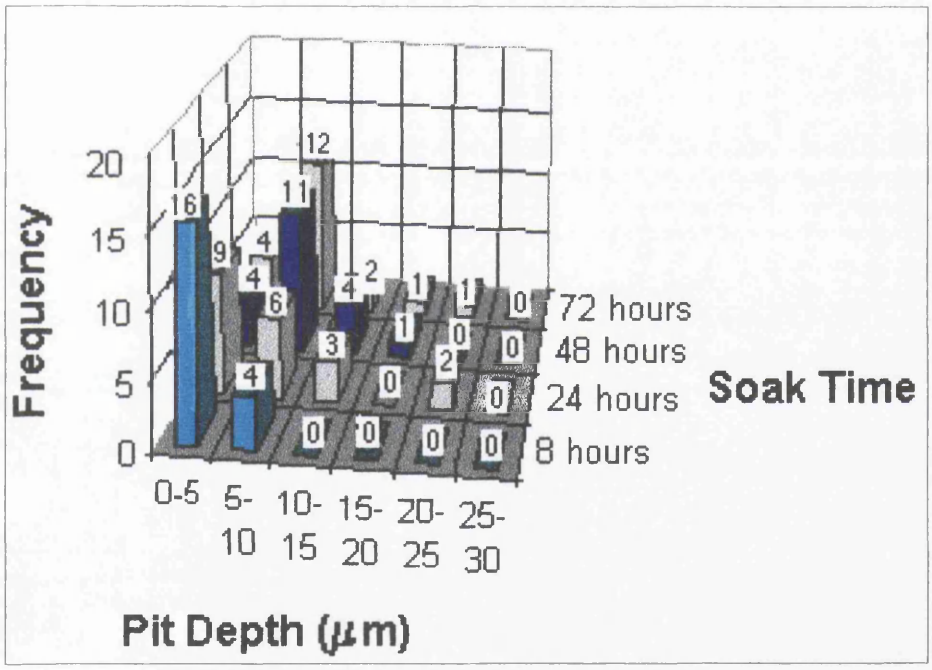

Figure 31.

It should also be noted that the pitting frequency can be influenced by polishing. It was found that polished samples tended to initiate more pits than unpolished samples. This is most likely to be due to the cleaning effect that polishing and subsequent washing has on the sample. Although the unpolished samples were subjected to cleaning with soap and water with a subsequent rinse in ethanol, the process was likely to have been less effective

on the unpolished specimens due to the rough undulating nature of the machined surface. This probably left some lubricating residue on the surface of the specimen which was liable to impart some protection from the saline solution. Also, the thickness of any protective oxide layer would be reduced in the polished samples.

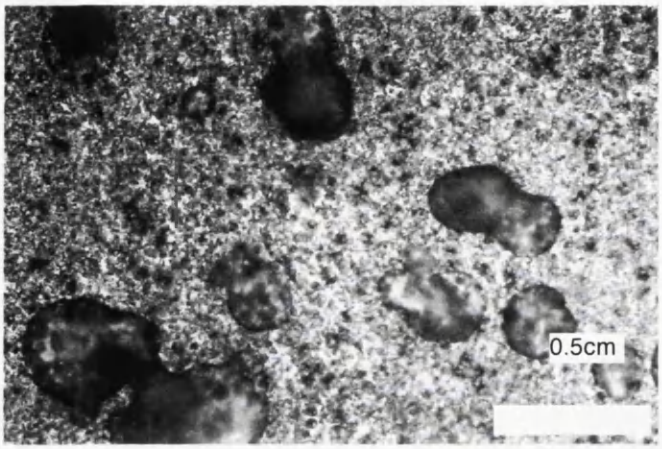

Figure 32. XeT4, 24hr presoak, polished.

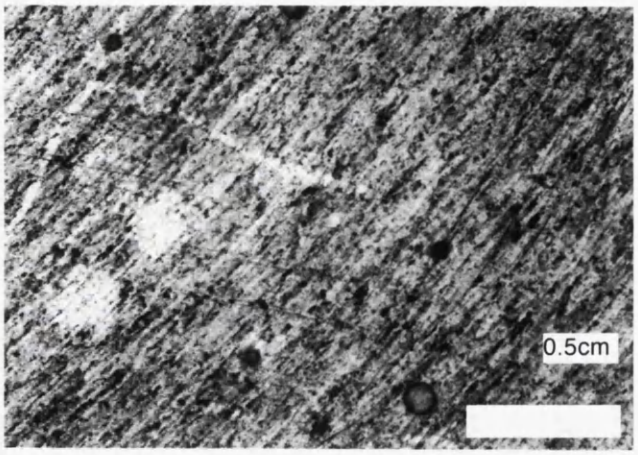

Figure 33. XeT4, 24hr presoak, unpolished.

The figures 32 and 33 show the surface appearance of both polished and unpolished specimens of AMC225Xe T4 material after a 48 hour soak in 3.5% sodium chloride solution. The polished specimen has more apparent initiated pits which exhibit circular pit mouths and a smooth inner surface.

3.2. Pit Morphology.

The shape of a surface pit may also vary. The dunked samples exhibit round pit mouth morphology, whereas the fog tested samples show directional effects. Figures 32 and 33 above show typical dunked response to saline solution of a cross sectional section of material soaked with no stress applied. It was also found however that the sides of these samples exhibited a similar pit mouth profile, in that no directional response was observed. This seems to imply that the directional effect is principally stress induced.

This phenomenon was investigated and the figures 34 and 35 overleaf show the response obtained.

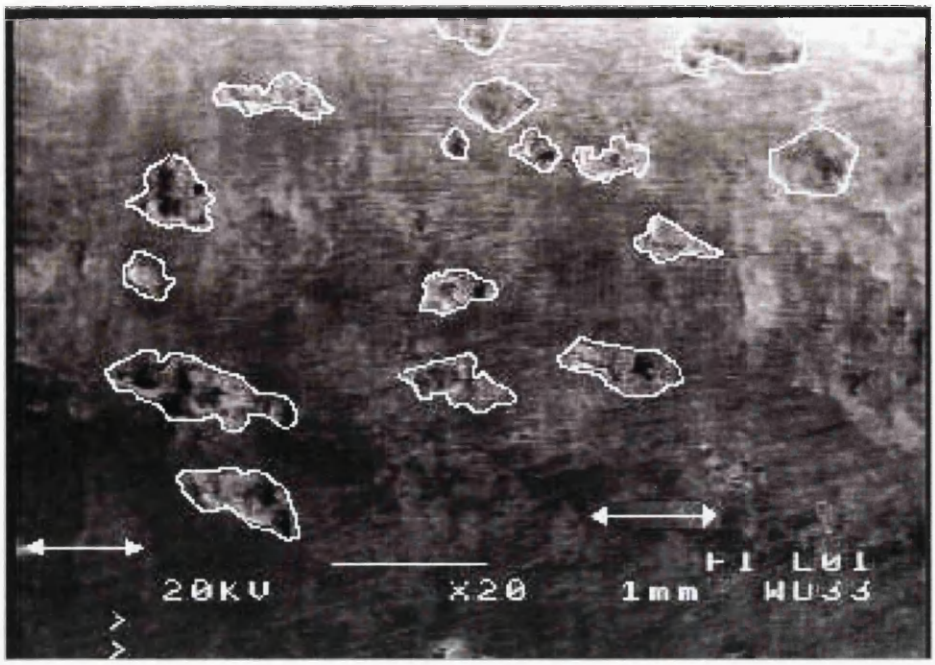

Figure 34.

These figures illustrate a marked response to the extrusion/stress direction.

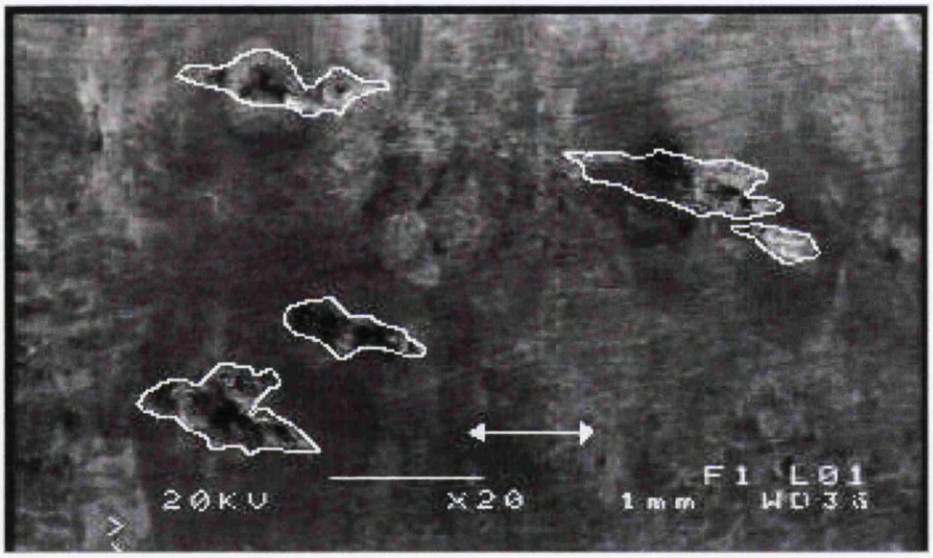

Figure 35.

3.3. Compositional Analysis of Surface Pitting.

Table 4 shows the composition of AMC200 (base alloy) material.

Element	Reading (%)
Magnesium	1.51 (1.2-1.8)
Manganese	0.59 (0.3-0.9)
Copper	3.86 (3.8-4.9)
Aluminium	rem

Table 4.

Element	Reading 1(%)	Reading 2 (%)	Reading 3 (%)	Reading 4 (%)	Reading 5 (%)	Reading 6 (%)	Reading 7 (%)
Carbon	4.37	4.98	5.62	5.44	5.06	4.04	5.32
Oxygen	0.79	0.58	0.72	1.35	1.37	1.18	0.69
Magnesium	0.50	0.24	0.65	0.90	0.96	0.83	0.13
Aluminium	88.87	90.31	89.07	88.43	87.22	88.13	90.09
Silicon	0.46	0.56	0.47	0.45	0.53	0.58	0.52
Manganese	0.84	0.44	0.28	0.51	0.78	0.19	0.35
Copper	4.18	2.89	3.19	2.91	4.08	5.05	2.89

Table 5.

Table 5 above shows typical readings from base material at a pit initiation site after soaking in a saline solution for 24 hours. It is apparent that the magnesium content of the material is significantly reduced in the initiation region, although the other alloying elements appear to be within the tolerance limits for this material.

4. Crack Propagation.

The measurements of fatigue crack growth rates were made for each of the six alloy variants, both in laboratory air and in 3.5% NaCl fog environments. The data presented here are in the form of da/dN vs. ΔK graphs.

Material Type	Air tested (MPa)	Fog tested (MPa)
XeT4	250	200
XeT1	250	200
XhT4	250	200
XhT1	250	200
200T4	175	175
200T1	175	200

Table 6.

Table 6 summarises the peak stress under which each material was fatigued.

Figure 36 (p.99) shows associated crack length (a in mm) vs. number of cycles (N) tested at a strain rate of 1mm/minute for each of the samples tested.

A potential drop method was used, as described in the experimental section. As expected, crack length increases with the number of cycles at a progressively faster rate. Since the peak test stress was not the same in all cases (table 6) the crack growth rates are not directly comparable from this graph.

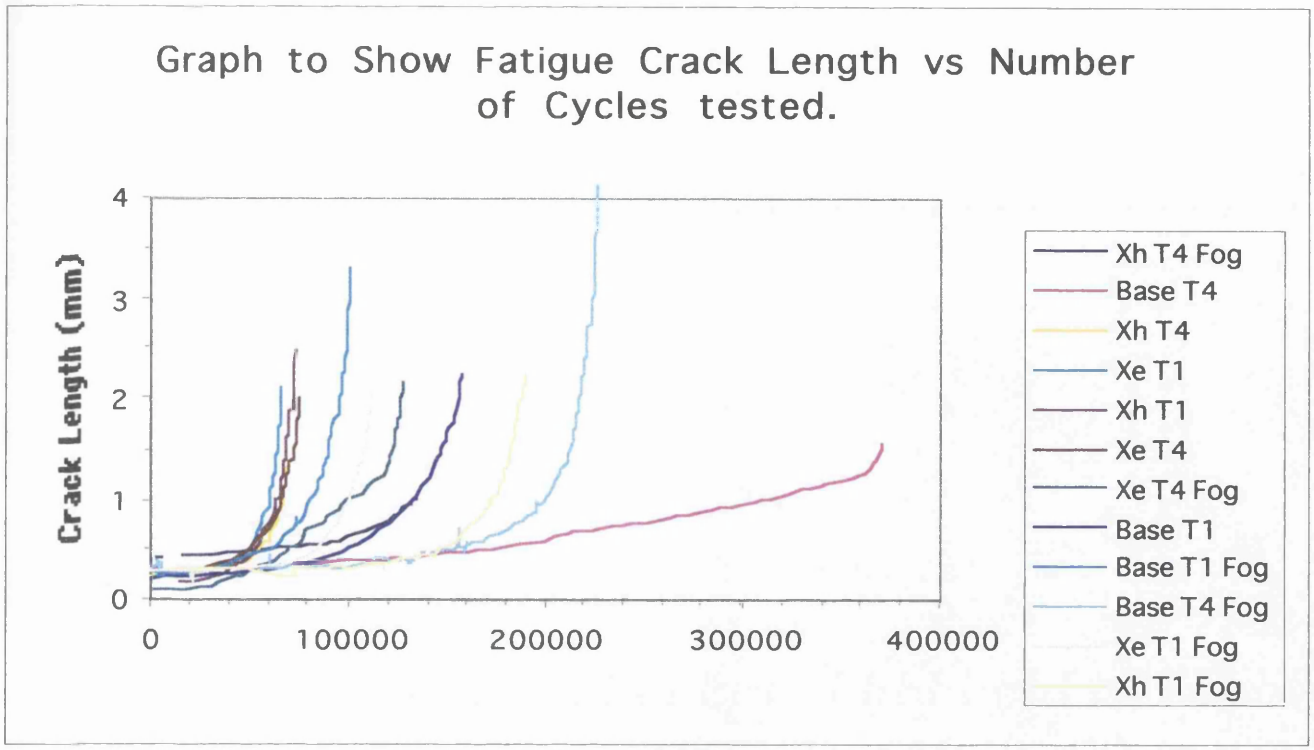

Figure 36.

The baseline data (AMC225Xe T4 material) tested in air and salt fog conditions are presented in figure 37 (p. 100). It can be seen that the data correlate very well above ΔK values of 8, which corresponds to the Paris regime and effectively describes the performance of microstructurally "long cracks". Below this value however, there is apparent divergence of the data. The fog tested samples exhibit a slightly faster rate of crack growth in this "short crack" growth regime. This effect is not observed in the Xh and base materials (figures 38 and 39).

Figure 38 (p. 100) demonstrates good correlation between the data sets throughout the ΔK range, with a small amount of divergence in the microstructurally short crack growth region, similar to the Xe material, although to a markedly lesser degree.

The scatter observed in the the fog tested T4 base material data (figure 39, p.101), is due to true microstructurally "short crack growth" effects probably in the threshold region. In a similar way to the composite materials, the data correlates very well above ΔK values of 8. The T4 air tested material appears to have a markedly slower rate of crack growth in the range of ΔK between 5-8. This advantage appears to be lost in the saline environment.

Crack Propagation Behaviour for AMC225 Xe Material Tested in Air and NaCl Fog.

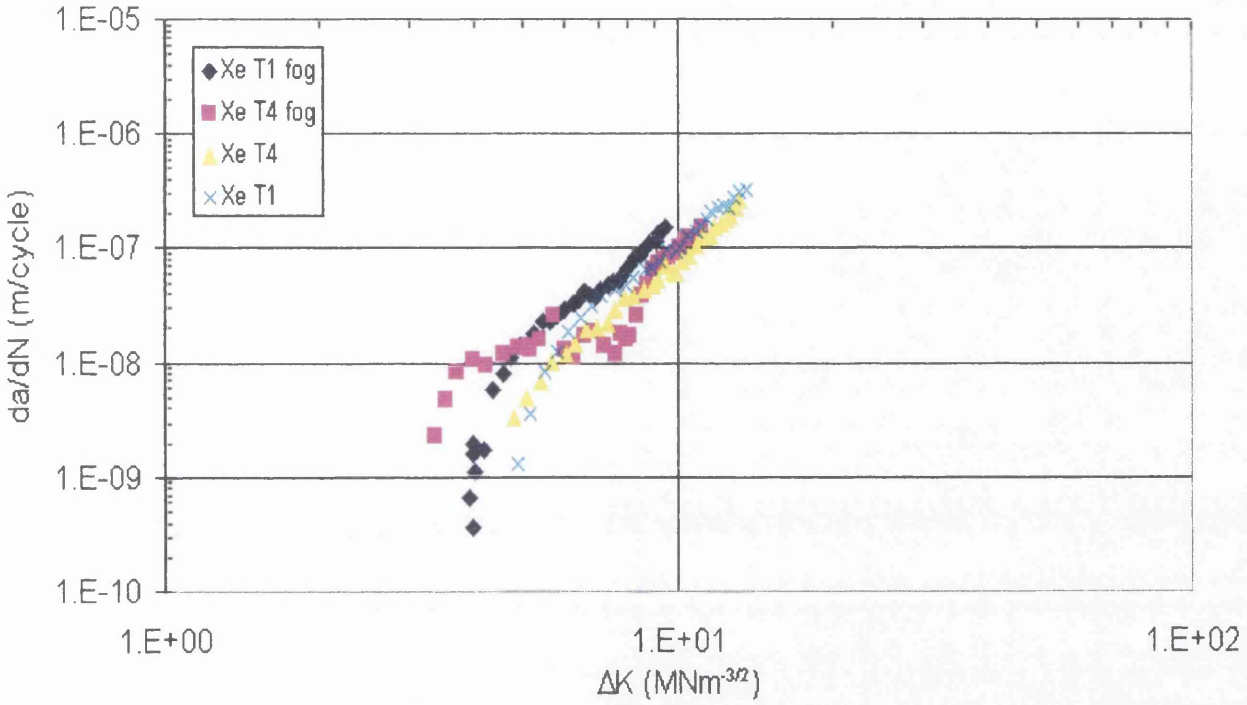

Figure 37.

Crack Growth Behaviour of AMC225 Xh Material Tested in Air and NaCl Fog.

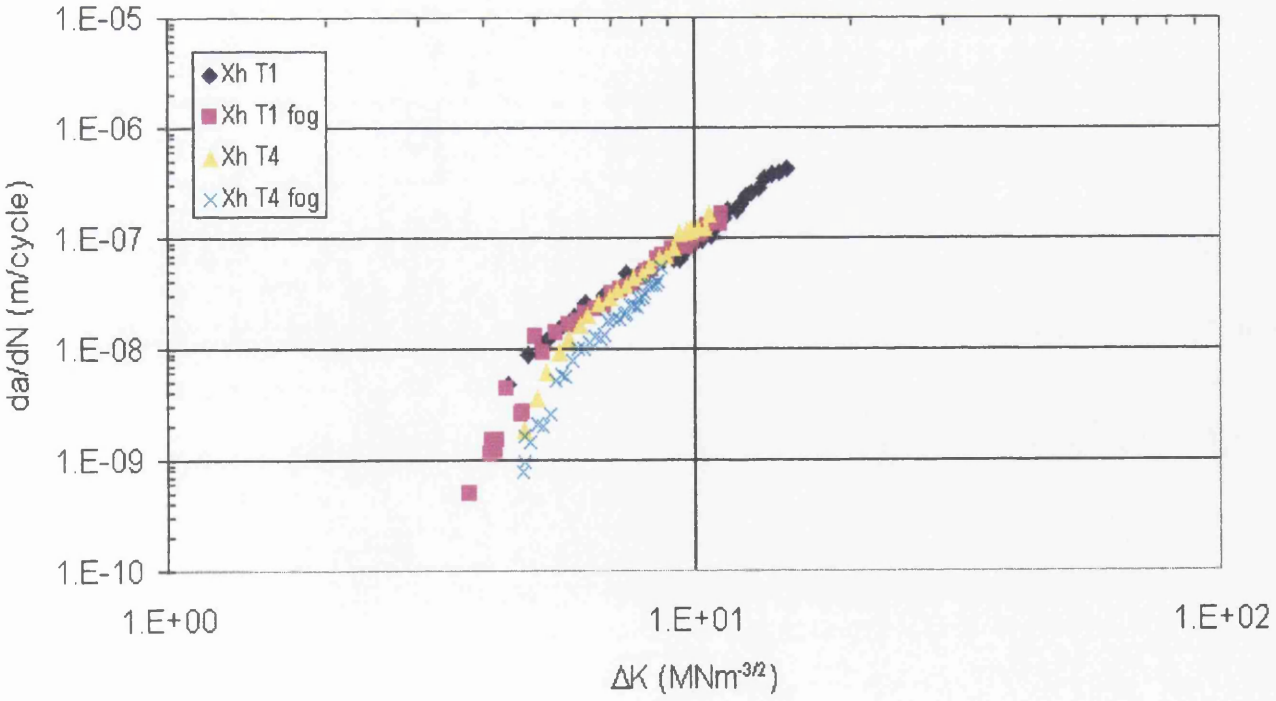

Figure 38.

Crack Propagation Behaviour for Base Material in Air and NaCl Fog.

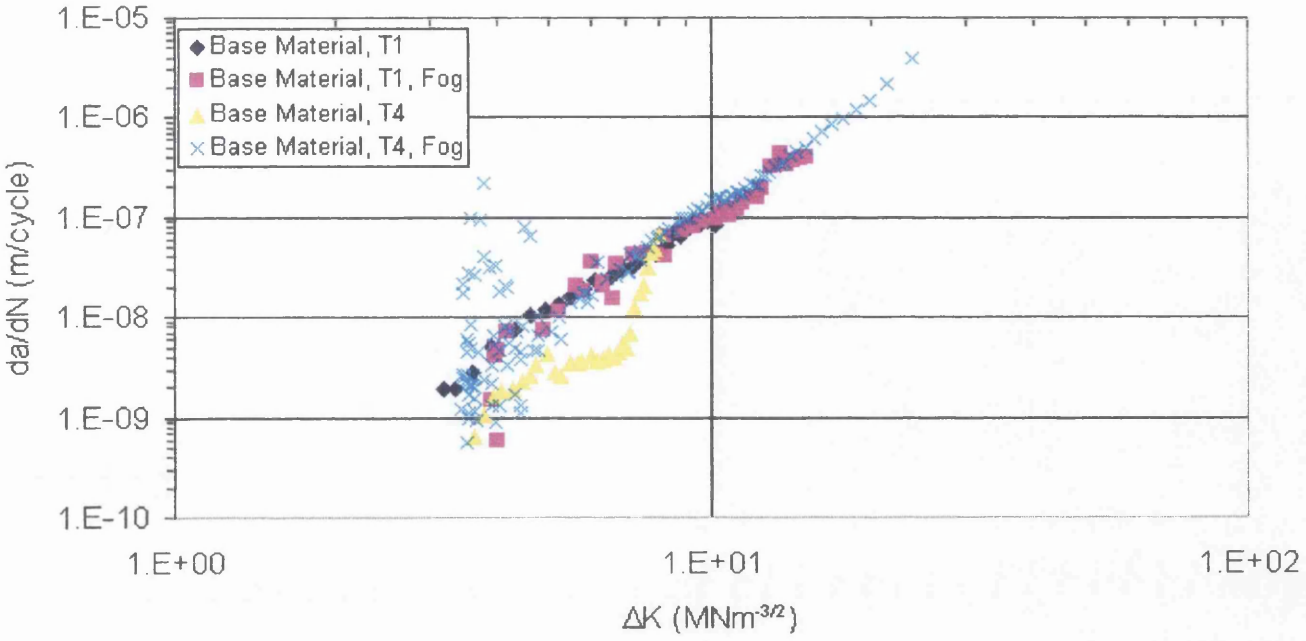

Figure 39.

UNIVERSITY OF WALES SWANSEA LIBRARY

5. Fractography.

Results of fractographic analysis of fatigued samples and 3.5% NaCl solution soaked samples are shown in the discussion and in appendix 3 for ease of reference.

Figure 40 below shows a typical pit from which a fatigue crack initiated. Figure 41 shows this pit in more detail.

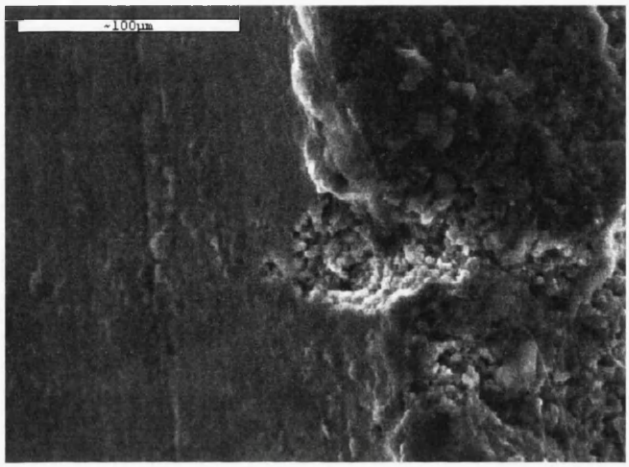

Figure 40.

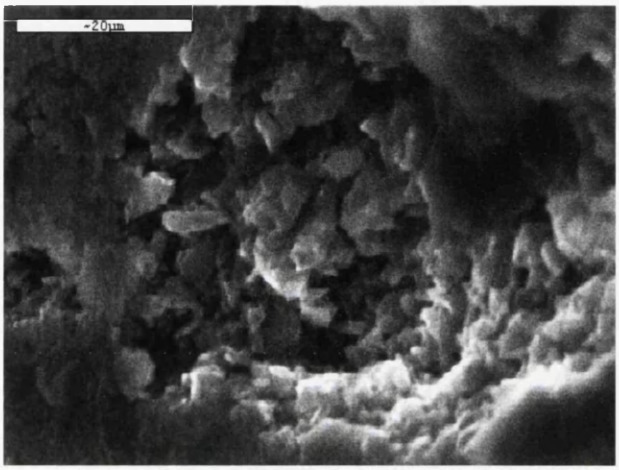

Figure 41.

Figure 42 shows the area just behind the crack initiation site of a 24 hour salt solution presoaked Xh T1 sample, tested at a peak stress of 300MPa. The flat appearance of the fracture surface suggests a transgranular fracture mode, indicating corrosion fatigue failure. This may be due to some residual moisture in the base of the initiation pit.

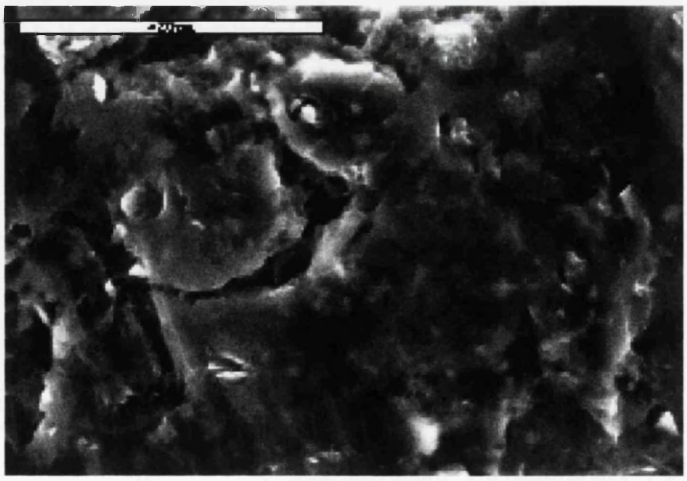

Figure 42.

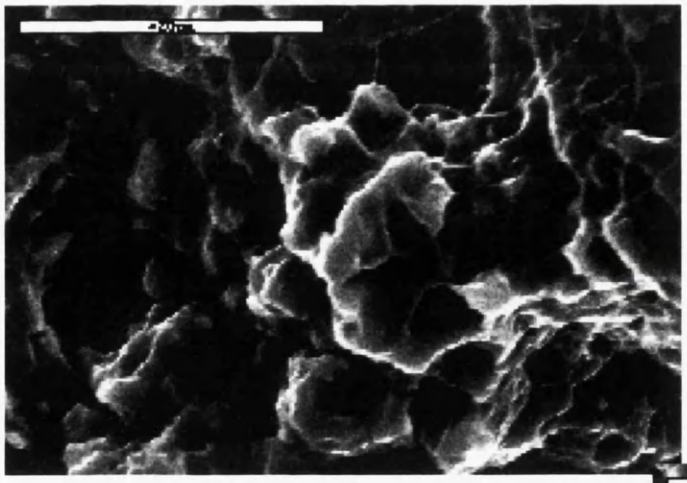

Figure 43.

Figure 43 shows the area approximately 50 microns from the point shown in figure 40 above, in crack propagation direction. Here, the dimples formed during fatigue cycling are large, indicating slow rupture or tearing. The features appear rounded due to corrosion product on the surface.

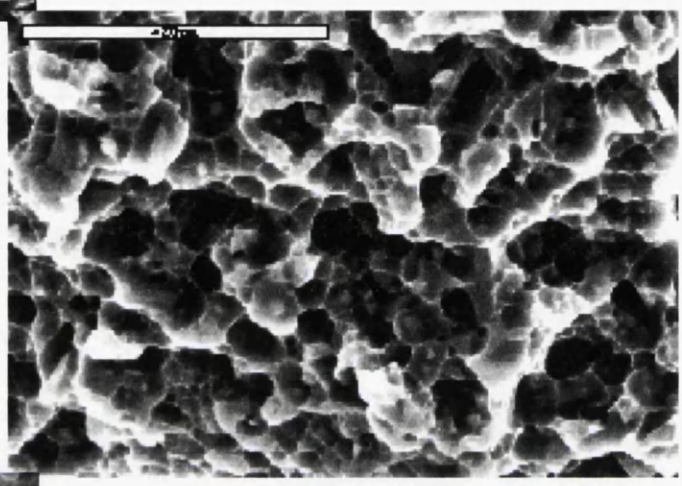

Figure 44.

Figure 44 depicts the stepped region of fatigue fracture surface. Here SiC particles can be seen in the bottom of the dimples which are smaller than in figure 43, indicating more rapid crack growth.

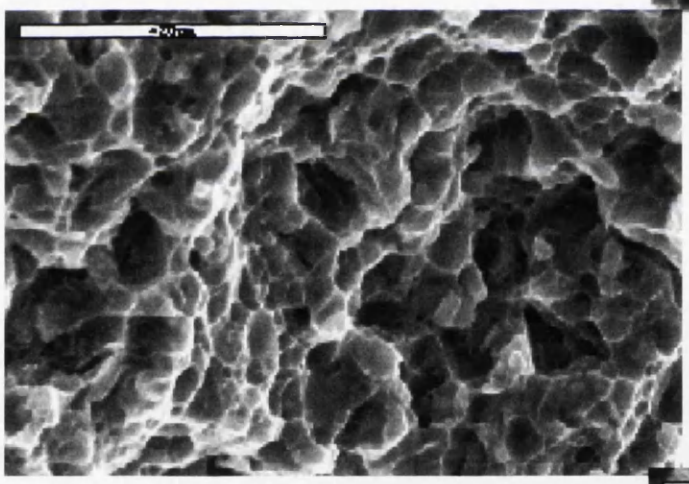

Figure 45.

The fast crack growth region of a fatigue fracture surface is shown in figure 45. Here there is a mixture of very small and slightly larger dimples. The overload region (figure 46) exhibits very small dimples. This typical pattern of fatigue crack progression, where dimple size decreases as crack growth rate increases in the direction of crack growth, was evident on all the samples examined during the course of this study.

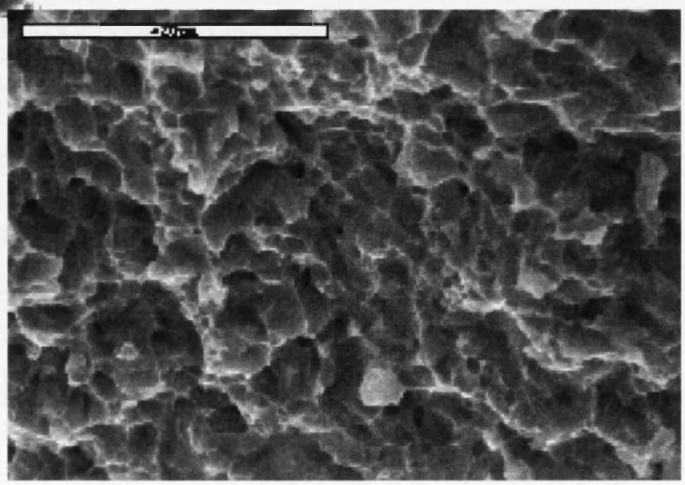

Figure 46.

Part 5. Discussion.

1. Mechanical Testing.

From table 7, AMC225Xe T4 material has the highest yield stress, ultimate tensile strength and elastic modulus and all have higher values for yield stress and U.T.S. than the T1 materials. The elastic moduli of the T4 materials appear to be more dependent on the type of material than the heat treatment. The Xe material exhibits the greatest value for Young's modulus, Xh material a slightly lower value, and the base material exhibits much lower values than either of the composite materials.

Material	E (GPa)	UTS (MPa)	Y.S. (MPa)	strain to failure
200a-T1	78	290	142	2.00
200a-T4	74	570	405	2.00
Xe-T1	119	500	220	0.43
Xe-T4	160	700	470	0.04
Xh-T1	12 2	400	140	0.69
Xh-T4	119	640	360	0.23

Table 7.

The extremely high value for Young's modulus of the Xe-T4 material (160 GPa) is probably a result of experimental error as it appears to have no correlation to either the Xe-T1 value or the Xh-T4 value. It should also be noted that the typical modulus expected from this materiall is 115 GPa, with the base material expected to be in the region of 70 GPa according to AMC official figures.

The composite materials exhibiting high values of Young's modulus is not unexpected with consideration of the rule of mixtures, which states that:

Assuming, $\varepsilon_p=\varepsilon_m=\varepsilon_{cl}$, where, ε=strain,
p = particulate,
m = matrix,
cl = composite.

then, $\sigma_{cl} = v_p.\sigma_p+(1- v_p).\sigma_m$ σ =stress

v_p=volume fraction of particulate.

Since $\sigma_m = E_m \varepsilon_m$ where E = Young's modulus

and $\sigma_p = E_p \varepsilon_p$

then $E_{cl} = v_p E_p + (1 - v_p) E_m$,

Since the Young's modulus of silicon carbide is much greater than that of the matrix material, then

$$E_{cl} \Rightarrow v_p E_p$$

Hence the higher values of Young's modulus in the composite materials. This also indicates that the composite materials should exhibit similar values for young's modulus, supporting the assumption that this value is a result of experimental error.

In the case of the base material and the Xh material, the Young's modulus value is slightly lower for the T4 heat treated material than for the T1 counterpart.

The U.T.S. and yield strength of the material is thought to give a comparative indication of fatigue strength. This is also evident with the present alloys. The relevant data is illustrated in figure 21 (p.90) It is clear that the fatigue strength is higher for the T4 heat treated alloys, irrespective of the alloy variant, and that the Xe processed MMC is superior to the Xh variant.

It is interesting that the T1 and T4 heat treatments in both the Xe and Xh MMCs produced comparable yield strengths to those of the base material. Yield behaviour presumably occurs when dislocations start to move in the metal matrix material. The ultimate tensile strengths however, are noticeably larger than the base alloy. This is indicative of a steeper stress/strain graph caused by a higher level of strain hardening. The strain hardening is caused by dislocations interacting with the silicon carbide particles. In contrast, the failure strain is much lower in the MMCs. This is because the carbide particles act as preferential sites for the formation of ductile voids. Failure mechanisms are therefore enhanced in the MMCs.

2. Corrosion Effects.

2.1 Pit Characterisation.

The key factor in controlling the impact of salt solution or salt fog on fatigue lives is the development of pits. The pits act as a focal point for the subsequent propagation of cracks. Figure 31 (pg. 95) indicates that short soaking times tend to produce many shallow pits. Longer soaking times produce more pits overall with many deep pits and fewer shallow pits. It should be noted however that deep pits can be observed in as little as 24 hours. None of the pits observed in this survey exceeded 25 microns in depth. This is due in part, to the method of measurement used. Since the measurements were attained using a microscope calibrated to determine the distance between focussing on the base of the pit and the corroded surface, it was intrinsically essential that the base of the pit was visible. It is also true that the build up of corrosion product at the pit mouth stifles the transport of the active species into the pit, preventing further corrosion.

Due to the unpredictable nature of the pitting process as well as the difficulties in measuring pit depths, (mainly due to the build-up of corrosion product at the pit mouth over time), it is only possible to give a general overview of the pitting initiation frequency and depth with respect to soaking time. That is, as soaking time increases, so does the frequency of initiated pits and the depth of the pits. As time continues however, the initiation frequency continues to increase, but the pits depth tends to reach a maximum. This maximum depth is defined by the amount of corrosion product which builds up at the mouth of the pit as this stifles the chemical reactions which produce it. Hence the pit depth may also be related to the temperature, the motion of the solution (ie. stirring in solution or spray rate and direction in humid/foggy atmospheres) or any other variable which may effect the reaction rate.

In addition to the morphology observations, it was noted that pitting frequency was effected by polishing. From figures 32 and 33 (pg. 96), it is clear that the polished sample has many more apparent initiated pits than the unpolished sample. It is difficult to identify pits from the photographs of unpolished samples and this, in part, may account for the apparent lack of

pits on the unpolished specimen. This may also have been a consequence of the cleaning action of the polishing process and subsequent washing, causing disruption of the protective oxide layer.

The shape of the pits is also relevant to this form of measurement. The samples used in this case produced pits with a round hole on the surface and appeared to form a roughly hemispherical pit with a smooth interior (figure 32, p. 96 is a typical example), which is indicative of a rapid corrosion rate (Trzaskoma ref.126). This was not the case in most instances on the fatigued specimens tested in a fog atmosphere, which tended to produce far more irregular morphologies. This suggests that the pit morphologies are influenced by the microstructure/texture of the materials.

Figures 34 and 35 (p. 97) and figure 47 show the surface of AMC225Xe T4 heat treated sample after a 96 hour exposure to 3.5% NaCl fog atmosphere with no stress applied. The pits are very large, of the order of 0.5 mm on the surface with deep, narrow pits intruding into the sample from these initiation sites. The extrusion direction is indicated with arrows.

These samples demonstrate a marked preference for corrosive attack in the extrusion direction, indicating that this is a textural phenomenon since there was no stress applied during exposure to the saline environment.

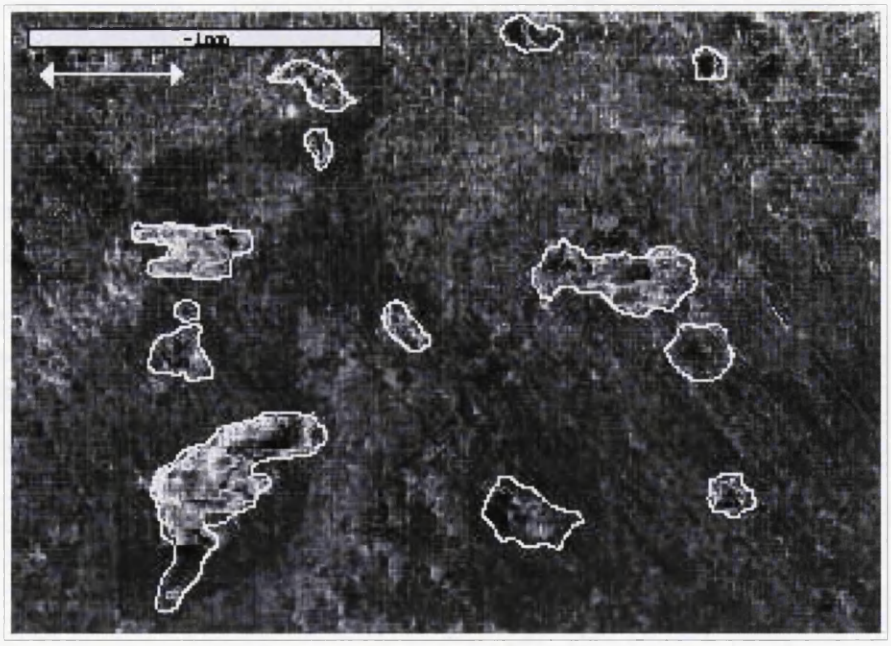

Figure 47.

Figures 48 and 49 are AMC225Xe T4 heat treated material after a 24 hour exposure to a 3.5% NaCl fog atmosphere whilst subject to a static load of 450MPa. It can be seen from these photographs that the pitting occurring here is not only less advanced than the 96 hour exposure, but also is less directionally oriented to the stress and extrusion direction. This could be due to a slight initial preference for corrosive attack to be oriented in the machining direction.

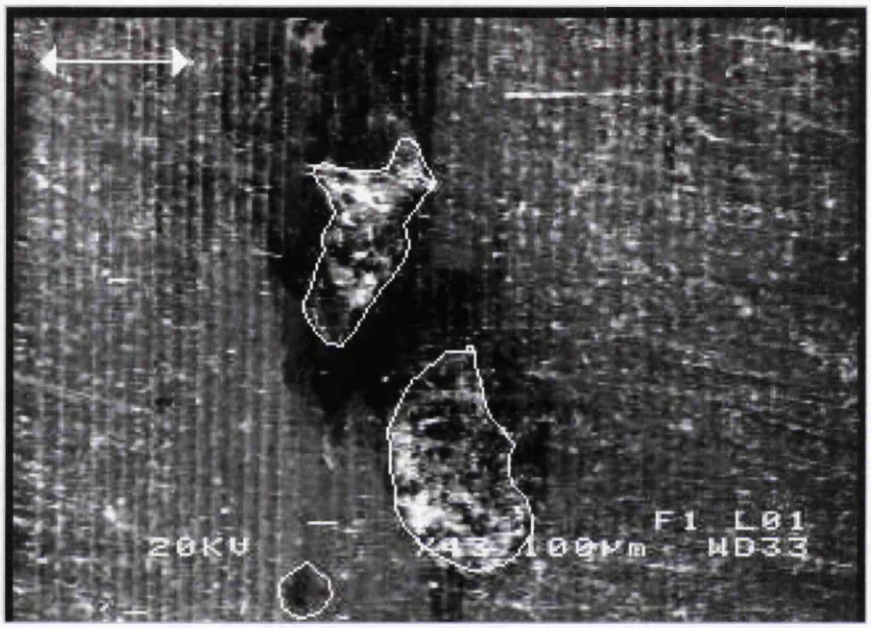

Figure 48.

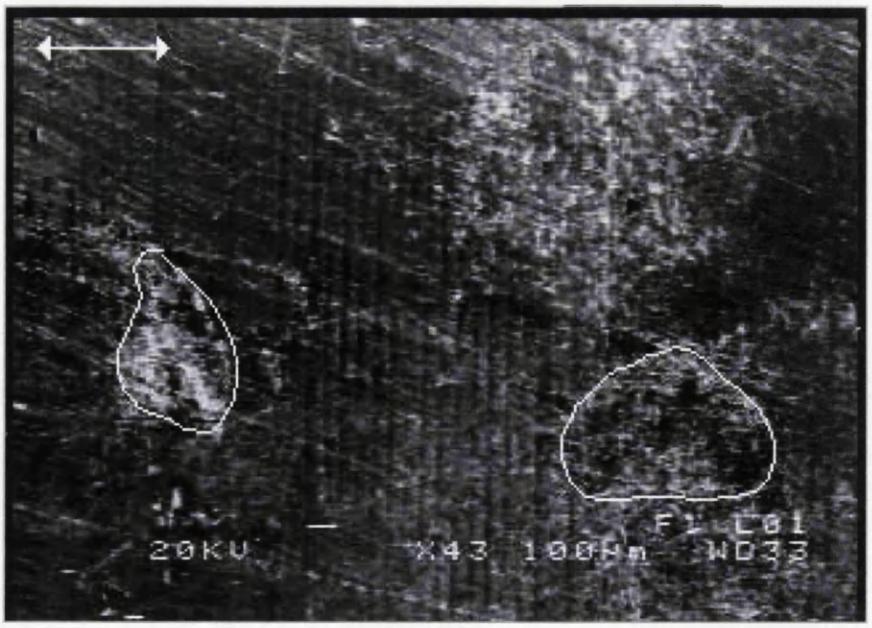

Figure 49.

It should also be noted that corrosion was only apparent on this sample on one side, the side facing the spray nozzle in the fog chamber. Samples which which were exposed to the salt fog atmosphere for longer periods however, showed no apparent preferential corrosion on the nozzle facing side. This may mean that the spray side of the samples begins to corrode slightly earlier, but is unlikely to determine the side on which a fatigue crack may arise due to the nominal difference at longer exposure times and the unpredictability of the pitting process.

The fact that the fatigue response of the base alloy and the MMCs is similar in both pre-exposed and salt fog conditions, suggests that pit formation is confined to the matrix regions of the alloys. This was confirmed by metallographic sections and through EDAX measurements on the electron microscope. These indicated compositional variations within the matrix.

2.2 Metallurgical Analysis.

This section focuses on the compositions of the material surrounding corroded regions as well as the composition of the material in pitted regions. The object is to compare the constituent percentages in order to determine the elements associated with this process. Of particular interest in this investigation is the distribution of copper, manganese and magnesium. These measurements were taken from base metal alloy, AMC200 (2124), by X-ray diffraction techniques after the sample had been polished and soaked in 3.5% NaCl solution for 24 hours.

The result of compositional analysis of the base material before corrosion showed the average values to be within expected ranges. Individual readings for Mn, however ranged from 0.84-0.19%, indicating the presence of Mn rich and Mn depleted regions. Similarly for copper (2.89-5.05), rich and deficient areas are apparent. Also of interest is an increased magnesium content in the initiation region, together with a lower than average matrix Mg content, in agreement with work by Imeson and Bartlett[100]. From these results, it can be assumed that the existing areas of compositional variation are associated with sites for

preferential corrosive attack.

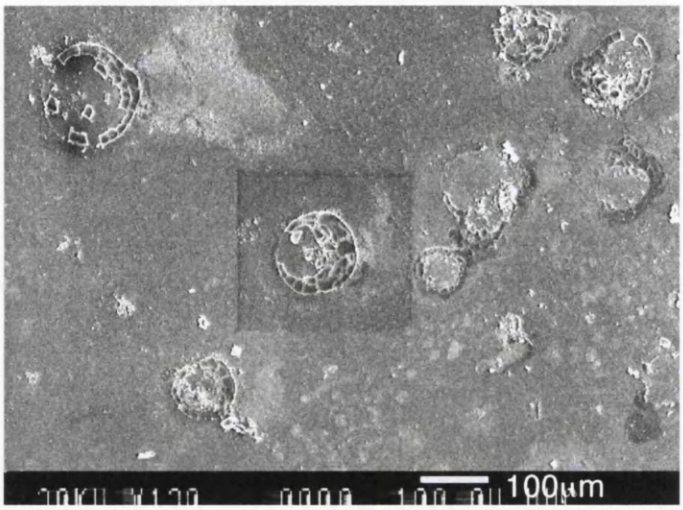

Figure 50.

Results obtained from the centre of the pit in the centre of figure 50.

Elmt	Element%	Atomic%
O	20.51	30.62
Al	75.83	67.13
Si	3.37	2.87
Mn	0	0
Cu	1.18	0.44

Table 8.

Results from general area surrounding the central corrosion pit of figure 50.

Elmt	Element%	Atomic%
O	15.17	23.74
Al	79.29	79.29
Si	1.77	1.58
Mn	0.74	0.34
Cu	3.63	1.43

Table 9.

Figures 51 and 52, overleaf, show the texture of the material. The light grey patches are surface silicon carbide particles. Some of these stand proud of the surface because they are much harder that the surrounding matrix material which was polished away more

quickly. In figure 51, the extrusion direction can clearly be identified, horizontally.

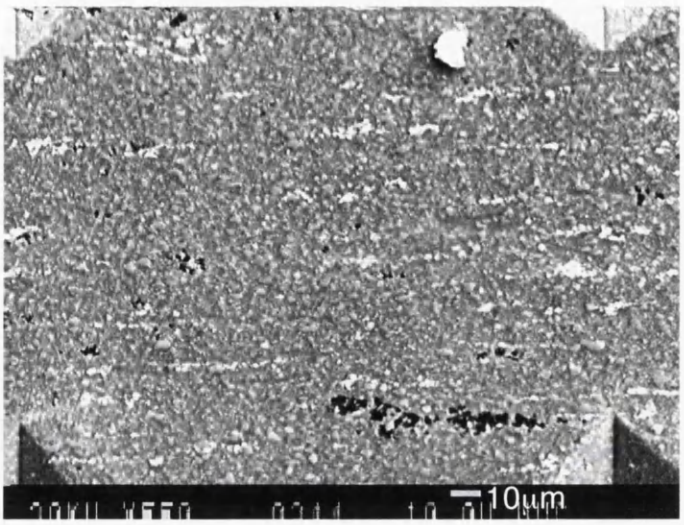

Figure 51.

AMC225Xe T1 heat treated material. Ground and polished sample with extrusion direction running from left to right of the picture.

Figure 52 exhibits no such features and is more isotropic, although the polishing direction may be identified.

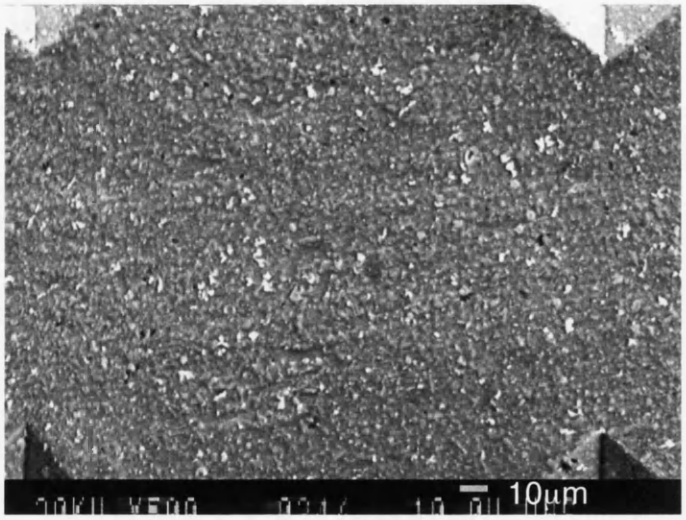

Figure 52.

AMC225Xe T1 heat treated material. Ground and polished sample cut in the transverse direction, perpendicular to the extrusion direction.

This textural difference has an effect on the pit morphology observed on the sides of the specimens and the soaked transverse sections of the material. Round pits are observed in

the transverse sections, and elongated pits in the longitudinal (side) specimens.
Also of some significance is the apparent clustering of SiC particles in the blended material. Transverse disk specimens were examined under a light microscope after polishing. This demonstrated that the blended material consisted of uniformly distributed, very small (15-20μm), clusters of silicon carbide particles, whereas the mechanically alloyed material tended to have a more uniform distribution of particles throughout the microstructure and no obvious clustering.

3. Load controlled LCF.

The results of the load controlled LCF testing are tabulated in tables 14-31 in appendix 2. The data has been plotted in the form of S-N curves in order to make relevant comparisons between the data sets (figures 17-30, p. 88-94).
The results from AMC225Xe, T4 heat treated material tested at 1Hz under a sinusoidal waveform in air, have been plotted in figure 17 (pg. 88). This data has been superimposed on subsequent graphs for the purpose of comparison.

3.1 The Effect of Heat Treatment.

The effect of heat treatment of this material has been illustrated in figure 18 (pg. 88), where data for air tested T1 and T4 materials have been plotted. In agreement with the U.T.S. results, the T1 material is weaker at the high stress end of the curve.
This phenomenon becomes less apparent at lower peak stress and longer life. It should be noted that the final point on the Xe T1 curve and the final two points on the Xe T4 curve may be above the endurance limits of the materials as these samples were not tested to failure due to time constraints.

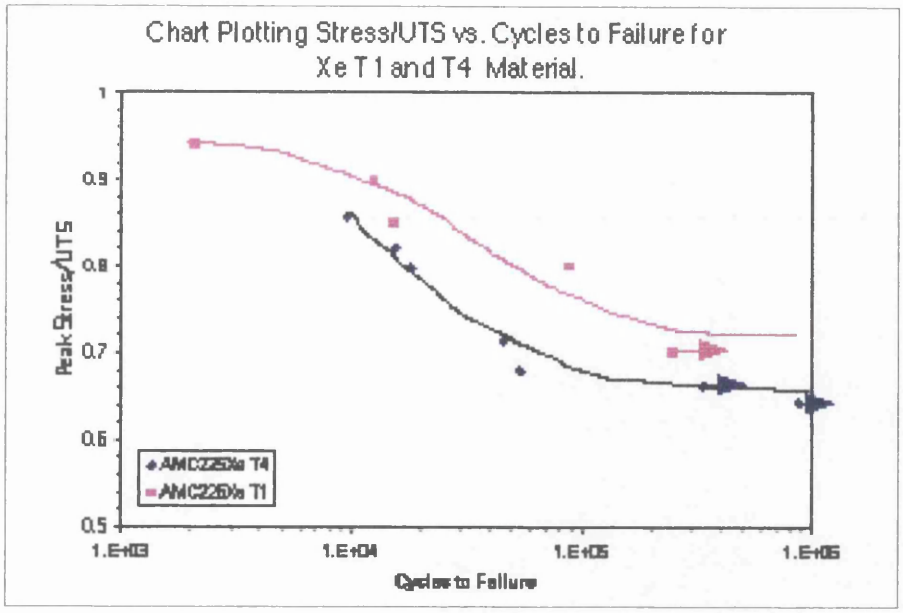

Figure 52.

Figure 52 shows the normalised response to heat treatment, for Xe material, where the peak stress divided by the ultimate tensile stress (UTS) has been plotted against the cycles to failure. The difference between the two sets of data is markedly decreased and the T1 material now shows a slightly better response at the high cycle end of the curve. The endurance limits are 65% (T4) and 70% (T1) of the respective material's ultimate tensile strength.

From the results presented previously for the effect of heat treatment (figures 18-20, pgs. 88-89), it appears that the T4 heat treatment confers greater fatigue resistance when tested in air. This is not the case however when measured with respect to the respective ultimate tensile strength. It then appears that the increase in fatigue resistance is not proportional to increase in ultimate tensile stress conferred by a T4 treatment. If the peak stress is normalised with respect to Young's modulus (figure 53, overleaf), the fatigue resistance is largely the same for both heat treated and untreated alloys in the high cycle and low cycle areas of the graph. This data demonstrates that the fatigue resistance is largely dependent on the modulus of the material.

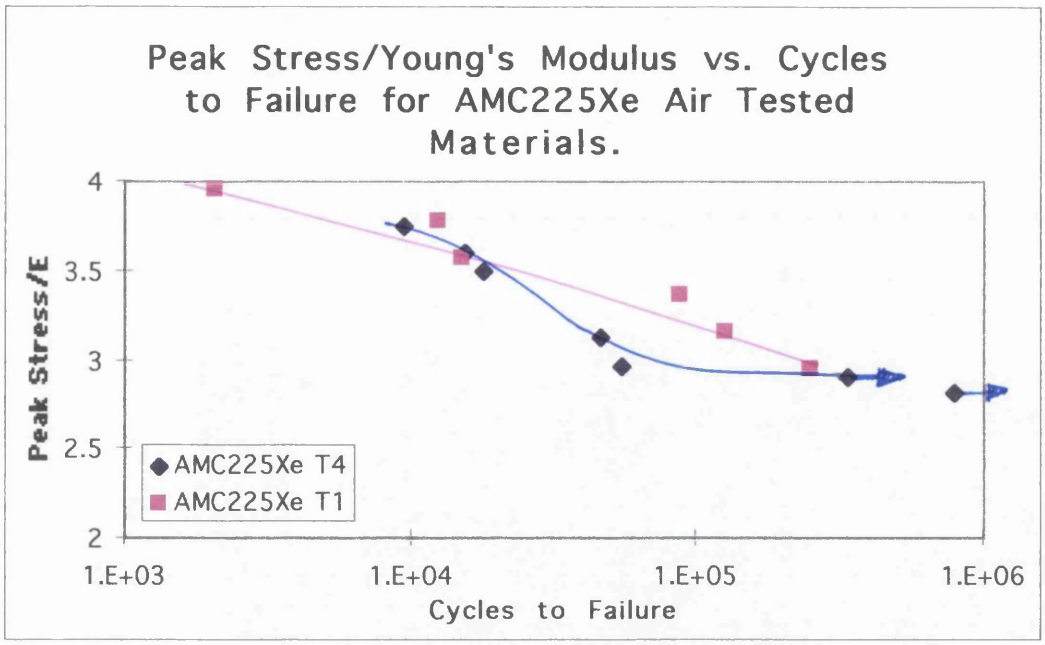

Figure 53.

2.2 The Effect of Processing Route.

The effect of processing route and alloy variants has been illustrated in figure 21 (pg. 90), where a relatively close correlation is found between mechanically alloyed and powder blended materials.

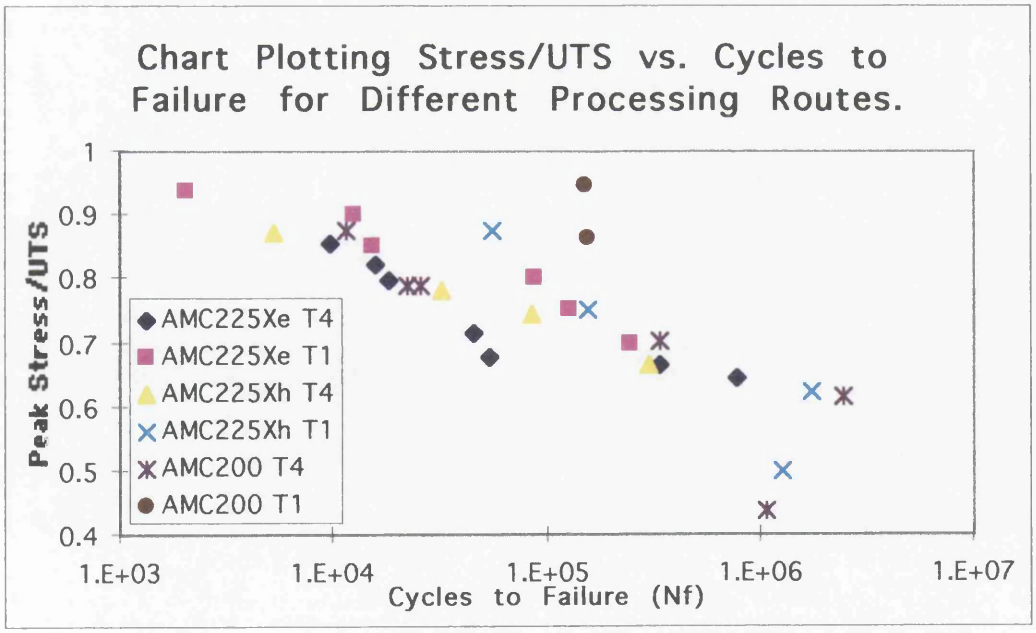

Figure 54.

With respect to the UTS an inverse response is observed (figure 54). Again, it should be noted that the UTS obtained experimentally was used in this case and that the resulting data obtained for the Xe T4 material was erroneous and significantly higher than expected. From the summary of the alloy responses in figure 21 (pg. 90) and figure 54, it can be seen that the relative UTS of the alloy is the major determining factor in its position on the stress axis. The T4 condition alloys having undergone a solution heat treatment at 505^0C for one hour and a cold water quench, followed by natural aging at room temperature therefore provide the best fatigue response for each of the alloy types. The difference between the Xe material and the Xh material is small and probably within the bounds of experimental scatter. The base material is not dramatically weaker. This is indicative that the particulate additions do not play a significant role in the initiation and growth of cracks. At a life of 10^5 cycles, the average peak stresses are approximately 430MPa (T4 base alloy), 460MPa (XhT4) and 470MPa (XeT4). In contrast to this, the average peak stresses for the T1 alloys is significantly reduced, 270MPa (T1 base alloy), 300MPa (Xh T1) and 390MPa (XeT1). This demonstrates that the matrix and precipitation hardening process plays a dominant role in the fatigue process. The fatigue initiation, involving the formation of slip bands and consequent separation of these slip bands under tensile and shear stresses may occur independently from any interaction with the silicon carbide particles. The slip band formation, separation and ensuing cracking will follow the path of least resistance, in the weaker regions.

The T1 microstructure is produced by cooling from the elevated temperature (where, during the production process, any shaping is carried out), and naturally aged. This produces a more overaged and weaker condition compared to the T4 material. The lower average stresses observed in the T1 materials are a consequence of the overaged precipitates produced.

In summary, the major determining factor influencing the fatigue response of the material, tested in ambient conditions is the heat treatment and subsequent mechanical strength, not the composition or production route.

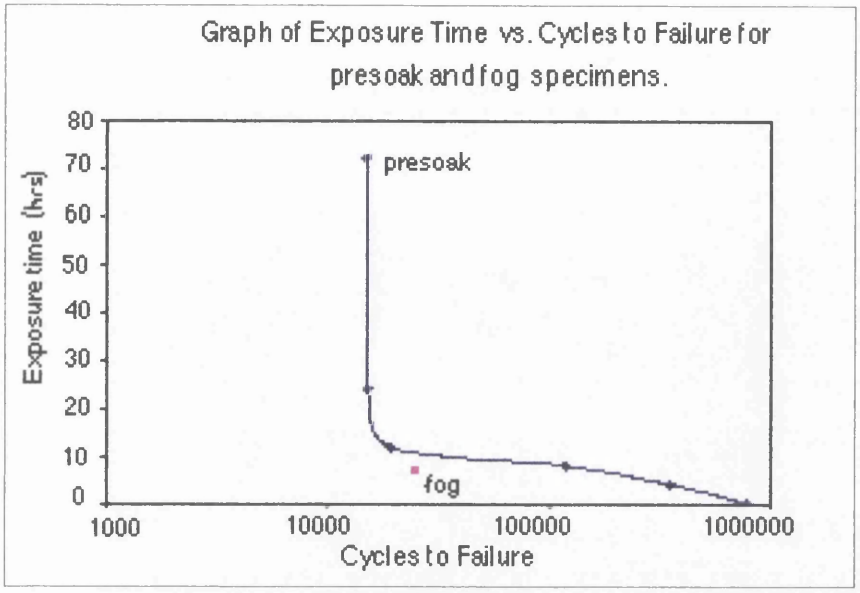

Figure 55.

Figure 55 shows a plot of AMC225 Xe T4 material tested at 350 MPa, 0.1 Hz and R=0.1 after various presoak times. The equivalent stress for a fog tested sample has been superimposed on the graph to demonstrate that when a sample is fatigued at 0.1 Hz, R=0.1 in a saline environment, the time to failure is reduced. In other words, while an 8 hour exposure to a saline solution and subsequent fatigue cycle result in failure after 32 hours, (116,535 cycles), the sample tested in a saline fog atmosphere failed in under 7 hours exposure (at 24,916 cycles). This suggests that a fatigue cycle imposed during exposure accelerates environmental damage. From this graph, it should also be noted that a vast reduction in fatigue life occurs between 1 and 12 hours exposure time (10^6 to 17000 cycles), but at longer exposure times there is no significant further reduction in fatigue life, suggesting that a saturation point in terms of environmental damage has been reached.

Environmental effects are demonstrated in figure 22 (pg. 90), showing the fatigue response of the mechanically alloyed T4 composite tested in air, in fog and after a salt solution presoak.

The strength of the alloy is significantly decreased on exposure to saline conditions. It should be noted however that the presoak data demonstrates a greater degree of scatter

than those of the fog tested data. This phenomenon is also demonstrated by comparing tables 15, 16 and 19 in appendix 2. Table 15 shows that soaking in a salt solution has a marked effect after only 4 hours and has reached a peak effect by 12 hours, in agreement with the data presented in figure 55. The unpredictability of the severity of pits introduced during the soaking process will be discussed in further detail later in this chapter.

From figures 22-26 (pgs. 89-91, showing environmental effects on fatigue), it can be seen that the reduction in fatigue life on introduction to a saline environment is common to all materials. The presoaked specimens tend to have lower fatigue responses than the fog atmosphere tested samples at the high stress/low cycle end of the curve. This is not entirely unexpected as at these stresses, the fog atmosphere tested samples have a short exposure duration (1000 cycles is approximately 15 minutes of exposure time, 10,000 cycles, 2hrs 45mins and 100,000 cycles, 27 hrs). Since the detrimental effects of the saline conditions typically reach a peak at about 12 hours exposure to solution the 24 hour exposed presoaked specimens would be expected to be weaker. As the exposure time increases (at the low stress/high cycle end of the fatigue curve), the presoaked specimens tend to have comparably better fatigue responses than the fog tested specimens. It can be concluded that the presoaking introduces defects which reduce the fatigue life of the specimen at high stresses, but an endurance limit may still be identified at lower stresses. In the case of the fog tested samples, there was an obvious decrease in fatigue life, even at short exposure times (high stresses) which demonstrates significant immediate environmental influence. Also, all of the specimens tested in a salt fog atmosphere failed, regardless of the stresses imposed. In other words, an endurance limit was not identified even at relatively low stresses, suggesting that the corrosion/fatigue process is more damaging than either fatigue or corrosion process alone in agreement with other work (refs. 137, 138, 139).

Figure 27 (pg. 93) shows the response of all the materials tested in a salt fog atmosphere. Since the response of all the alloy variants falls in the same narrow band, it can be assumed that the processes involved are common to all the materials, irrespective of the production route or heat treatment. Since the base material contains no silicon carbide particles, it can be assumed that these play no significant role in the corrosion/fatigue

process. Furthermore, since the metal matrix composites behave in an almost identical fashion to the base matrix material, the damage events must be occurring in the matrix. The similarity between the T1 and T4 heat treated alloys also suggests that the precipitate morphology does not influence their progression.

2.4 Effects of Frequency.

The effects of various waveform frequencies are shown in figure 28 (pg. 93). This data falls well below the fatigue strength of the air tested baseline data. A negligible effect on fatigue life due to the waveform frequency effects is demonstrated by the fact that the fog tested data fall within the same narrow band, despite a two order of magnitude change in testing frequency (0.1-10Hz). This demonstrates that crack growth or crack advancement per cycle is similar, regardless of the exposure time of the new fracture surface to the saline environment. This implies that the damage initiation period is short, well within the testing time of the various testing frequencies evaluated. On this basis it is relevant to compare the alloy variants tested in salt fog at 1Hz with the corresponding alloy variant, tested after a 24 hour exposure to salt solution (figures 22-26, pgs. 90-92).

2.5 Effects of R-ratio Variation.

Effects of R-ratio variation (mean stress effects) were examined (figure 29, pg. 94) and show that an R value of 0.5 in a fog atmosphere generates a higher S-N curve than that for R=0.1 under the same conditions.

Figure 30 (p. 94) shows a plot of stress range against cycles to failure. This demonstrates the effects of mean stress on the fatigue life of AMC225Xe T4 material tested in air and salt fog. This plot shows that the samples tested at the higher mean stress of R=0.5 have a have a much shorter fatigue life than those tested at R=0.1. This result is not an unexpected. A Goodman and/or Gerber plot would give a better visual image of the role of the mean stress and stress amplitude on these materials, and hence further testing would be advisable.

To summarise, the fact that fatigue response of the base alloy and the metal matrix composites is similar for both the presoaked and salt fog tested conditions, suggests that pit formation is confined to the matrix. The EDAX measurements on the electron microscope confirm this, indicating the presence compositional variation within the base matrix material. There were magnesium, manganese and copper rich and depleted regions. The magnesium content of the region surrounding a pit initiation site was found to be significantly lower than average. Manganese was found to be within tolerance limits in the initiation region, whereas the pit itself was found to be significantly manganese deficient. Copper was found to be decreased in the region of initiation and significantly depleted in the pit itself. Individual readings for copper taken from base matrix material after a 24 hour soak in saline solution (table 5, pg. 97) range from 2.89% to 5.05%. This indicates regions of depletion and regions of deposition

It is argued that pit initiation occurs in the matrix at locations where there are compositional variations which allow anodic and cathodic regions to develop, promoting anodic dislocations and pit formation.

4. Crack Propagation.

4.1. Fatigue Crack Growth.

The results for each alloy type tested in air and salt fog conditions are plotted in figures 37-39 (pgs. 100-101).

The baseline data (T4 heat treated condition for each alloy) measured in laboratory air are shown in figure 56.

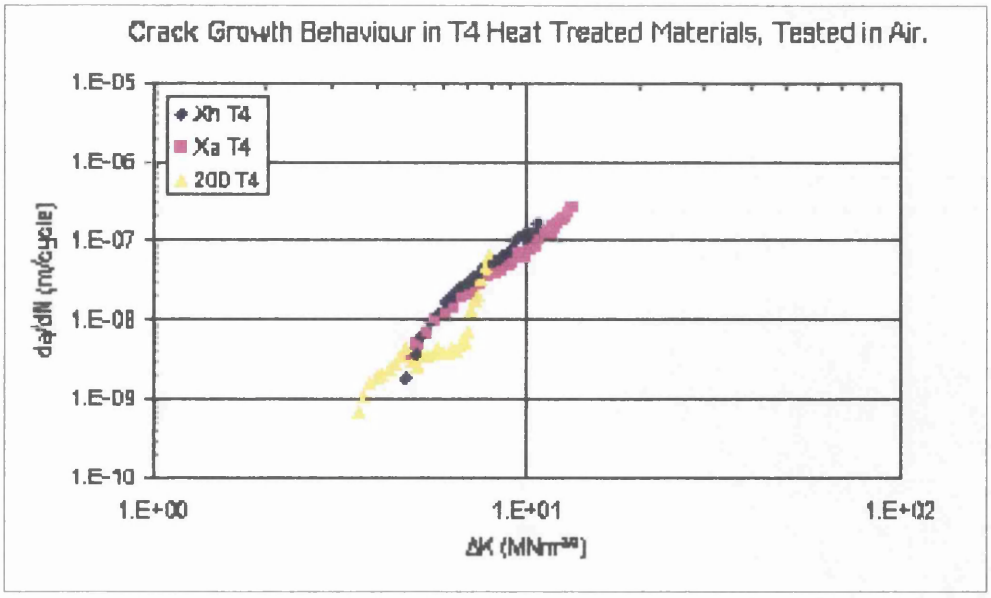

Figure 56.

There is very good correlation between the data sets between ΔK values of approximately 8 to 16 $MNm^{-3/2}$, which suggests that the previous data also correlate well with each other in this region. At lower values of ΔK, however, distinct differences in the growth rates are apparent with the AMC200 material showing significantly slower growth.

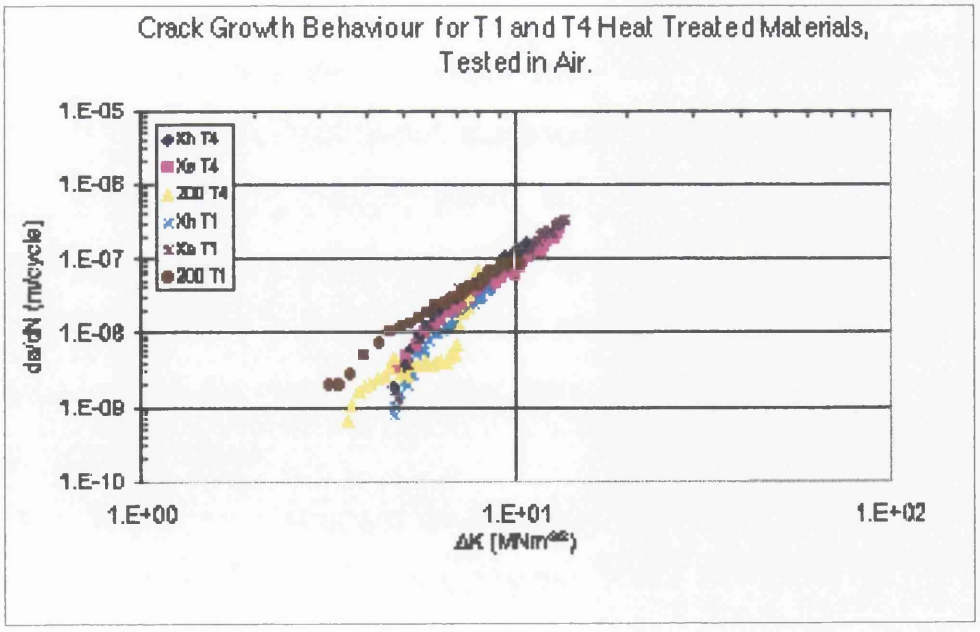

Figure 57.

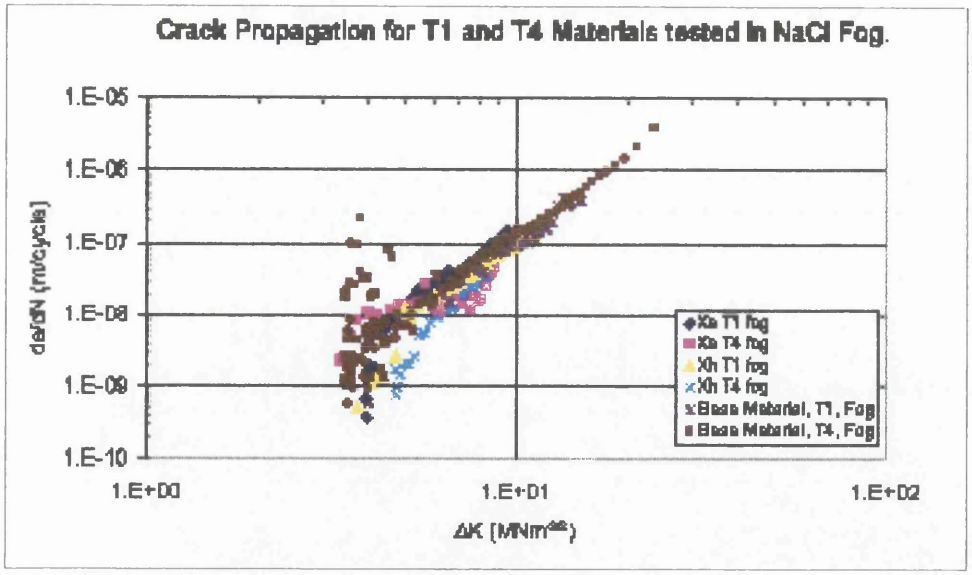

Figure 58.

The data for all material variants tested in a saline atmosphere are presented in figure 58. This graph demonstrates very good correlation between the data sets, indicating a similar response to corrosion fatigue throughout. The Xh T4 material appears to exhibit a slightly slower crack growth rate at low values for ΔK which is probably due to statistical scatter.

4.2 Crack Propagation Prediction For Design.

Pitting due to corrosion is increasingly, a major concern for the aircraft industry. It is widely recognised that the 2000 and 7000 series aluminium alloys from which most airframes are constructed are susceptible to pitting corrosion. In the past this was not considered to be a major design problem, but increasingly airframes are being kept in service for much longer times and pitting corrosion is becoming much more extensive in these aging aircraft. Reliable design criteria are required to allow the impact of corrosion pits on mechanical integrity to be safely predicted.

The presence of defects as a consequence of exposure to the salt environments might imply that the lives of the test-pieces are controlled by the rate at which the cracks grow to failure. On this basis, it should be possible to calculate the lives to failure through a fracture mechanics integration based on measured growth rates. To support the calculation, growth

rate measurements were made in air and salt fog environments at R = 0.1 and a cyclic frequency of 1 Hz, for each of the six alloy variants. The data presented here are in the form of da/dN vs. ΔK graphs. The results are recorded in figures 37-39 (pages 100-101).

The data generally follow a Paris law relationship of the form:

$$da/dN = C\Delta K^m$$

with C a constant, m the Paris exponent and ΔK the stress intensity factor range ($\Delta K = K_{max} - K_{min}$).

Interestingly, there is generally little difference in the growth characteristics between the different MMC alloy variants and environmental states for the tests conditions used. The deviation from the linear (on a log-log basis) Paris law at low stress intensity factors is an anomaly of the test technique and reflects the period when the crack is growing out of the influence of the initial starter slit. The similarity in growth rate response is clear from the measured m and C values as recorded in Table 10 below.

Material	Test condition	'm' exponent	'c' exponent
Xe T4	air	3.51	3.47e-11
	fog	3.86	1.38e-11
Xe T1	air	3.51	3.46e-11
	fog	4.58	5.04e-12
Xh T4	air	3.89	9.70e-12
	fog	3.89	9.53e-12
Xh T1	air	4.73	1.51e-12
	fog	3.69	2.18e-11
Base T4	air	3.20	9.73e-12
	fog	3.34	6.02e-11
Base T1	air	2.76	1.42e-10
	fog	3.56	2.56e-11

Table 10. Paris constants and exponents.

The data suggests however, that complicated interactions may be occurring at low growth rates. This is particularly evident in the data for the 2124 base alloy. A more detailed set of experiments, which were beyond the scope of the present programme, is required to define the nature of such small crack interaction mechanisms. It is important to appreciate also that the deductions made above are specific to the testing conditions employed. Previous work (ref.189) clearly demonstrated, for similar MMC materials in salt solution, that the relative

response to a salt environment compared with air is strongly dependent on test frequency and R value. While this may have far reaching consequences for the design and operation of engineering structures, it was not taken into consideration in the present work as insufficient testing was carried out under these various conditions.

4.2.1 Pits as stress concentrators.

The metallographic examination has shown that the pits have an irregular geometry but that, in general, their morphology is semi-ellipsoid. For the purpose of the finite element stress analysis (P.J.Nicholas – private communication of unpublished work), the pits were modelled as regular, semi-ellipsoid shapes. The general geometry is illustrated in figure 59. The analysis explored the effect of variations in the a:b:c ratio on the elastic stress concentration factor, K_t, at the free surface and the deepest point (normal to the free surface) of the ellipsoid. The a, b and c dimensions used in the analysis were based on measurements made on real pits.

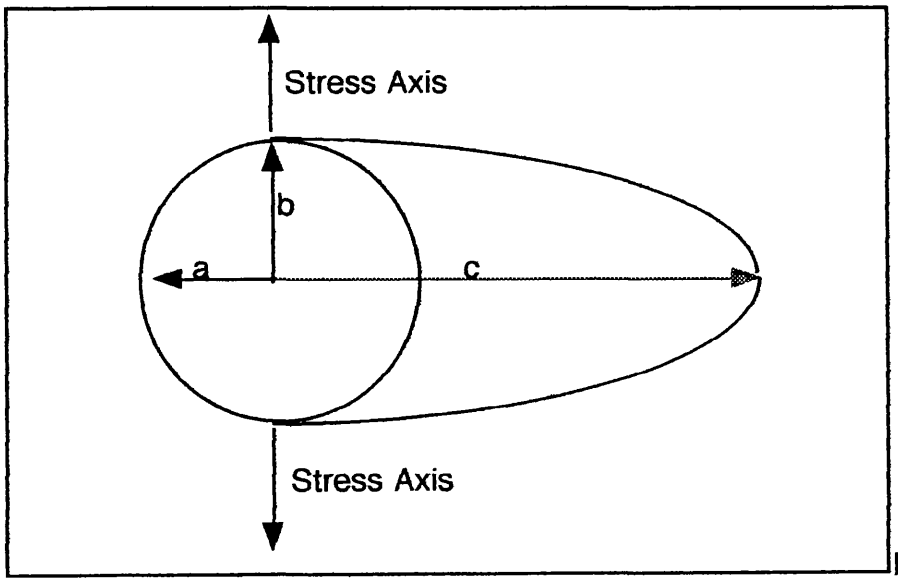

Figure 59.

Figure 59 is a schematic diagram of a pore showing 'a', 'b' and 'c' directions, where, 'a' and 'b' are surface measurements of a pore, while 'c' is the depth. While a range of pore sizes was covered in the stress analysis, it is the *relative values* of these dimensions which is of

importance.

The calculated K_t factors derived from polynomial fits to the stress fields at the simulated pits are recorded in table 11.

Pore shape		max/nom	max/nom
a: b: c ratio		Normal to surface	Parallel to surface
1:1:1		1.8	1.69
4:4:4	(Four times size)	2.05	1.94
4:1:1	(Elongated perpendicular to snom)	2.44	1.85
1:1:4	(Elongated towards the specimen centre)	1.89	2.07
1:4:1	(Elongated parallel to the loading direction)	1.16	1.18
2:2:2	(Double size)	1.96	1.85
2:1:1	(Elongated perpendicular to snom)	2.18	1.84
1:1:2	(Elongated towards specimen centre)	1.94	1.92

Table 11, where max/nom denotes $\sigma_{max}/\sigma_{nom}$.

These are idealised shapes which were not meant to represent the more complex pitting observed in practice. However, it is believed that the values quoted are representative of the average stress concentration arising at the real defects. Locally, there could be stress peaks significantly different to these measurements. However, it is argued below that such variations may not be significant in relation to the overall fatigue performance of the flaws.

It is clear that irrespective of pit shape or dimensions, the maximum stress concentration factor is in the range 1.8 to 2.18 except for the 4:1:1 morphology where it rises to 2.44. This last shape is the least likely of the geometries observed in practice. On the basis of these observations, it was assumed that the real pits have a general K_t factor of 2. This value is used below in an analysis of the fatigue response of the MMC alloys in salt environments.

4.2.2 Predicting the fatigue response of pitted test pieces.

There are two important ways in which the fatigue response of damaged test-pieces and structures can be predicted. These are:

a. To apply a 'safe life' approach based on S-N (stress-life) curves in which the corrosion pits are treated as stress concentrations.

b. To adopt a 'damage tolerant' approach by assigning the pits an Equivalent Initial

Flaw Size (EIFS) as a means of calculating residual crack propagation lives.

Each of these is considered below.

4.2.2a Safe life design.

In a previous programme of work, the effect of notch geometry on the low cycle fatigue response was explored for similar MMC alloys to the present work (ref. 182). The earlier measurements were carried out in air on machined notches. It was found that the notch results could be correlated with strain control data on plain specimens. This was achieved by plotting round cylindrical notch (RCN with K_t = 1.92) and double edge notch (DEN with K_t = 1.92) specimen lives in terms of $K_t\Delta\sigma$ with $\Delta\sigma$ the applied nominal stress range. The plain specimen lives were expressed in terms of the measured stabilised stress range (ref. 183). A typical graph based on this earlier work is presented in figure 60. This graph amalgamates strain control data on plain specimens at R = 0 and -1, strain control torsion data and notch measurements from tests on RCN and DEN geometries. The interesting fact is that the graph also includes measured lives obtained on pitted specimens. These are introduced by taking the FE calculated average K_t factor of 2 for the pits. Using the derived $K_t\Delta\sigma$ for the exposed samples, it is clear that there is good correlation with the mechanically notched specimens. The correlation applies irrespective of whether the pits are produced progressively in salt fog or introduced prior to fatigue testing by immersion in salt solution.

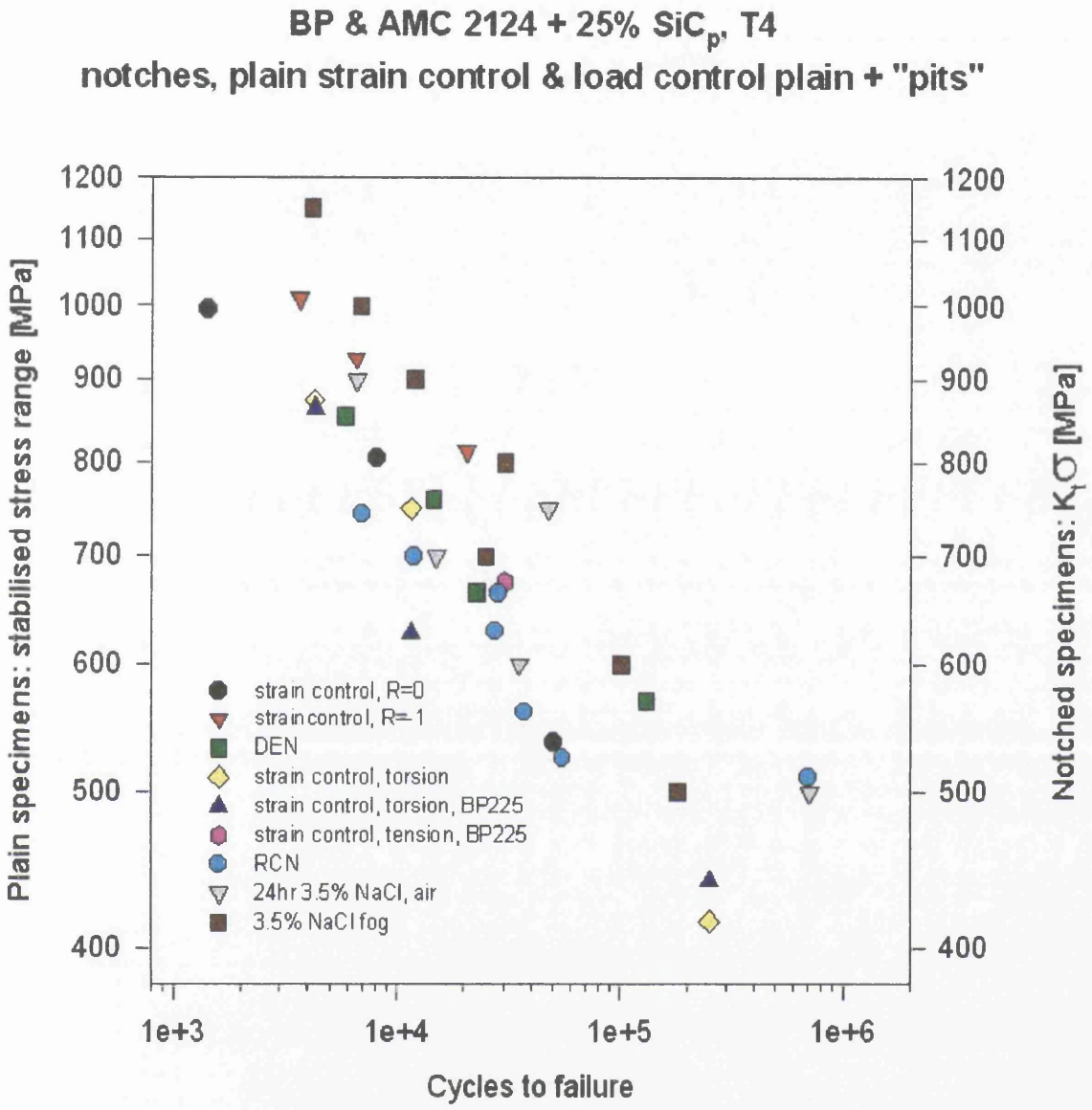

Figure 60.

An additional important piece of information from the graph of $K_t\Delta\sigma$ against life, figure 60, is the observation that the stabilised stress range from strain control experiments on plain specimens also correlates with the notch and pit data. This correlation is consistent with the critical strain lifing approach which is often used to predict the behaviour of stress raisers

from plain specimens. In the critical strain approach it is assumed that if the strain at the root of a notch and in a plain specimen is the same, then they will develop a crack in the same number of cycles. Generally, the stress range in the strain control test stabilises to a constant value after a small fraction (5-10%) of the overall fatigue life. In the present materials, it has been shown previously that there is a strong tendency to cyclically harden and that the stress range moves towards an essentially elastic state. The cyclic hardening will curtail the degree of plasticity at notch roots. It is not surprising, therefore, that the plain specimen 'elastic' stress range provides a good prediction of the peak elastic stress range at the notch root.

Defining the pits in terms of a stress concentration factor offers an interesting design curve approach for establishing the impact of corrosion pits on fatigue performance. It might be argued that the assumption of a regular ellipsoidal shape is not strictly representative of the real geometry of the corrosion pits. This may countered, however, by stating that the irregularities will generally lead to localised K_t factors that are significantly higher than 2. On a $K_t\Delta\sigma$ basis, this is advantageous as machined notches with $K_t > 2$ demonstrate. Plotted this way, the higher K_t notches have longer lives for a given $K_t\Delta\sigma$ stress level (ref. 183). This 'improvement' in fatigue performance is attributed to a smaller critically stressed volume for the initiation of fatigue cracks at high $K_t\Delta\sigma$. In the present case if the cracks at the pits initiate in regions of lower stress concentration factor due to a larger stressed volume of material they will quickly grow into adjacent regions at higher $K_t\Delta\sigma$ and rapidly surround the pit thereby negating the irregular pit shape.

4.2.2b Damage tolerant design.

The alternative damage tolerant approach for defects assumes that the life of the test-piece or component is determined by the rate of crack growth from the initial defect dimensions to a crack size at which failure occurs. The calculation method assumes there is no crack initiation. It is based on the integration of the Paris power law relationship between the initial

and final crack sizes. The general form of the resultant expression is (ref. 184)

$$N = 1 / CY^{m}F(\Delta\sigma)^{m}\Pi^{m/2}\{a_f^{(1-m/2)} - a_0^{(1-m/2)} / (1-m/2)\}$$

The C and m are the constant and exponent from the Paris relationship. The 'Y' term is the geometry factor from the expression below for the stress intensity factor. For through section cracks in simple structures such as thin plates, Y is usually expressed as a polynomial function of crack size 'a' and width, 'w', of the structure i.e. Y = f(a/w). In the present case, however, the cracks have a part through form and the test-piece has a cylindrical geometry. This requires a more complicated expression for Y of the form:

$$Y = M_G M_S M_B \phi$$

With M_G, M_S and M_B general, side-face and back-face geometry correction factors and ϕ a relationship that accounts for elliptic crack shape. The stress function $F(\Delta\sigma)$ is also from the expression for stress intensity factor. The functional form is used in recognition of the fact that the cracks might be growing in a stress gradient. In the present case, a plain specimen geometry is used and a simple tensile load is applied so that $F(\Delta\sigma) = \Delta\sigma$. On this basis, the expression for the stress intensity factor can be expressed as:

$$\Delta K = Y\Delta(\Pi a)^{1/2}$$

With $\Delta K = K_{max}-K_{min}$, the applied maximum and minimum stress intensity factors in the fatigue cycle.

Knowing the applied range of stress, $\Delta\sigma$, and C and m from the crack growth data, the requirement is to establish 'Y' for the present pit/specimen geometries, a_0 the initial crack size and a_f, the final crack size, in order that the number of propagation cycles to failure can

be calculated. There is relevant published information on Y factors for semi-circular and semi-ellipitical cracks in cylindrical test-pieces. A graphical presentation of such work is reproduced in figure 61 (ref . 185). The graph shows Y values in terms of the ratios a/D, with 'a' the crack depth and D the specimen diameter, and a/l with '2l' the crack length along the specimen circumference.

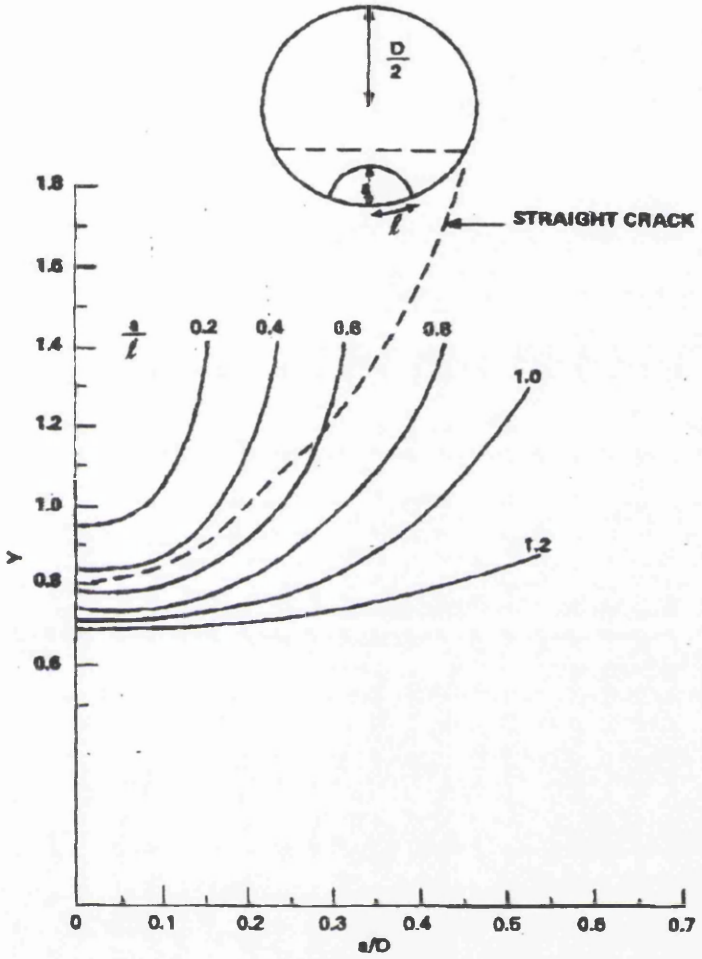

Figure 61.

The maximum measured pit depths were approximately 100 μms. The specimen diameter was 5 mms, so that a/D < 0.05 (c.f. figure 61). The pit shape also tended to be either slightly elongated along the specimen diameter or approximately semi-spherical in form. On this basis, a/l = 1 is not an unreasonable approximation. These two pieces of information yield Y = 0.7. Sensitivity studies confirmed that variations between 0.6 and 0.8 do not alter the calculated lives significantly. Figure 61 shows that for the range of a/D encountered, the Y value is virtually constant.

The calculation approach was to assume specific initial flaw sizes, a_0, that cover values typically found in test-pieces (i.e. 20, 40, 60, 100 μms). Then to calculate propagation lives, N_p, for stress ranges, $\Delta\sigma$, which span the values applied to the test-pieces. From this base, direct comparisons with the experimental measurements were made. The final crack size at which failure occurred, a_f, was calculated from the fracture toughness for the MMC alloys which previous crack growth work (ref. 183) suggested was approximately 20 $MN/m^2(m)^{1/2}$. Some typical results from this calculation are recorded in table 11. These particular results are based on the salt fog crack growth rate data for the XE T4 variant.

Max. Stress, σ_{max}	200 MPa	300 MPa	400 MPa	500 MPa
Stress Range, $\Delta\sigma$	180 MPa	270 MPa	360 MPa	450 MPA
$a_0 = 20$ μm		Np = 275024		Np = 26790
$a_0 = 40$ μm		Np = 119612		Np = 5157
$a_0 = 60$ μm		Np = 65682	Np = 9500	
$a_0 = 100$ μm	Np = 233074	Np = 21156		

Table 12. XE T4 material, m = 3.86, C = 1.38E-11, R = 0.1

Lines based on this table are superimposed on figure 62 alongside the salt fog and pre-exposed S-N results for all the alloy variants. It is clear that the trend in the S-N data is consistent with the crack propagation results and that the measured lives are predicted by pit sizes in the range 40 to 100 μm. This range reflects the pit sizes measured in practice. The fact that the calculation based on the XE T4 growth rates is consistent with the measured behaviour of all the alloy variants is due to the similarities in Paris constants and exponents. The consistency is confirmed by the sensitivity study recorded in Table 13.

Stress range (MPa)	XE T4	XH T4	XE T1	XH T1	Defect size
450	5157	7175	5442	4088	40 microns
270	119612	168041	159629	90000	40 microns

Table 13. Relative crack propagation lives, N_p, for alloy variants.

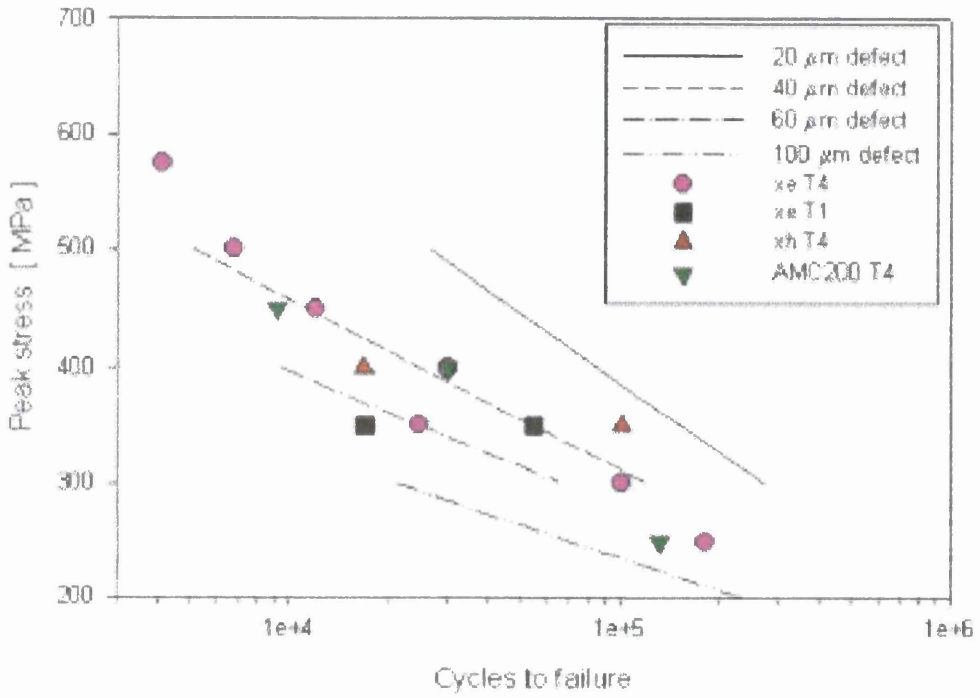

Figure 62.

4.3 Overview.

An important implication from the calculations carried out is that the corrosion pits develop more rapidly under the action of the cyclic stress. The application of the fracture mechanics approach to pre-existing flaws caused by prior exposure to the salt solution is plausible and consistent with the analysis of defects arising for other reasons e.g. foreign object damage and casting flaws. However, the success of this method with the pits arising from cyclic testing in salt fog is more difficult to justify. The explanation must be that the pits develop at a much faster rate under those conditions. After all, the experimental testing on pre-exposed samples suggested times of 48 hours for pits of 20 µm. This is far longer than many of the fatigue tests in salt fog. The pre-exposure work, however, did reveal a large number of small pits after 8 hours or less time. The acceleration under cyclic loading may be a consequence of the action of the stress on such small pits. It would tend to remove corrosion debris from the vicinity allowing fresh metal to be available continually. It would

also cause localised plasticity which could accentuate the tendency for corrosion cells to develop and may promote the ingress of corrosive species such as hydrogen into the metal.

Another important implication is the equivalent success of both the $K_t\Delta\sigma$ and fracture mechanics in predicting the effects of pits on fatigue performance. This may be fortuitous but it could imply that they are alternative views of the same event. This event is effectively growth of cracks to failure from a very early stage in the fatigue process. Interestingly, the stress analysis of idealised pit shapes has shown that there is little variation in K_t factor for a wide range of pit sizes or shapes. Clearly once a pit develops with a K_t approximating 2, crack initiation could be rapid so that the overall life is controlled by the growth rate. There is a requirement here for further work in order to establish the precise relationship between the stress concentration and stress intensity approaches to fatigue in corrosive environments.

5. Fractography.

Optical and scanning electron microscopy showed that for all composite LCF samples, cracks were initiated from surface or near surface locations. In the case of the presoaked samples the initiation site of the fatigue cracks was invariably associated with a corrosion pit. A typical plan view of of this type of fracture surface is shown in figure 63, with the initiation sites and associated corrosion pits visible to the left and lower edges of the picture. There are clearly two initiated fatigue cracks in figure 63, with the most severe defect eventually leading to the failure of the specimen. Figure 64 shows a magnified image of the initiation region, with a pit depth of approximately 100μm. Many additional pits are apparent on each individual specimen. Pitting on the sides of the specimen typically has an elongated profile, generally in the stress and extrusion direction in the specimens exposed to saline conditions for more than 16 hours. This is demonstrated by the appearance of the pits in figure 64 at the bottom left of the picture.

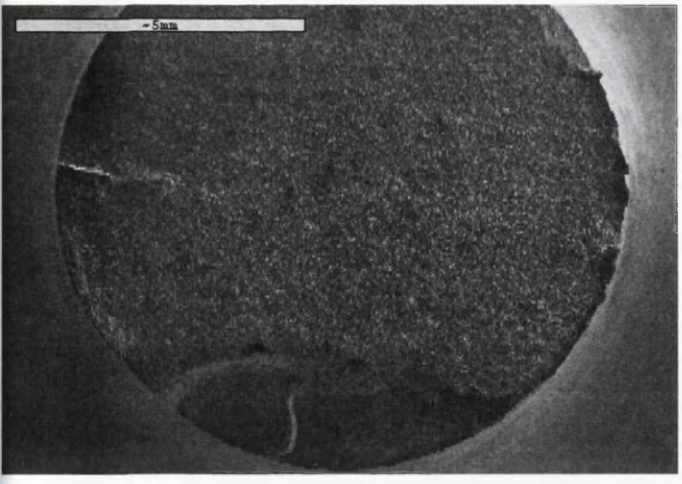

Figure 63.

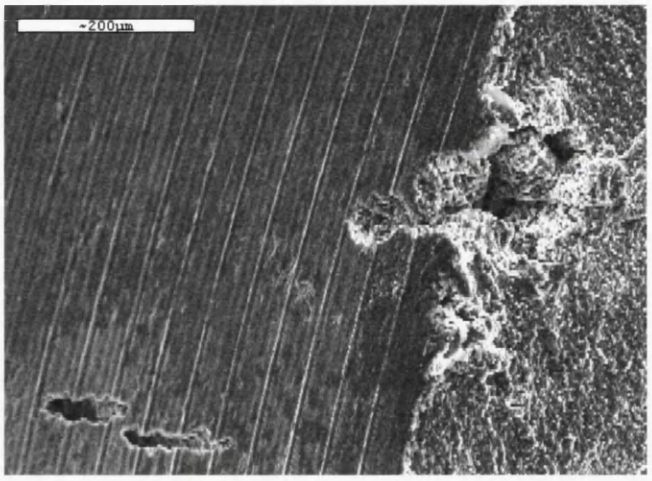

Figure 64.

The following figures (65-70) are all taken from AMC225Xe T1 material tested at 350 MPa after a 24 hour presoak.

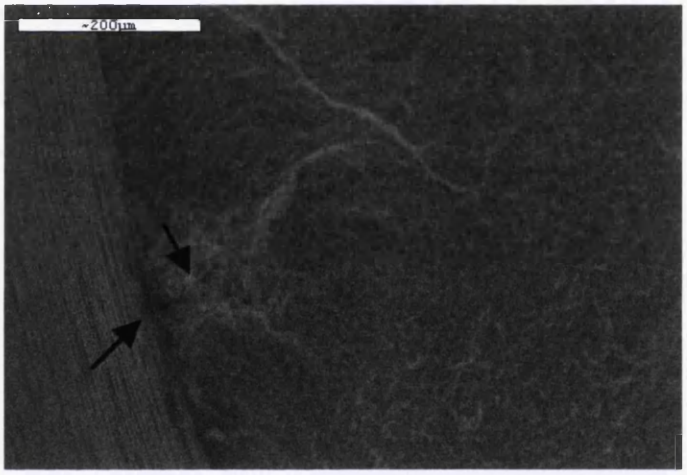

Figure 65.

In figure 65, it can be seen that the major defect in the initiation region is actually about 20µm below the surface of the specimen. The surface of the specimen showed little disruption creating difficulty in predicting the presence of a defect of this size. This is referred to as undercutting or subsurface pitting attack and is typical of pitting which occurs in an aggressive environment (ref. 128).

In figure 66, the illustrated initiation site is probably the site from which the fatigue crack grew, leading to eventual failure. This is supported by the fact that this appears to be the area of convergence of the fatigue markings.

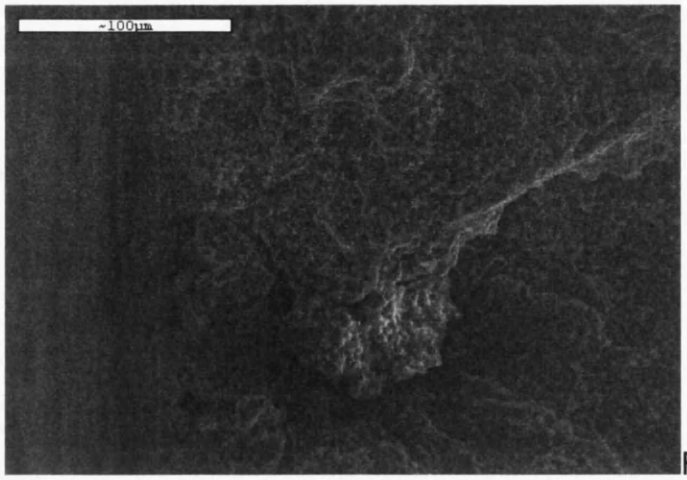

Figure 66.

The region shown in figure 67 appears to have a coating of corrosion product, resulting in the less defined appearance of the fracture surface features.

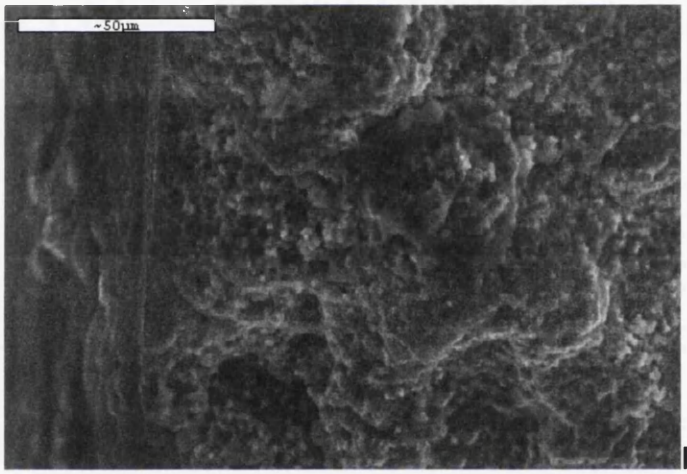

Figure 67.

It should be noted that although any of these three sites may be the flaw which lead to crack propagation and failure, initial microscopic fatigue cracks would probably have initiated in each of these areas and then coalesced to form one large initial flaw. This is probably why the fatigue life for this specimen (16931 cycles) was somewhat shorter than for a similar specimen tested under the same conditions (54846 cycles), in which a single pit developed into the final failure flaw. This supports the theory that there is significant scatter within the salt fog tested data and that more research is required to statistically define this scatter.

Figure 68 presents an area in the slow growth rate region showing large dimples as expected.

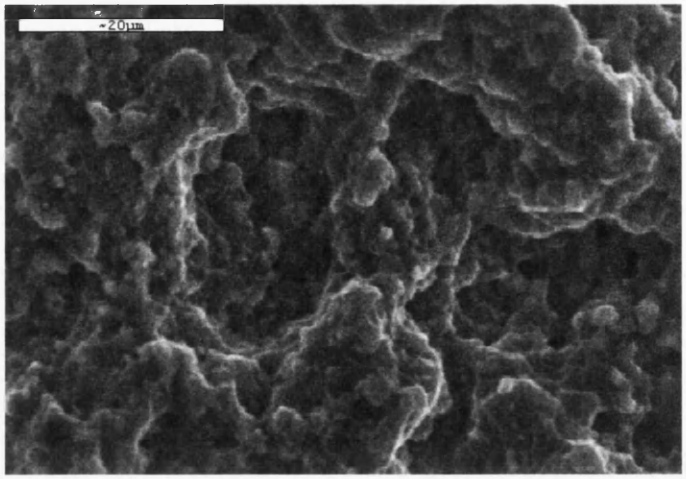

Figure 68.

Figure 69, taken from the fast crack growth rate region, shows much smaller dimples as expected due to the higher crack growth rate in this region.

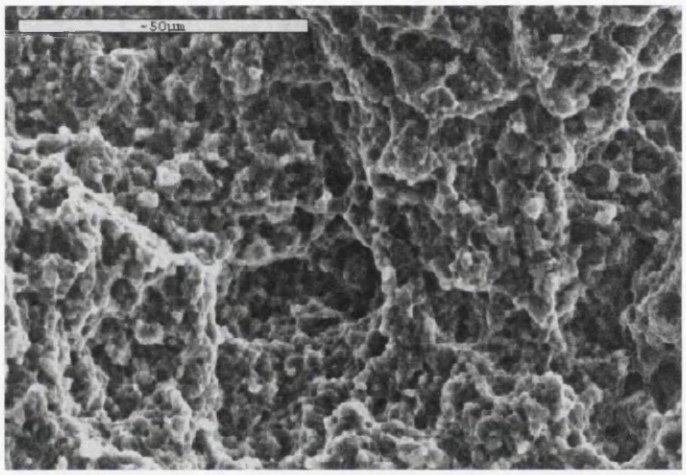

Figure 69.

Figure 70 shows typical ductile fracture features from the overload region.

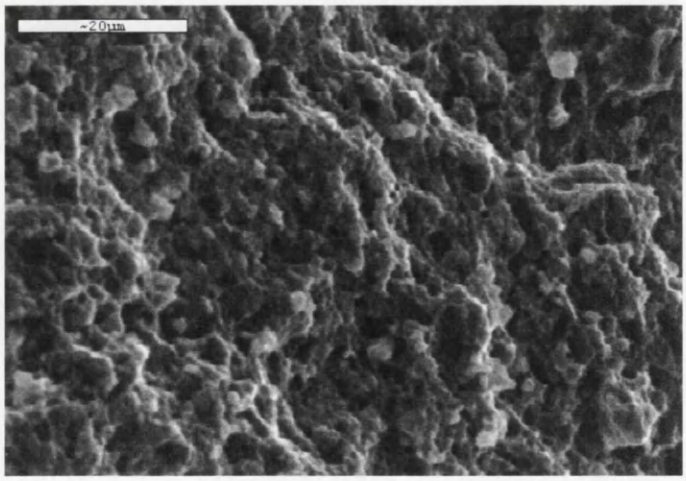

Figure 70.

Figure 73 shows a fracture surface morphology typical of T1 air tested specimens. It shows ripples running perpendicular to the crack growth direction, increasing in width with increasing distance from the initiation point.

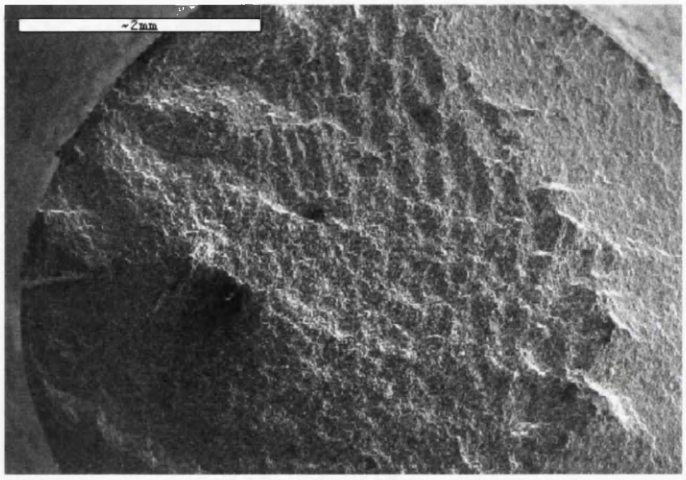

Figure 73.

Figures 63 and 74 are typical of T4 air tested fracture surfaces. The ripple effect is much less pronounced in these samples.

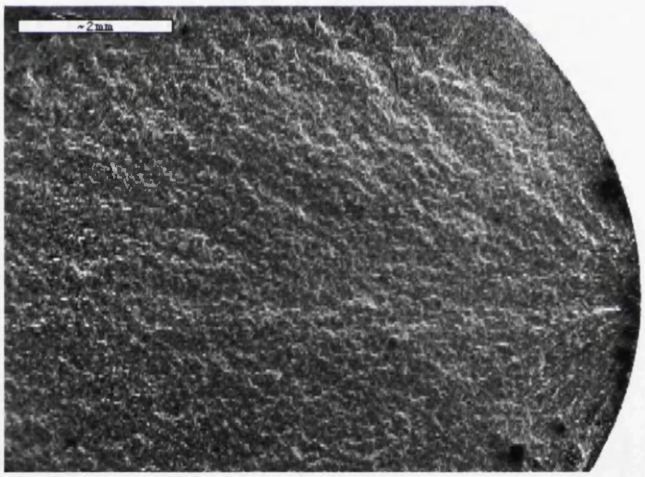

Figure 74.

Initiation of fatigue fractures occurred at the site of a pit in all cases of presoaked and fog tested samples. These pits vary enormously in size so it is not possible to estimate a satisfactory pit size or range for these initial crack propagation flaws.

It can be very difficult to assess the severity of a pit before fracture. Figure 65 shows a good example of a subsurface or undercutting pit. This would not appear to be a severe defect from the surface, but corrosion below the surface was severe enough to cause initiation of a

fatigue crack and subsequent failure. Other defects, such as large shallow surface pits, may appear larger but be less severe. All composite samples tested in air have a similar fracture surface appearance. The sequence of figures 75-82 show typical examples of the features apparent in these samples.

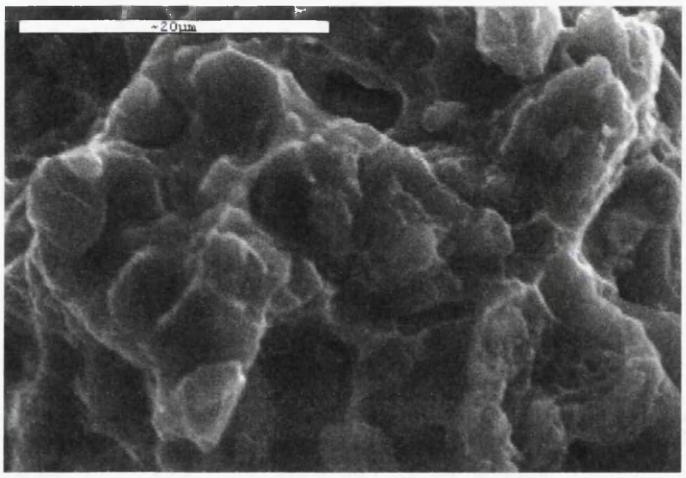

Figure 75. This picture shows the presence of a micro crack in the AMC225Xh T1 sample, approximately 50µm from the initiation point.

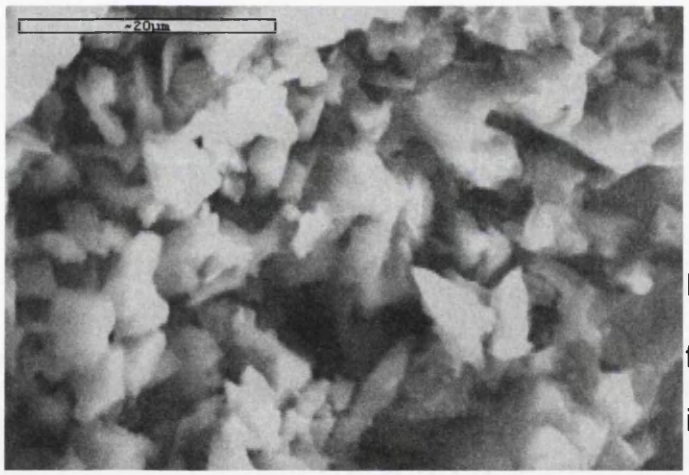

Figure 76. Taken from 90µm into the fracture surface from the initiation point in the propagation direction.

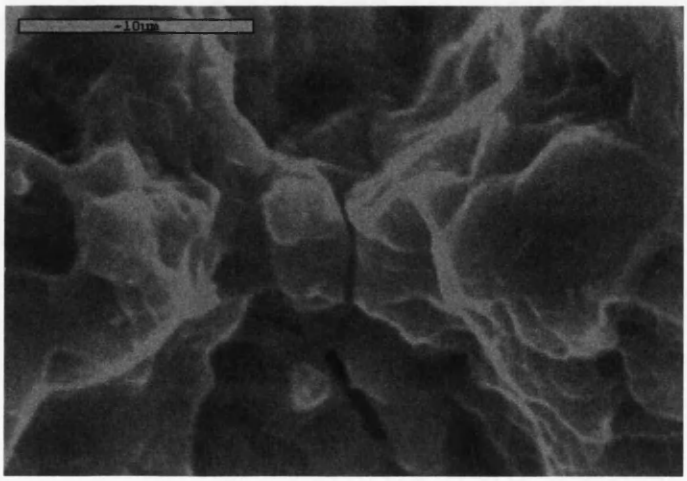

Figure 77. Taken from 1mm behind the initiation pit, this shows a micro crack running from the elongated hole at the bottom of the picture, all the way to the top of the frame. Also many small dimples are apparent.

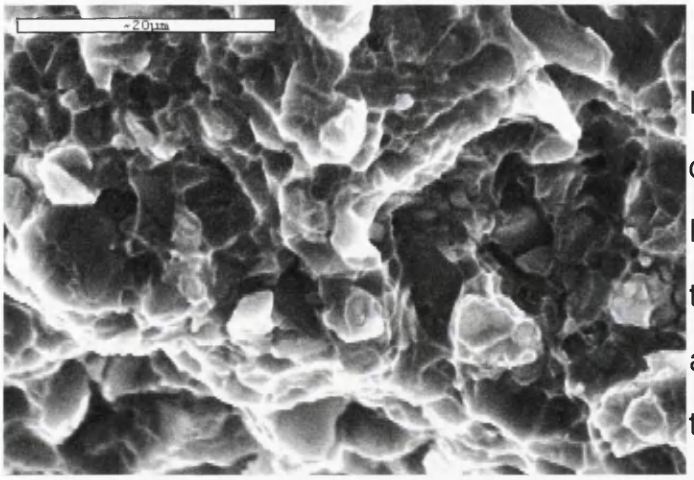

Figure 78. Approximately 2mm in, the dimples have become more apparent. Particle cracking is mostly perpendicular to the direction of maximum stress, although a few were fractured parallel to the stress direction.

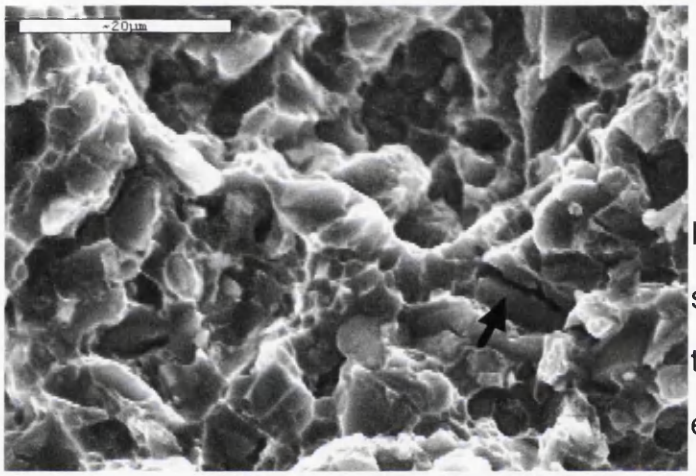

Figure 79. 3mm into the fatigue crack surface, particle cracking (indicated by the arrow) is still very much in evidence, especially in the larger particles.

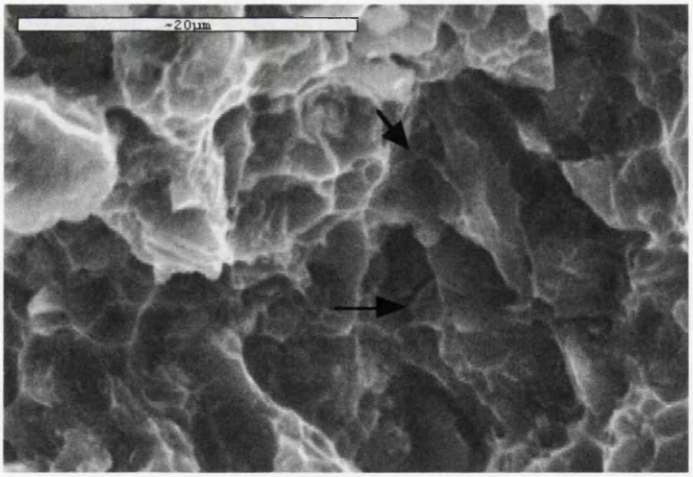

Figure 80. 4mm into the fatigue crack surface, particle cracking is evident only in the large particles (greater than 5µm, shown by arrows) with the prevalent crack advancement mode being particle/matrix debonding.

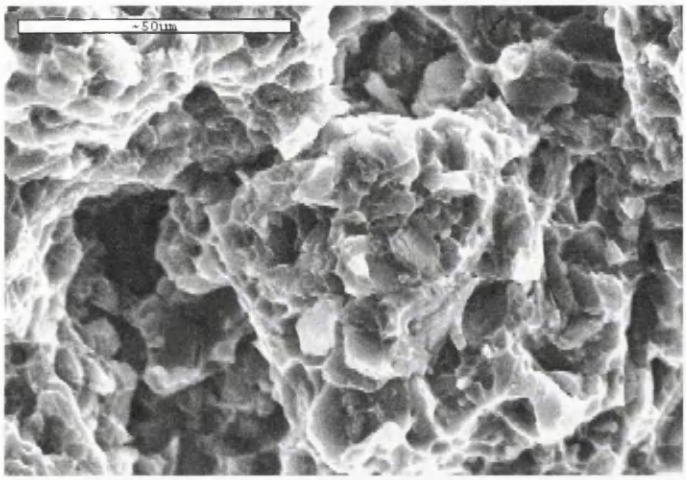

Figure 81. 5mm from the initiation pit into the fatigue crack surface. Smaller dimples are evident.

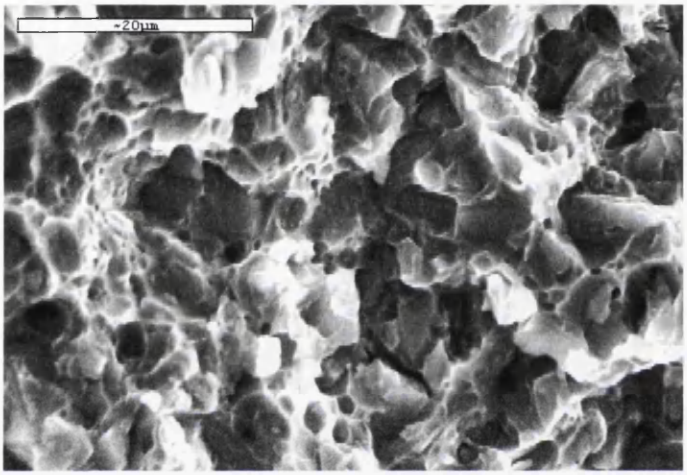

Figure 82. Over load region. Here there is a marked prevalence of debonding as opposed to partical cracking. The dimples of the ductile fracture mode are smaller and more prolific in this region.

Part 6. Conclusions.

1. Tensile strength is increased substantially by a T4 heat treatment, and the AMC225Xe T4 material has the highest tensile strength of the materials tested. The elastic modulus of the material is more dependent on alloy type than heat treatment.
2. Pits form, some rapidly deepening, when the material is exposed to 3.5% NaCl solution. A maximum pit depth was recorded after a 12 hour exposure. Pit depth is self limiting due to the build up of corrosion products at the pit mouth. Longer exposure times produce more initiated pits with the frequency of deep pits rising.

   Copper, manganese and magnesium concentration was found to vary throughout the matrix material. It is speculated that this leads to electrolytic cell formation and to preferential corrosive attack.

   In agreement with work by Imeson and Bartlett[100], an increased magnesium content in the initiation region, together with a lower than average matrix Mg content is associated with pit initiation. In addition, the initiation region is deficient in copper and, to a lesser extent, manganese. Further research is required to determine which of these elements is of major importance in the initiation process.

   It was noted that silicon carbide was not evenly distributed throughout the matrix material. Grouping/clumping of the particulate reinforcement was recorded, particularly in the blended mix process.

   Preferential corrosive attack occurs in the extrusion direction of the matrix material
3. Under ambient lab conditions, the T4 heat treated material has a greater fatigue resistance than the respective untreated (T1) condition alloys.

The blended material has higher fatigue resistance than the mechanically alloyed material when tested in air. It is speculated that this is due to the more even distribution of silicon carbide particles.

4. On the introduction of samples to a salt atmosphere (solution or fog), pits create fatigue intolerant defects and a consequent shortening of fatigue life in all cases. Upon immersion in saline solution the majority of life reduction occurred in the first 12 hours, while first deep pitting takes place.

   The fatigue responses of the blended and mechanically alloyed materials are found to be comparable. Hence, any increase in fatigue resistance conferred by production methods is lost.

5. Stress range variation (R ratios of 0.1 and 0.5) and waveform frequency (in the range 0.1 to 10 Hz) has no evident influence on LCF response in a fog atmosphere, although further investigation is required in this area.

6. All of the materials examined were found to behave in a similar manner when tested in a salt fog atmosphere.

   A "microstructurally long crack" trend has been defined for $\Delta K > 8MNm^{-3/2}$ which is independent of the alloys evaluated, heat treatment or environment.

Part 7. Further Work.

Composite materials used in industry are subjected to a 1.5% strain in order to straighten heat treated material. The effect of this straightening process has not been addressed by this project.

Further work into pit initiation is required. The exact location of pit initiation has not been identified. Research into the miro-constituents, precipitate composition and location and the electrochemical processes involved, is necessary to do this. Further, it is important to establish the precise relationship between the stress concentration and the stress intensity approaches to fatigue prediction in corrosive environments.

Corner crack specimens may not be the most sensitive test piece design for characterising short crack growth in such fine grained alloys. Further research on short crack effects and the influence of environment on them, may be necessary to allow accurate defect tolerant calculations.

Part 8. References.

1) Ed: Ken L. Reifsnider,
Composite Materials Series, Vol. 4, 1991

2) R. L. Trumper,
Metals and Materials, November, pp. 662-667, 1987.

3) O. H. Basquin,
Proc. A. S. T. M. 10, pp. 625-630, 1910.

4) T. G. Nieh and R. F. Karlak,
Journal of Materials Science, Letters 2, pp. 119-122, 1983.

5) Concice Encyclopedia of Composite Materials.
Ed: Anthony Kelly, Pub. Pergamon Press, 1994.

6) Minoru Taya and Richard J. Arsenault,
Pergamon Press. pp. 136, 1989.

7) Y. Zong and B. Derby,
Journal de Physique IV, Volume 3, Chapter 7, pp 1861-1866, 1993.

8) Ali Cansun and Ahmet Aran,
Materials Science Forum, vols. 217-222, Part 2, pp. 1115-1120, 1996.

9) H. M. Ledbetter and M. W. Austin,
Materials Science and Engineering, 89, pp. 53-61, 1987.

10) K. A. Lucas and H. Clarke,
Pub. Research Studies Press Ltd, 1993.

11) Jae-Chul Lee, Ji-Yuong Byun, Chang-Seok Oh, Hyun-Kwang Seok and Ho-In Lee,
Acta Materialia, vol. 45, No. 12, pp. 5303-5315, 1997.

12) Safak Yilmaz and Ahmet Aran,
Materials Science Forum, vols. 217-222, Part 2, pp. 1121-1126, 1996.

13) Keesham Shin, Dongsup Chung and Sunghak Lee,
Metallurgical and Materials Transactions A, Vol. 28A, pp. 2625-2636, Dec. 1997.

14) P. K. Rohatgi, R. Asthana and F. Yarandi,
Solidification of MMC's, Ed: Pradeep Rohatgi, pp.51-57, 1990.

15) Hongquing Xu, E. J. Palmier,
Materials Science Forum, vols. 217-222, Part 2, pp. 1091-1096, 1996.

16) T. S. Srivatsan, T. S. Sudarshan and E. J. Lavernia,
Progress in Materials Science, Vol. 39, pp. 317-409, 1995.

17) B. Tomkins and W. D. Biggs,
Journal of Materials Science, 4, pp. 532-538, 1969.

18) R. J. Arsenault, N. Shi, C. R. Feng and L. Wang,
Materials Science and Engineering, A131, pp. 55-68, 1991.

19) C. D. Beachem,
Trans. ASM, vol. 56, pp. 318-326, 1963.

20) M. Gensamer,
Transactions of the American Society of Metals, pp. 30-60, 1945,

21) S. M. Pickard, B. Derby, J. Harding and M. Taya,
Scripta Metallurgica, vol. 22, pp. 601-606, 1988.

22) Joseph Gurland,
Composite Materials, Vol. 5, Fracture and Fatigue, pp. 45-50, 1974.

23) A. J. Birkle, R. P. Wei and G. E. Pellissier,
Trans. ASM, vol. 59, pp981-990, 1966.

24) D. L. Davidson,
Metallurgical Transactions A, vol. 18A, pp. 2115-2128, 1987.

25) John K. Tien, Anthony W. Thompson, I. M. Bernstein and Rebecca J. Richards,
Metallurgical Transactions A, vol. 7A, pp. 821-829, June 1976.

26) S. H. Goods and L. M. Brown,
Acta Metallurgica, vol. 27, pp. 1-15, 1979.

27) J. LLorca, A. Needleman and S. Suresh,
Acta Metallic et Materialia, vol. 39, No. 10, pp. 2317-2335, 1991.

28) P. B. Pragnell, T. Downes, P. J. Withers and W. M. Stobbs,
Acta Metallic et Materialia, vol. 42, No. 10, pp. 3437-3442, 1994.

29) J. Llorca, A. Martin, J. Ruiz and M. Elices,
Metallurgical Transactions A, vol. 24A. pp. 1575-1588, 1993.

30) D. J. Lloyd,
Acta Metallurgica et Materialia, vol. 39, No. 1, pp. 59-71, 1991.

31) Zhirui Wang, Tzi-Kang Chan and D. J. Lloyd,
Metallurgical Transactions A, vol. 24A. pp. 197-207, 1993.

32) Y. Flom and J. Arsenault,
Acta Metallica, vol. 37, No. 9, pp. 2413-2423, 1989.

33) M. Manoharan and J. J. Lewandowski,
Acta Metallica et Materialia, vol. 38, No. 3, pp. 489-496, 1990.

34) M. E. Fitzpatric, M. T. Hutchings and P. J. Withers,
Acta Materialia, vol. 45, number 12, dec. 1997.

35) J. Llorca, S. Suresh, and A. Needleman,
Metallurgical Transactions A, Volume 23A, pp. 919-934, March 1992.

36) U. Lindborg,
Acta Metallurgica, vol. 17, pp. 521-526, 1969.

37) W. W. Gerberich,
Trans. ASM, vol. 59, pp. 899-908, 1966.

38) B. I. Edelson ans W. M. Baldwin, Jr.,
Trans ASM, vol. 55, pp. 231-250, 1962.

39) D. O. Swenson and C. A. Rau, Jr.,
Int. J. Fracture Mech., 6, pp. 357-365, 1970.

40) Robert K. Leverenz,
Int. J. Fracture Mech., 8, pp. 311-324, 1972.

41) J. R. Hancock,
Composite Materials, vol. 5, pp. 371-414, 1974.

42) D. G. Harlow and S. L. Phoenix,
International Journal of Fracture, Vol. 17, pp347-372, 1981.

43) J. M. Papazian and P. N. Adler,
Metallurgical Transactions A, vol. 21A, pp. 401-410, 1990.

44) K. S. S. Aradhya and M. K. Surappa,
Script Metallurgica et Matrialia, vol. 25, pp 817-822, 1991.

45) Irina Severin and Gheorghe Zgura,
Materials Science Forum, vols. 217-222, Part 2, pp. 1097-1102, 1996.

46) D. W. A. Rees,
Composites A, 29A, pp. 171-182, 1998.

47) Jody N. Hall, J. Wayne Jones and Anil K. Sachdev,
Materials Science and Engineering, vol. 83, pp. 69-80, 1994.

48) Nakai Manabu and Takehiko Eto,
Materials Science Forum, vols. 217-222, Part 3, pp. 1517-1522, 1996.

49) F. J. Humphreys, W. S. Miller and M. R. Djazeb,
Materials Science and Technology, vol. 6, pp.1157-1166, 1990.

50) F. J. Humphreys,
Materials Science and Engineering, A135, pp. 267-273, 1991.

51) I. Dutta and B. S. Mujumdar,
Materials Science Forum, vols. 217-222, Part 3, pp. 1473-1478, 1996.

52) V. C. Nardone and K. M. Prewo,
Scripta Metallurgica, vol. 20, pp. 43-48, 1986.

53) I. A. Ibrahim, F. A. Mohamed and E. J. Lavernia,
Journal of Materials Science, vol. 26, pp. 1137-1156, 1991.

54) I. Sinclair and P. J. Gregson,
Materials Science and Technology, Vol. 13, pp. 709-726, Sept. 1997.

55) L. C. Davis and J. E. Allison,
Metallurgical Transactiona A, vol. 24A, pp. 2487-2496.

56) Li Shouxin, Sun Lizhi and Wang Zhongguang,
Scripta Metallurgica et Materialia, vol. 25, pp. 2431-2434, 1991.

57) P. B. Pragnell, T. Downes, W. M. Stobbs and P. J. Withers,
Acta Metallic et Materialia, vol. 42, No. 10, pp. 3425-3436, 1994.

58) O. P. Arora and M. Metzger,
Trans. A.I.M.E., 236, pp. 1205 , 1966.

59) T. Christman and S. Suresh,
Acta Metallica, Volume 36, No 7, pp 1691-1704, 1988.

60) L. M. Styles, I. Sinclair, P. G. Gregson and S. M. Flitcroft,
Materials Science and Technology, vol. 10, pp. 475-480, 1994.

61) T. S. Srivatsan, T. S. Sudarshan and E. J. Lavernia,
Progess in Materials Science, vol. 39, pp. 317-409, 1995.

62) M. A. Bayoumi, H. Ribes and M. Suery,
Conference Proceedings, Mechanical and Physical Behaviour of Metalic and Ceramic Composites, Rosklide, Denmark, pp 291-296, September 1988.

63) A. J. Shakesheff,
Journal of Materials Science 30, pp. 2269-2276, 1995.

64) T. J. Downes and J. E, King,
Composites, Vol. 24, No. 3, pp. 276-281, 1993.

65) B. Y. Lou and J. C. Huang,
Materials Science Forum, vols. 217-222, Part 2, pp. 1103-1108, 1996.

66) T. G. Nieh, C. A. Henshall and J. Wadsworth.
Scripta Metallurgica, vol. 18, pp. 1405-1408, 1984.

67) T. G. Nieh, J. Wadsworth and T. Imai,
Scripta Metallurgica et Materialia, vol. 26, pp. 703-708, 1992.

68) K. Matsuki, H. Kawakami, M. Tokizawa, Y. Murakami and S. Murakami,
Materials Science Forum, vols. 217-222, pp. 1163-1168, 1996.

69) J. Llorca,
Theoretical Concepts and Numerical Analysis of Fatigue, pp. 523-539.

70) S. Suresh,
Pub Cambridge University Press, 1991.

71) M. R. Bache, W. J. Evans and G. Rees,
Proc. Int. Symp. Air Breathing Engines, Melbourne, Australia, 1995.

72) Ze Wen Huang, Ian R. McColl and Samuel J. Harris,
Materials Science and Engineering, A125, pp. 67-72, 1996.

73) D. N. Lal and V. Weiss,
Metallurgical Transactions A, Vol. 9A, pp. 423-425, March 1978.

74) Ed. Ken L. Reifsnider,
Composite Materials Series, vol. 4, 1991.

75) T. S. Srivastan and T. S. Sudarshan,
J. of Materials Science, vol. 23, pp. 1521-1533, 1988.

76) A. Plumtree and A. Varvani-Farahani,
Materials Science Forum, vols. 217-222, Part 3, pp. 1377-1382, 1996.

77) S. Pearson,
Engineering Fracture Mechanics, vol. 7, pp. 235-247, 1975.

78) K. Tanaka, T. Hoshide and O. Maekawa,
Engineering Fracture Mechanics, vol. 16, No. 2, pp. 207-220, 1982.

79) C. Laird and D. J. Duquette,
Localised Corrosion, N. A. C. E.- 3, pp. 88-117, 1971.

80) D. A. Lukasak and D. A. Koss,
Composites, Volume 24, No3, pp. 262-269,1993.

81) Zhirui Wang and Ruby J. Zhang,
Acta Metallica Materials, Volume 42, No 4, pp. 1433-1445, 1994.

82) D. L. Davidson,
Composites, Vol. 24, No. 3, pp. 248-255, 1993.

82) J. J. bonnen, J. E. Allison and J. W. Jones,
Metallurgical Transactions A, vol. 22A, pp. 1007-1019, 1991.

84) Chang Gil Lee, Dongil Kwon and Sunghak Lee,
Metallurgical and Materials Transactions A, vol. 28A, pp. 2162-2170, 1997.

85) J. C. Healy and C. J. Beevers,
Conference on Mechanical Behaviour of Materials 6, vol. 4, pp. 101-106, 1992.

86) D. L. Corn,
Engineering Fracture Mechanics, vol. 3, pp. 45-52, 1971.

87) Hiroyuki Toda and Toshiro Kobayashi,
Metallurgical and Materials Transactions A, Vol. 28A, pp. 2149-2157, Oct. 1997.

88) C. Bathias,
Materials Science Forum, vols. 217-222, Part 3, pp. 1407-1412, 1996.

89) R. J. H. Wanhill,
Int. J. Fatigue, vol. 16, pp. 99-110, 1994.

90) J. J. Bonnen, J. E. Allison and J. W. Jones,
Metallugical Transactions A, vol. 22A, pp. 1007-1019, 1991.

91) J. B. Johnson and T. T. Oberg,
Proc. ASTM, vol. 29, part 2, Technical Papers, pp. 339-352.

92) B. Thomkins and W. D. Biggs,
Journal of Materials Science, vol. 4, pp. 532-538, 1969.

93) T. Christman and S. Suresh,
Materials Science and Engineering, A102, pp 211-216, 1989.

94) J. K. Shang and R. O. Ritchie,
Acta Metallurgica, 37, pp 2267-2278, 1989.

95) E. Hochrieter, M, Panzenbock, and F. Jeglitsch,
International Journal of Fatigue, No 6, pp. 493-499, 1993.

96) K. R. Trethwey and J. Chamberlain,
Pub. Longman Scientific and Technical, 1988.

97) Y. V. V. R. S. Murty, T. Z. Kattamis and O. F. Devereux,
N. A. C. E. Corrosion, vol. 31, No. 6, pp. 207-208, 1975.

98) P. R. Roberge,
Materials Science Forum, vols. 217-222, Part 3, pp. 1581-1586, 1996.

99) J. Y. Barghout, G. W. Lorimer, R. Pilkington, P. B. Pragnell,
Materials Science Forum, vols. 217-222, Part 2, pp. 975-980, 1996.

100) D. Imeson and D. I. Bartlett,
Journal of Microscopy, vol. 177, part 3, pp. 347-356, March 1995.

101) P. P. Trzaskoma, E. McCafferty and C. R. Crowe,
Journal of the Electrochem. Soc., vol. 130, pp 1804-1809, 1983.

102) Denise M. Aylor and Patrick J. Moran,
Journal of the electrochem. Soc., vol. 132, pp. 1277-1281, 1985.

103) Dr. S. C. Sharma. G. S. K. Rao, M. Nagarajan, B. M. Girish and Rathnakar Kamath,
Materials Science Forum, vols. 217-222, Part 3, pp. 1577-1580, 1996.

104) Dr. S. C. Sharma, G. S. K. Rao, M. Nagarajan, B. M. Girish and Rathnakar Kamath,
Materials science forum, vols. 217-222, pp. 1577-1580, 1996.

105) L. Pinto and E. Zschech,
Materials Science Forum, vols. 217-222, pp. 1593-1598, 1996.

106) S. J. Harris, B. Noble and A. J. Trowsdale,
Materials Science Forum, vols. 217-222, Part 3, pp. 171-1576, 1996.

107) Ch. Blanc, B. Lavelle and G. Mankowski,
Materials Science Forum, vols. 217-222, Part 3, pp. 1559-1564, 1996.

108) H. Bohni and, H. H. Uhlig,
Journal of the Electrochem. Soc., vol. 116, No. 7, pp. 907-910, 1969.

109) A. V. Karlashov, A. D. Gnatyouk and, A. B. Kardash,
Proc. first USSR-UK Seminar of Corrosion Fatigue of Metals. Lvov, USSR,
pp. 101-111, May 1980.

110) P. Lancombe and N. Yannaquis,
Rev. Met., vol. 45, p. 68, 1948.

111) J. Y. Boos and C. Goux,
Localised Corrosion, N. A. C. E.- 3, pp. 556-567, 1971.

112) B. Roald and M. A. Striecher,
J. Electrochem. Soc., vol. 97, p. 283, 1950.

113) R. J. Galvele and S. M. DeMicheli,
Corrosion Science, vol. 10, pp. 795-807, 1970.

114) G. H. Koch,
NACE, vol. 35, No. 2, pp. 73-78, Feb. 1979.

115) John K. Tien, Rebecca J. Richards, Otto Buck and Harris L. Marcus,
Scripta Metallurgica, vol. 9, pp. 1097-1101, 1975.

116) G. C. Wood, W. H. Sutton, J. A. Richardson, T. N. K. Riley and A. G. Malherbe,
Localised Corrosion, N. A. C. E.-3, pp. 526-539, 1971.

117) S. Wernick, R. Pinner, P. G. Sheasby,
A. S. M. 5 Edition Volume 1, Chapter 5, pp 220-288, 1987.

118) Trung Hung Nguyen and R. T. Foley,
J. Electrochem. Soc., vol. 126, No. 11, pp. 1855-1860, 1979.

119) K. Nisancioglu and H. Holtan,
Corrosion Science, vol. 18, pp. 835-849, 1978.

120) B. F. Brown, J, Kruger and R. W. Staehle,
Localised Corrosion, N. A. C. E.- 3, pp. 580-599, 1971.

121) V. I. Pokhmurskii,
Proc. first USSR-UK Seminar of Corrosion Fatigue of Metals. Lvov, USSR, pp. 47-53, May 1980.

122) A. I. Asphahani and W. L. Silence,
Metals Handbook, A. S. M. 9 Edition, pp. 113-114.

123) G. E. Thompson, P. E. Doherty and G. C. Wood,
Journal of the Electrochemical Society, No 129, pp 1515-1517, 1982.

124) P. P. Trzaskoma,
Corrosion, vol. 46, No. 5, pp. 403-409, 1990.

125) Bogulow Mazurkiewicz and Antoni Piotrowski,
Corrosion Science, vol. 23, No. 7. pp. 697-707, 1983.

126) P. P. Trzaskoma and E. McCafferty,
Journal of the Electrochemical Society, Volume 130, pp. 1804-1809, 1983.

127) J. H. Payer and R. W. Staehle,
Corrosion Fatigue, N. A. C. E. -2, pp. 211-269

128) Donald O. Sprowls,
Metals Handbook, A. S. M. 9 Edition, pp 131-132.

129) Markus O. Speidel,
Metallurgical Transactions A, vol. 6A, pp. 631-651, April 1975.

130) U. R. Evans,
Corrosion, N. A. C. E. 7, Volume 7, pp. 238-244, 1951.

131) J. F. Knott
Proc. first USSR-UK Seminar of Corrosion Fatigue of Metals. Lvov, USSR, pp. 9-23, May 1980.

132) R. Hermann,
N. A. C. E. Corrosion, vol. 44, No. 10, pp. 685-690, 1988.

133) R. J. Gest and A. R. Troiano,
N. A. C. E. Corrosion, vol. 30, No. 8, pp. 274-279, 1974.

134) M. J. Robinson,
Corrosion Science, vol. 23, No. 8, pp. 887-899, 1983.

135) I. A. Stepanov and A. G. Salomashenko,
Proc. first USSR-UK Seminar of Corrosion Fatigue of Metals. Lvov, USSR,
pp. 113-120, May 1980.

136) N. J. H. Holroyd and D. Hardie,
Corrosion Science, vol. 23, No. 6, pp. 527-546, 1983.

137) H. J. Gough, M.B.E., DSc., PhD., Member,
The Journal of the Institute of Metals, vol. 49, No. 2, Autumn Lecture, 1932.

138) F. N. Speller, I. B. McCorkle and P. F. Mumma,
Proc. ASTM, vol. 28, part 2, Technical Papers, pp. 238-249, 1928.

139) D. J. McAdam Jr.,
Proc. A. S. T. M., vol. 29, pp. 250-313, 1929.

140) Kasuaki Shiozawa and Shuming Sun,
Metallurgical and Materials Transactions A, Vol. 28A, pp. 1471-1477, July 1997.

141) I. Trockels, G. Lutering and A. Gysler,
Materials Science Forum, vols. 217-222, Part 3, pp. 1599-1604, 1996.

142) V. V. Panasyuk and O. N. Romaniv,
Proc. first USSR-UK Seminar of Corrosion Fatigue of Metals. Lvov, USSR, pp. 24-35,
May 1980.

143) T. Pyle, V. Rollins and D. Howard,
Corrosion Fatigue, N. A. C. E.- 2, pp. 312-318, 1971.

144) H. H. Uhlig,
Corrosion Fatigue, N. A. C. E.- 2, pp. 270-278, 1971.

145) B. P. Haigh and B. Jones,
Journal of the Institute of Metals, vol. 43, pp. 271-281, 1930.

146) E. M. Radetskaya,
Proc. first USSR-UK Seminar of Corrosion Fatigue of Metals. Lvov, USSR,
pp. 121-125, May 1980.

147) R. N. Parkins, "Corrosion Fatigue",
Proc. first USSR-UK Seminar of Corrosion Fatigue of Metals. Lvov, USSR,
pp. 36-46, May 1980.

148) D. O. Sprowls,
Metals Handbook, 9th Edition, pub. A. S. M. 13, pp. 291-302.

149) D. J. Duquette,
E. I. C. M. Proceedings, pp 45-53.

150) W. J. Evans and Z. Lu,
To be published: Engineering Fracture Mechanics.

151) M. O. Speidel, M. J. Blackburn, T. R. Beck and J. A. Feeny,
Corrosion Fatigue, N. A. C. E.- 2, pp. 324-345, 1971.

152) R. P. Wei and G. W. Simmons,
International Journal of Fracture, Vol. 17, pp. 235-247, 1981.

153) J. M. Barsom,
International Journal of Fracture Mechanics, vol. 7, No. 2, pp.163-182, June 1971.

154) D. A. Meyn,
Metallurgical Transactions, vol. 2, pp. 853-865, 1971.

155) H. L. Marcus, J. C. Williams and N. E. Paton,
Corrosion Fatigue, N. A. C. E.- 2, pp. 346-358, 1971.

156) R. P. Gangloff,
E. I. C. M Proceedings, pp. 55-109.

157) N. J. H. Holroyd.
E. I. C. M. Proceedings, pp 311-345.

158) Robert P. Wei and Richard P. Gangloff,
Fracture Mechanics, Twentieth Symposium, pp. 233-264.

159) C. E. Jaske, J. H. Payer and V. S. Balint,
Battelle Press, 1981.

160) Francis L. Laque,
Pub., John Wiley and Sons, 1975.

161) P. Scott and R. A. Cottis,
Mechanical Engineering Publications Ltd., (M. E. P.), 1990.

162) D. O. Sprowls,
A. S. M. Metals Handbook 13, pp 291-302, 1987.

163) T. S. Srivatsan and T. S. Sudarshan,
Journal of Materials Science, Volume 23, pp 1521-1533, 1988.

164) H. S. Rawdon,
Proc. ASTM. vol. 29, Part 2, Technical Papers, pp. 314-338, 1929.

165) B. Roebuck,
Test Techniques for MMC'c II, Conference proceedings, pp. 23-50, 1992.

166) J. C. Healy and C. J. Beavers,
Conference on the Mechanical Behaviour of Materials VI, Volume 4,
pp 101-106, 1992.

167) Corrosion Testing Procedures - Lab Exposure Conditions,
A.S.T.M. B. 287-74, pp. 85-95, Reapproved 1980.

168) Standard Method of Salt Spray (Fog) Testing,
A.S.T.M. B. 117-73, pp. 95-101, Reapproved 1979.

169) Fracture and Fatigue,
Ed. C. J. Beavers, Chameleon Press, 1980.

170) N. Knee,
The Effect of Microstructure on Fatigue and Crack Growth, Parthenon Press, 1986.

171) D. Walton and E. G. Ellison,
International Metals Review, Volume 17, p. 100, 1972.

172) W. J. Plumbridge and D. A. Ryder,
International Metals Review, Volume 14, p. 119, 1969.

173) C. Laird,
Fatigue Crack Propagation, A. S. T. M. S.T.P. 415, A. S. T. M. Phil., P. A.
p. 139, 1967.

174) C. Laird and G. C. Smith,
Phil. Mag. 7, p. 824, 1962.

175) P. C. Paris and F. Erdogan,
Trans A. S. M. E. Journal of basic Engineering, Vol 85, p. 528, 1963.

176) T. L. Anderson,
Fracture Mechanics, C. R. S. Press, p. 597, 1991.

177) H. L. Ewalds and R. J. H. Wanhill,
Fracture Mechanices, Edward Arnold and D. U. M. Press, 1984.

178) A. P. Parker,
The Mechanics of Fracture and Fatigue, E. and F. H. Spon Ltd., London 1981.

179) J. M. Kraft and W. H. Cullen, Jr.,
N. R. L. Memorandum Report, 2505, July 1977.

180) "Methods of Fatigue Testing",
BS3518:1993 part 1.

181) "Determination of the Rate of Fatigue Crack Growth in Metallic Materials."
BS6835 : 1998.

182) I. Yugur, Ph.D. Thesis,
University Wales, 1999.

183) W.J. Evans
Materials Science and Engineering A263, 160-175, 1999)

184) W.J. Evans, P.J. Nicholas and S.H. Spence,
Advances in Fatigue Lifetime Predictive Techniques, ASTM STP 1292;

M.R. Mitchell and R.W. Landgraf, Eds., ASTM, Phil., P.A. p.202, 1995.

185) R.P. Skelton,
'Fatigue Crack Growth' in 'Characterisation of high temperature materials'
Edited by I Curbishley, The Institutue of Metals, 1988, p.108-172.

Appendix 1.

Appendix 2.

Unless otherwise stated, LCF testing was carried out in air under a 1Hz sine waveform and R value of 0.1. Columns headed MPa represent peak stress applied. The columns headed Nf represent the number of cycles completed to failure. Where a "+" appears after a number, the sample has not been tested to failure and was stopped due to time constraints.

Results for AMC225Xe Material.

Xe-T4, tested in air at 1Hz sin, R=0.1

MPa	Nf
450	785597+
464	335942+
475	54080
500	46018
559	18033
575	15499
600	9542

Table 14.

Xe T4 material, tested in air, R=0.1, 1Hz sin.

Soak Time (hrs)	Peak Stress (MPa)	Cyles to Failure
4	350	349387
8	350	116535
12	350	18967
24	350	15064
72	350	17897
0	450	7895597+
8	450	6580
24	450	6626
72	450	4328

Table 15.

Xe-T4, 24 hour 3.5% NaCl pre-soak, tested in air at 1Hz sin, R=0.1

MPa	Nf
250	710590+
300	35313
350	15064
375	47624
450	6626

Table 16.

Xe-T4, tested in 3.5% NaCl fog atmosphere at 1Hz sin, R=0.1

MPa	Nf
250	181317
300	101024
350	24916
400	30411
450	12019
500	6838
575	4148

Table 17.

Xe-T1, tested in air at 1Hz sin, R=0.1

MPa	Nf
350	249200+
375	125904
400	87791
425	15129
450	12488
470	2078

Table 18.

Xe-T1, 24 hour 3.5% NaCl pre-soak, tested in air at 1Hz sin, R=0.1

MPa	Nf
350	54846
350	16931

Table 19.

Xe-T1, tested in 3.5% NaCl fog atmosphere at 1Hz sin, R=0.1

MPa	Nf
200	342538
250	136665
350	49290
400	25435
450	7385

Table 20.

Results from AMC225Xh Material.

Xh-T4, tested in air at 1Hz sin, R=0.1

MPa	Nf
425	298435
475	85263
500	32287
559	5332

Table 21.

Xh-T4, 24 hour 3.5% NaCl pre-soak, tested in air at 1Hz sin, R=0.1

MPa	Nf
350	101137
400	16805

Table 22.

Xh-T4, tested in 3.5% NaCl fog atmosphere at 1Hz sin, R=0.1

MPa	Nf
250	212816
250	36863
400	25783
450	9694

Table 23.

Xh-T1, tested in air at 1Hz sin, R=0.1

MPa	Nf
200	1275500+
250	1718900+
300	157979
350	56075

Table 24.

Xh-T1, 24 hour 3.5% NaCl pre-soak, tested in air at 1Hz sin, R=0.1

MPa	Nf
200	1302500+
250	1060230+
300	125482
325	19155
340	4698
350	6411

Table 25.

Results from AMC200 (base) Material.

200-T4, tested in air at 1Hz sin, R=0.1

MPa	Nf
250	1062700+
350	2465226+
400	334035+
450	25428
450	22350
500	11388

Table 26.

200-T4, tested in 3.5% NaCl fog atmosphere at 1Hz sin, R=0.1

MPa	Nf
250	131910
400	30359
450	9198

Table 27.

200-T1, tested in air at 1Hz sin, R=0.1

MPa	Nf
250	155476
275	151265

Table 28.

Frequency Effects.

Xe-T4, tested in air at 10Hz sin, R=0.1

MPa	Nf
300	75640
450	9315

Table 29.

Xe-T4, tested in air at 0.1Hz sin, R=0.1

MPa	Nf
300	54038
350	34617
400	10618
450	6721

Table 30.

R Value Effects.

Xe-T4, tested in fog at 1Hz sin, R=0.5

MPa	Nf
375	142000
425	47500
475	4500
600	5900

Table 31.

Appendix 3.

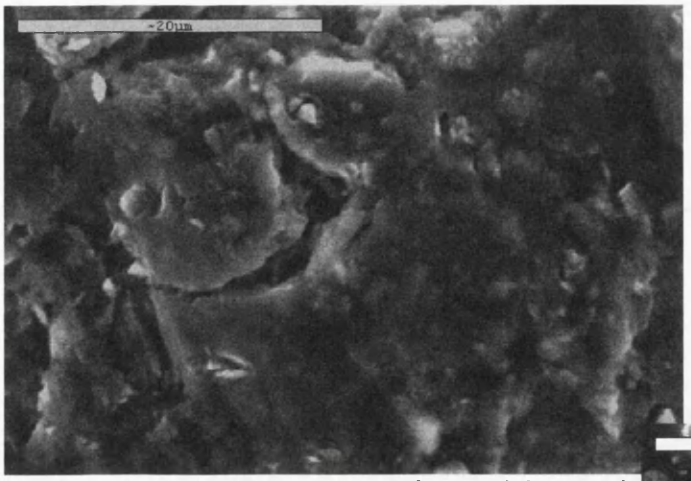

a) Area just behind initiation site of 24 hour presoak XH-T1 sample, peak stress 300MPa. The flat appearance of the fracture surface suggests a transgranular fracture mode, indicating corrosion fatigue failure. This may be due to some residual moisture in the base of the initiation pit.

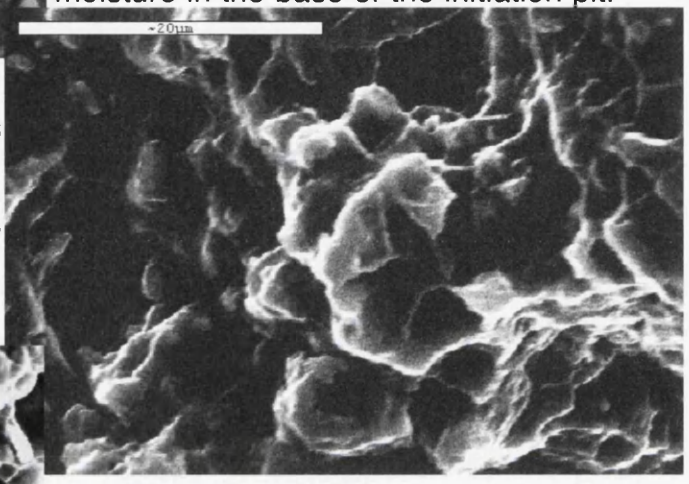

b) Area approx. 50 microns from a) in crack propagation direction. Here, the dimples form during fatigue cycling are large, indicating slow rupture or tearing. The features appear rounded due to corrosion product on the surface.

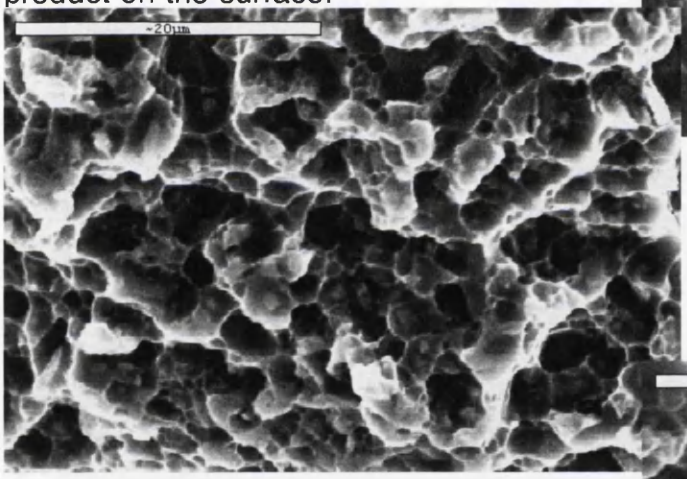

c) Stepped region of fatigue fracture surface. Here SiC particles can be seen in the bottm of the dimples which are smaller than in b), indicating faster crack growth.

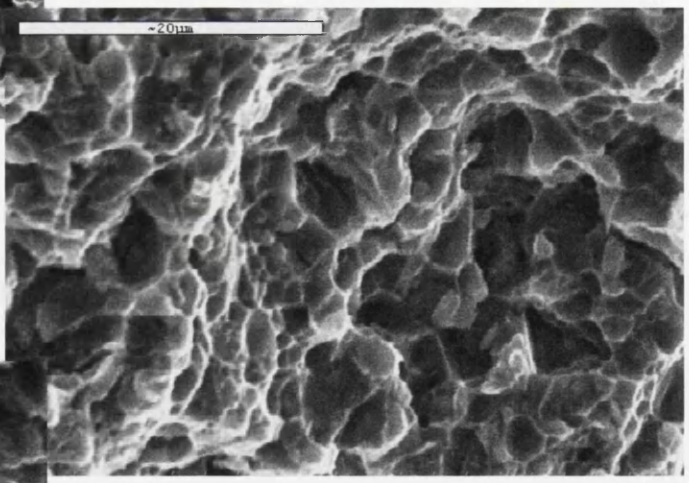

d) Fast growth region of fatigue fracture surface. Here there is a mixture of very small and slightly larger dimples.

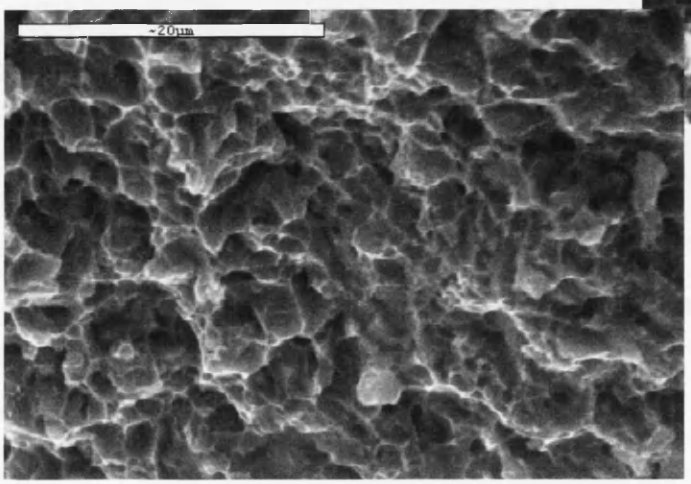

e) Overload region. Here the dimples are very small.

Dimple patterns seen in b)-e) are typical of all fracture surfaces examined.

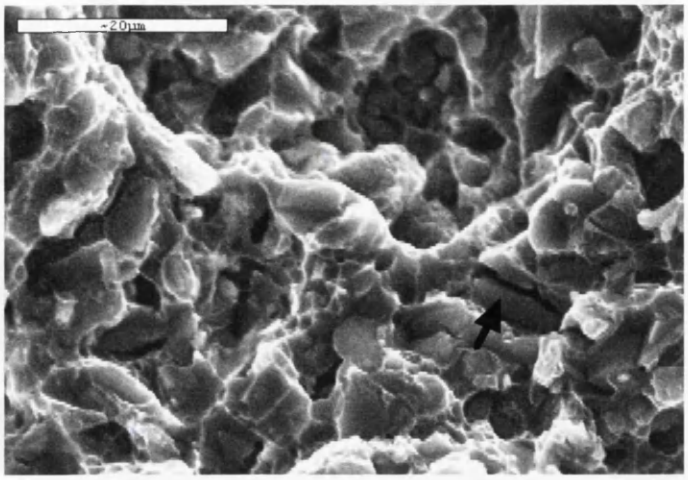

3mm into the fatigue crack surface, particle cracking (indicated by the arrow) is still very much in evidence, especially in the larger particles.

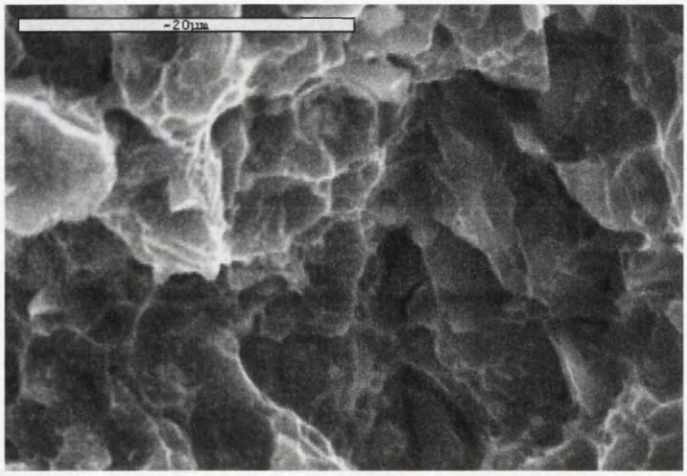

4mm into the fatigue crack surface, particle cracking is evident only in the large particles (greater than 5µm) with the prevalent crack advancement mode.being particle/matrix debonding

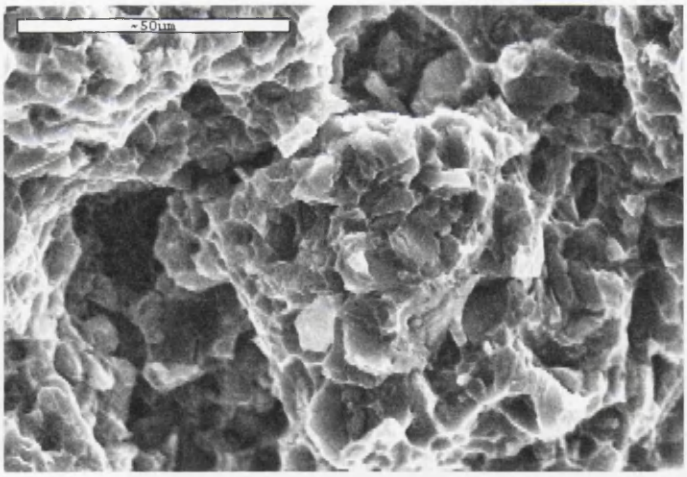

5mm from the initiation pit into the fatigue crack surface.

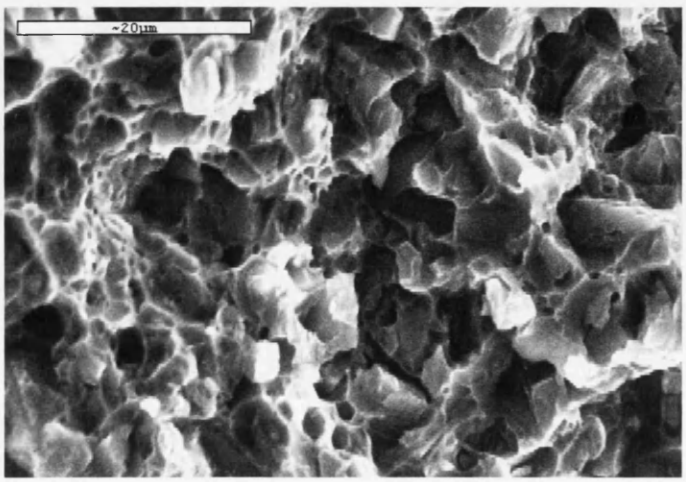

Over load region. Here there is a marked prevailance of debonding as opposed to partical cracking. The dimples of the ductile fracture mode are smaller and more prolific in this region.

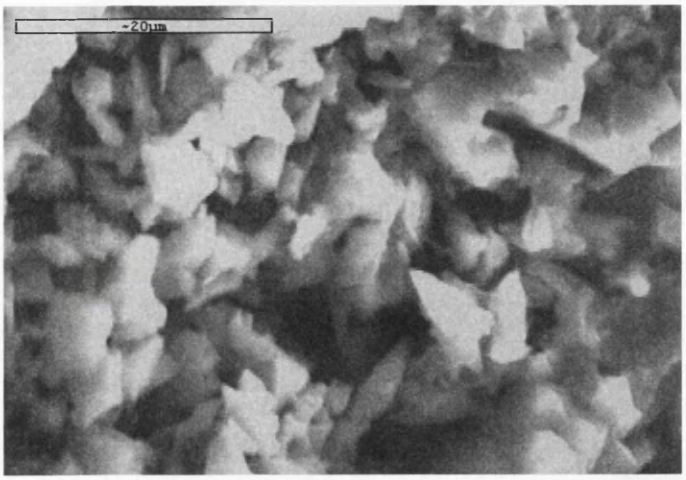

Taken from 90µm into the fracture surface from the initiation point in the propagation direction.

Taken from the surface of the guage length of the sample, approxomately 120µm from the initiation pit, showing initial erosion in the machining direction.

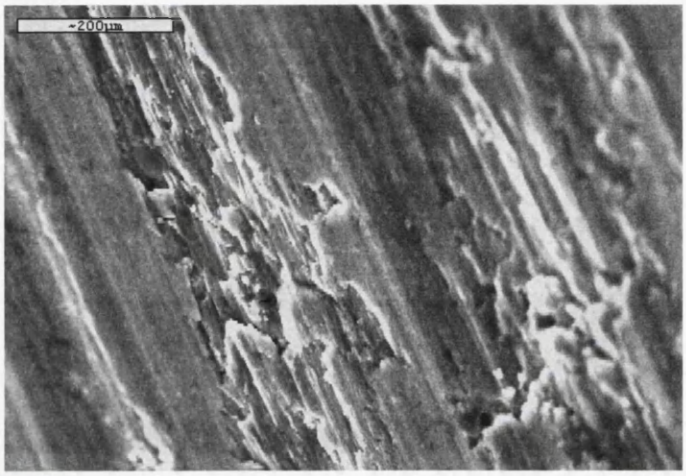

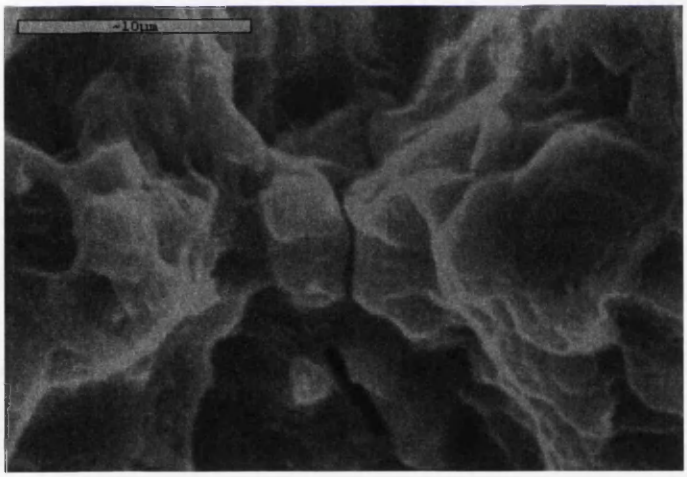

Taken from 1mm behind the initiation pit, this shows a microcrack running from the elongated hole at the bottom of the picture, all the way to the top of the frame. Also many small dimples are apparent.

Approximately 2mm in, the dimples have become more apparent. Particle cracking is mostly perpendicular to the direction of maximum stress, although a few were fractured parallel to the stress direction.

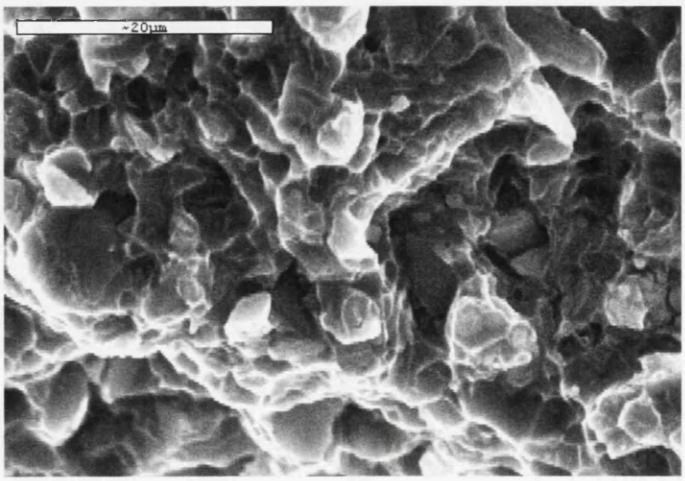

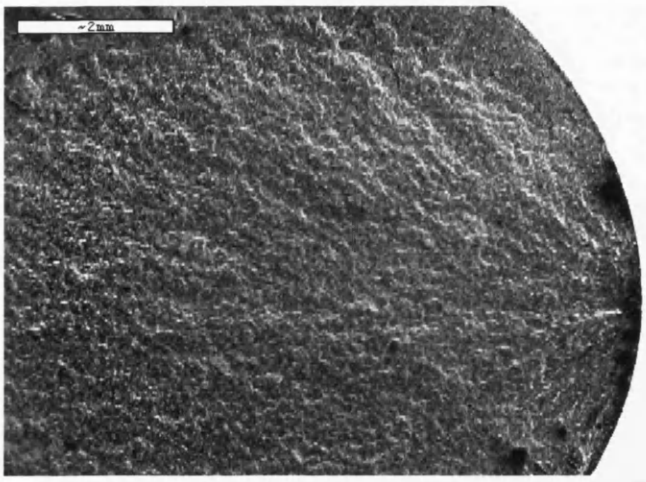

Picture to show the overall appearance of the fracture surface of an AMC225xh T4 heat treated sample, tested to failure in air.

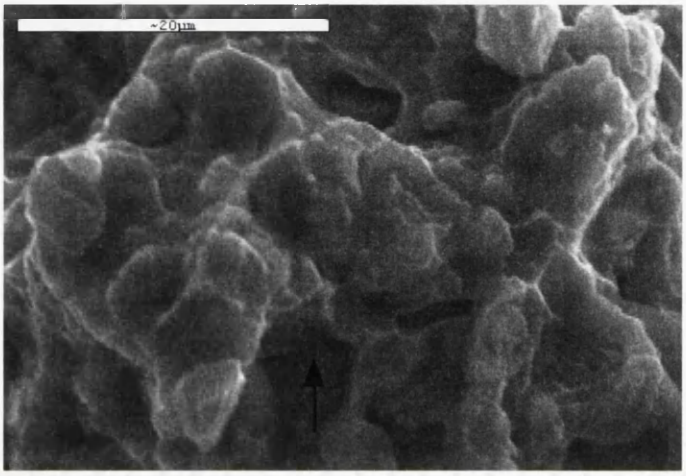

This picture shows the presence of a microcrack in the AMC225xh T1 sample, approximately 50μm from the initiation point.

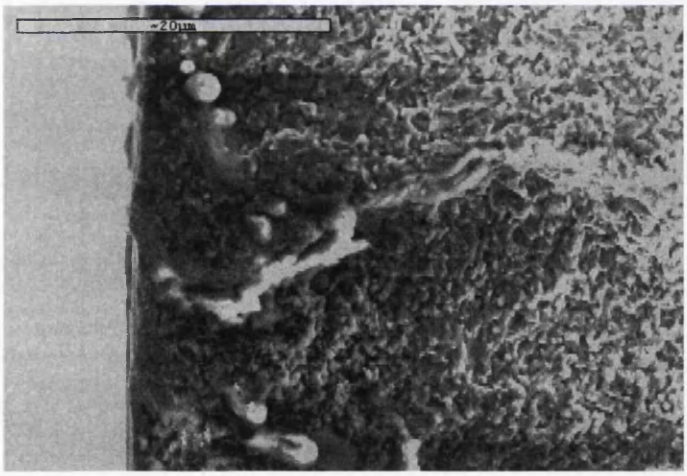

Photograph of the initiation piont, taken from a perpendicular angle to the fracture surface.

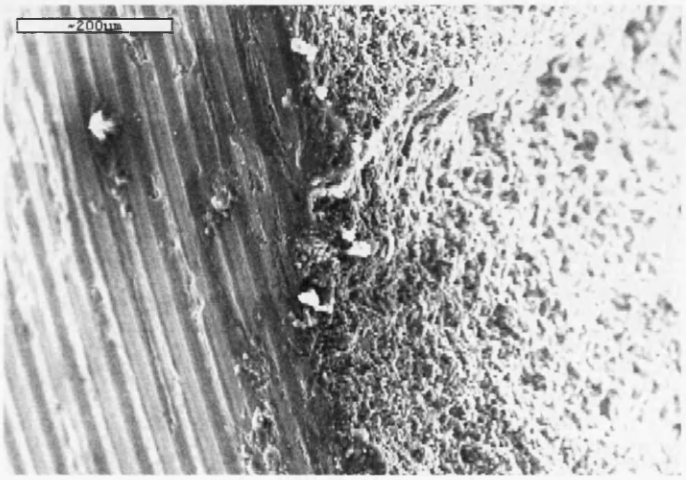

The initiation point taken from a 45^0 angle from the fracrue surface.

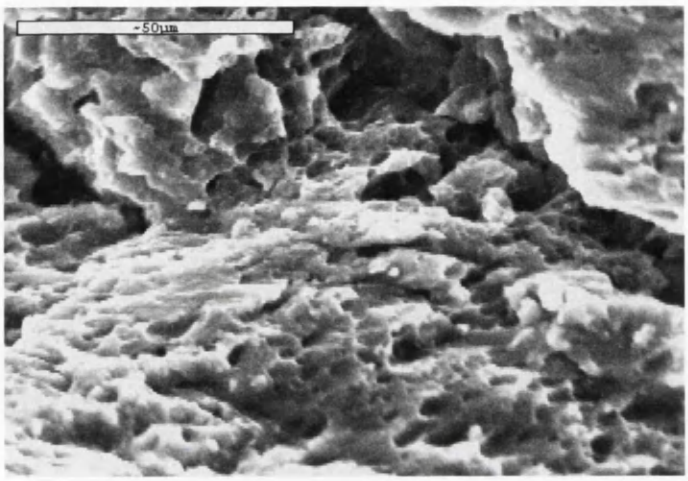

This picture shows shearing of a T1 heat treated base material sample tested after a 24 hour salt solution presoak at 275MPa. The direction of fatigue crack growth is from left to right of the picture. This picture was taken at the transition from fatigue cracking to overload.

Taken from the same sample. This shows a subsidiary fatigue crack, also initiated at a corrosion pit.

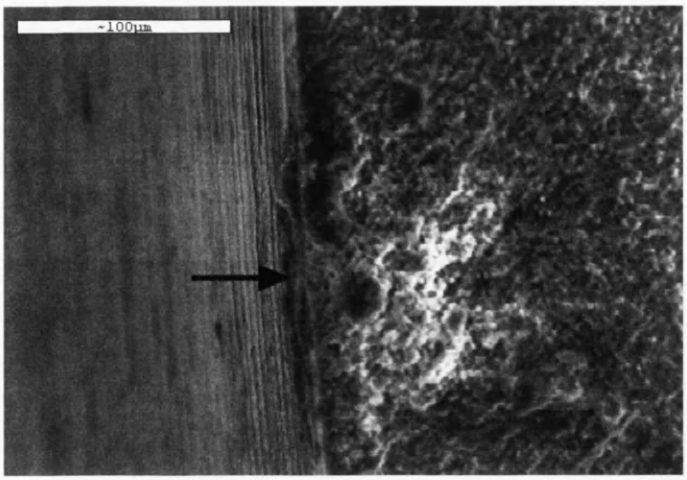

a) Initiation point on the fatigue surface of AMC225xh T4 heat treated material, fatigue tested in air at a maximum stress of 350MPa after a 24 hour soak in 3.5% NaCl solution.

b) Initiation site as a) at a 45° tilt, also showing the side of the specimen with corrosion/erosion in the machining direction as shown by the double headed arrow.

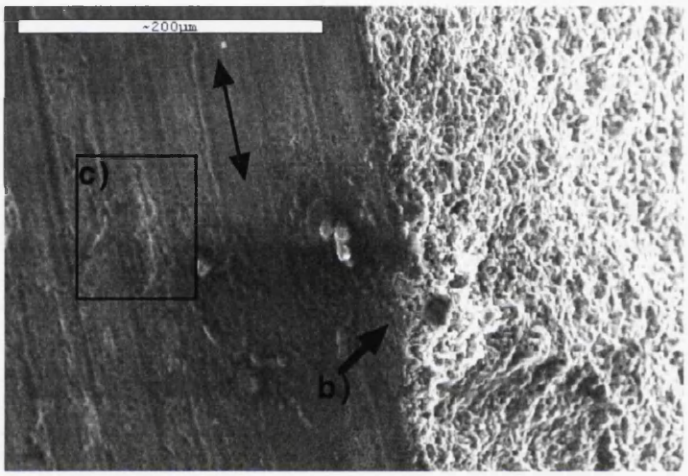

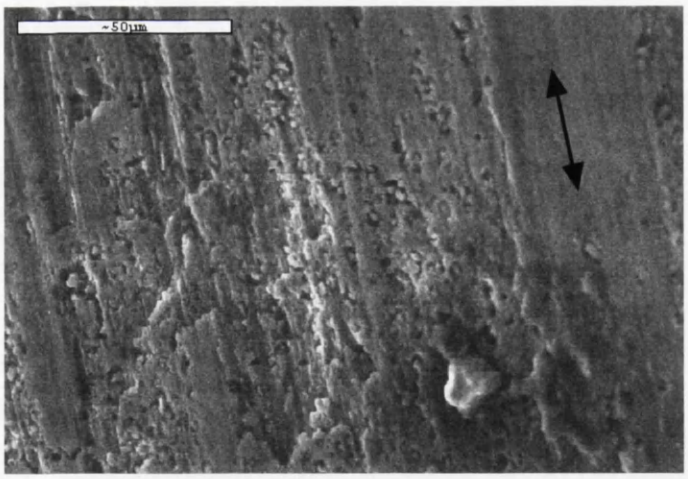

c) Enlargement of indicated area in b)

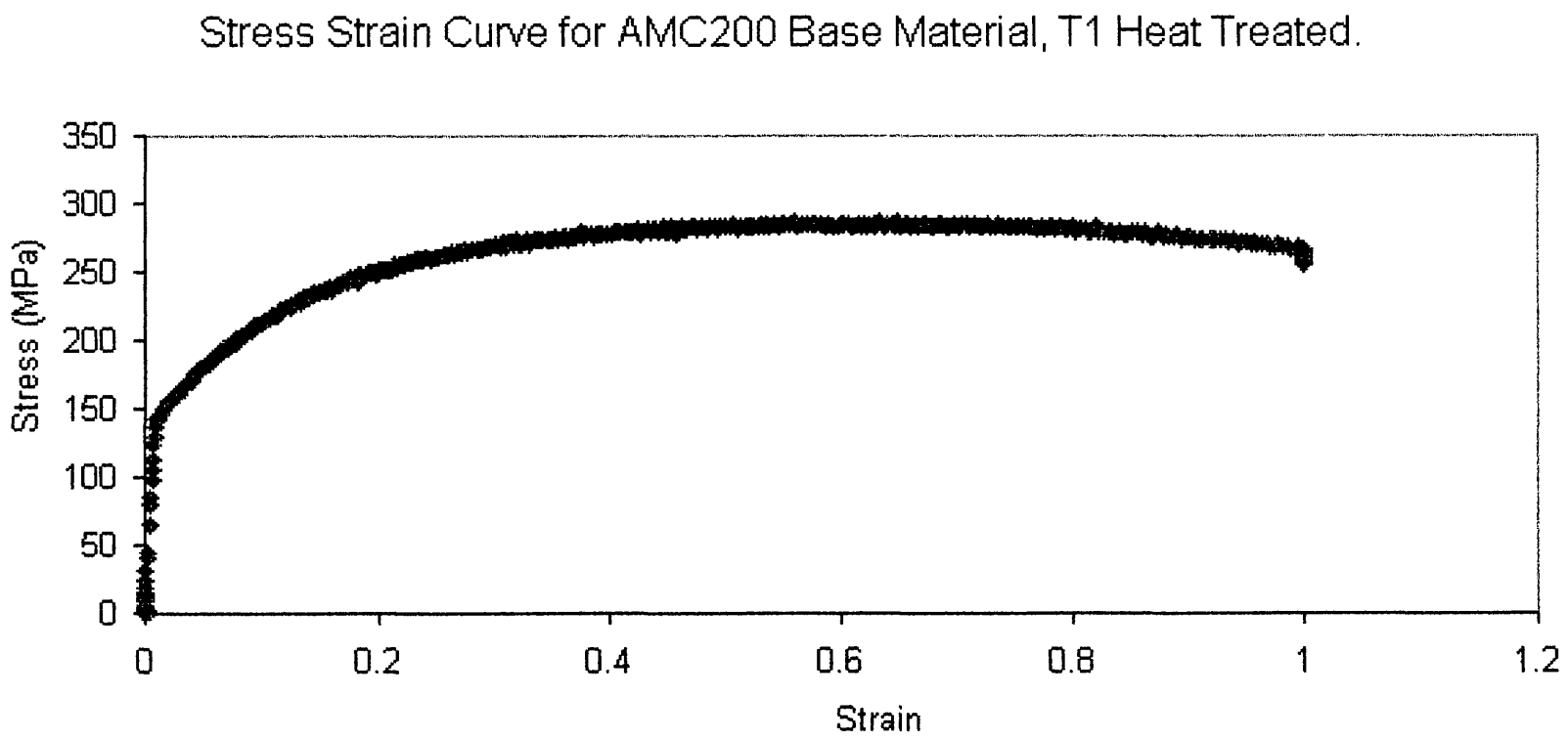

Appendix 1. Figure 1a.

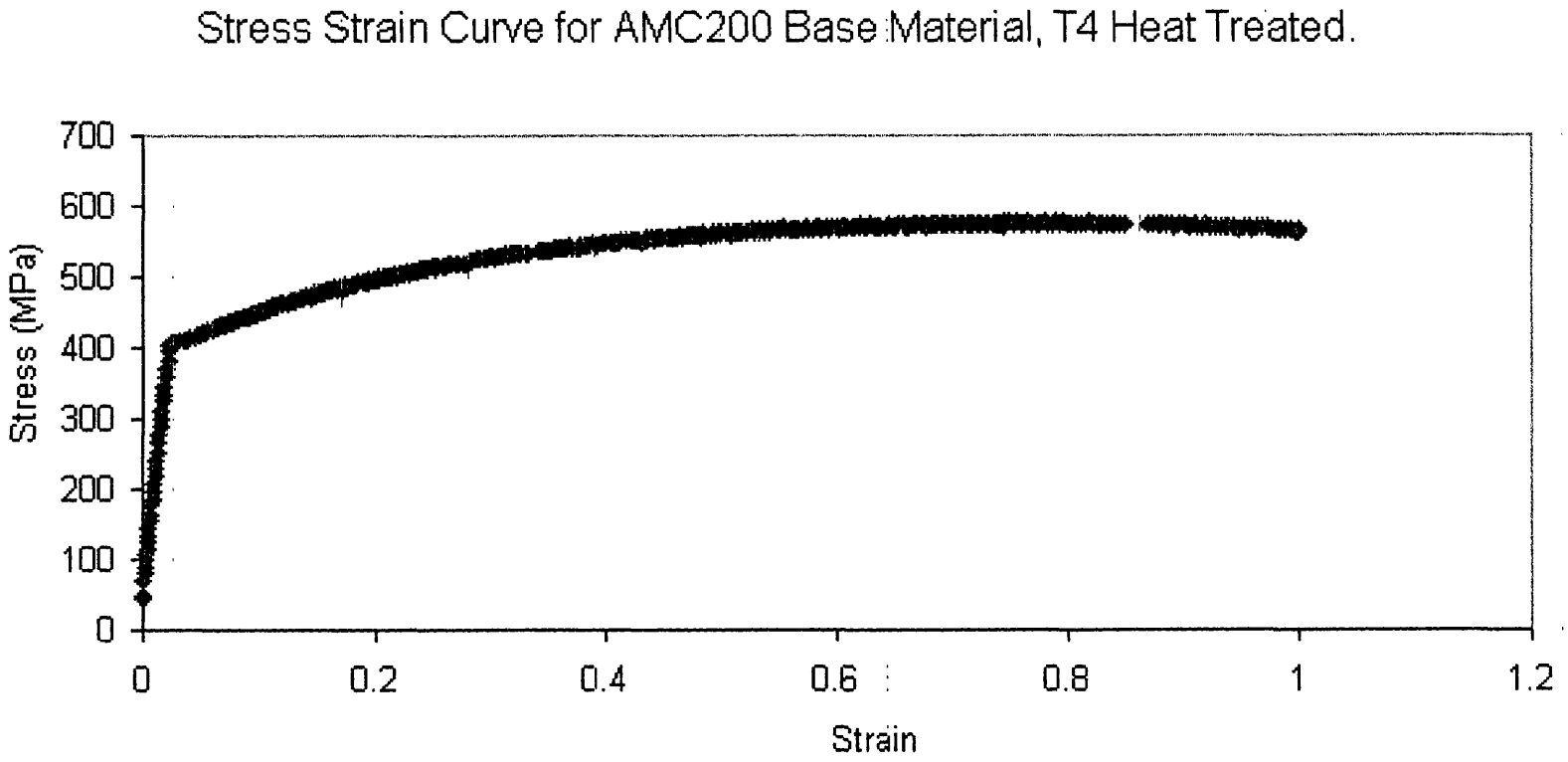

Appendix 1. Figure 1b.

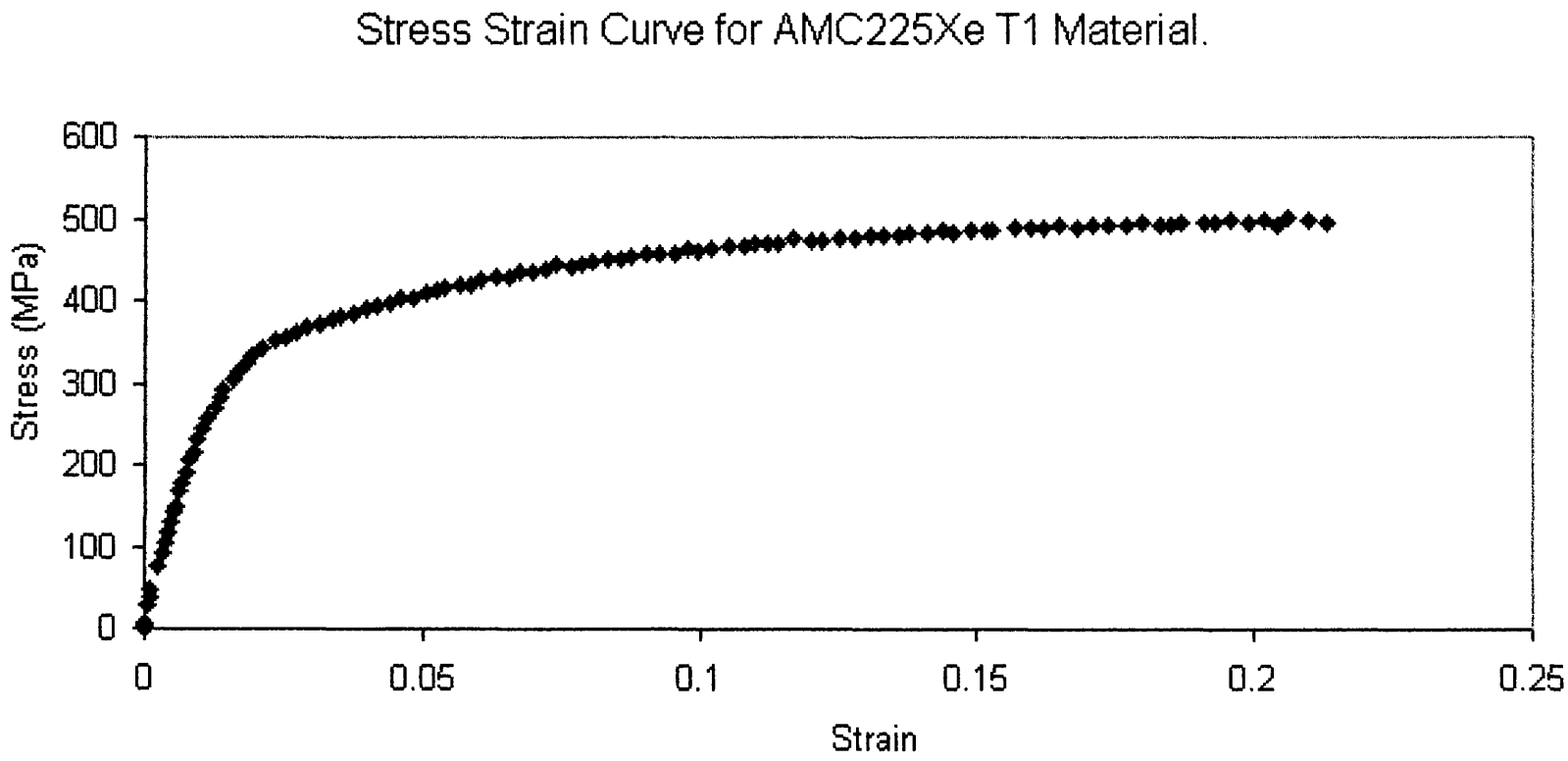

Appendix 1. Figure 1c.

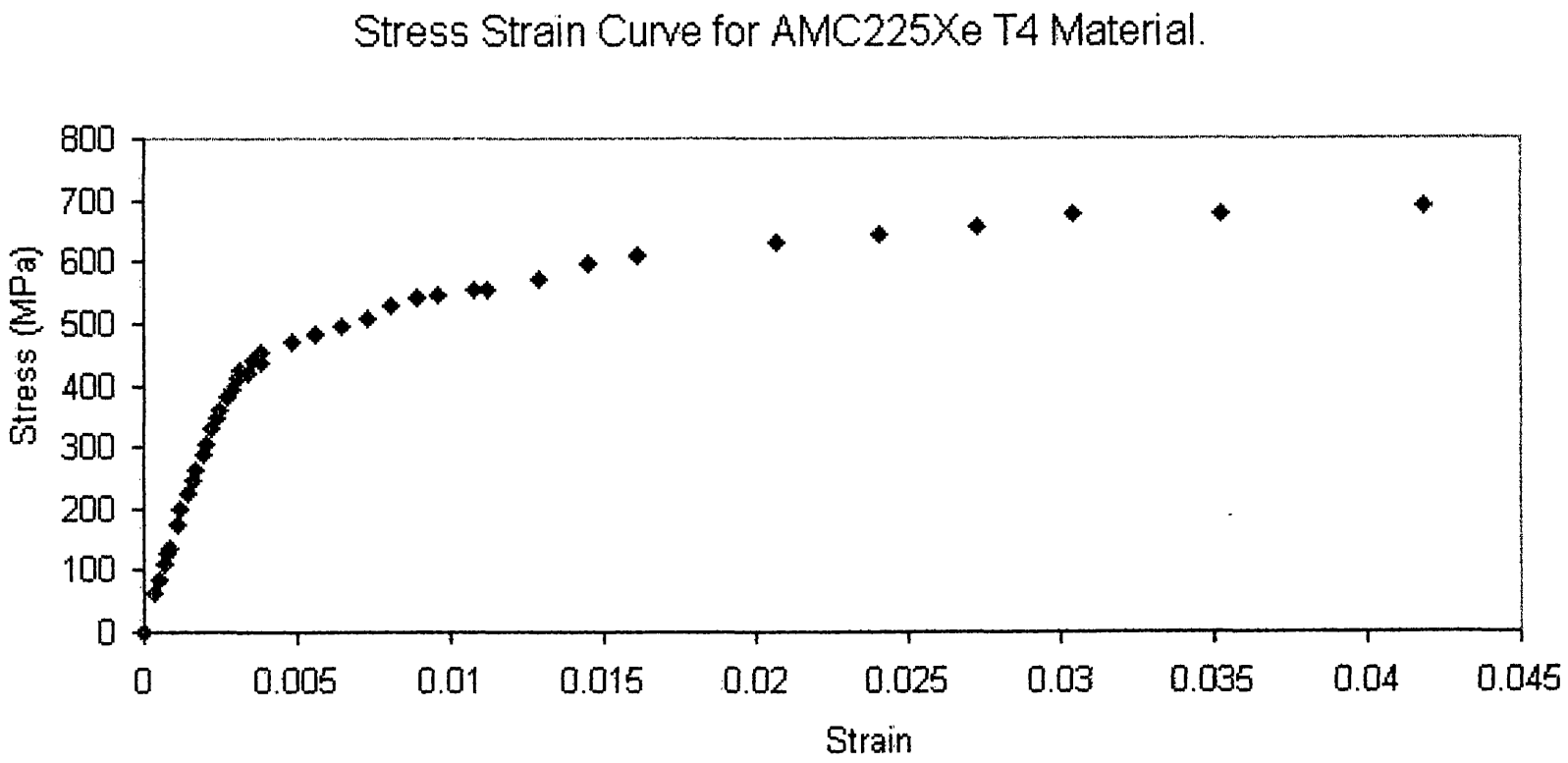

Appendix 1. Figure 1d.

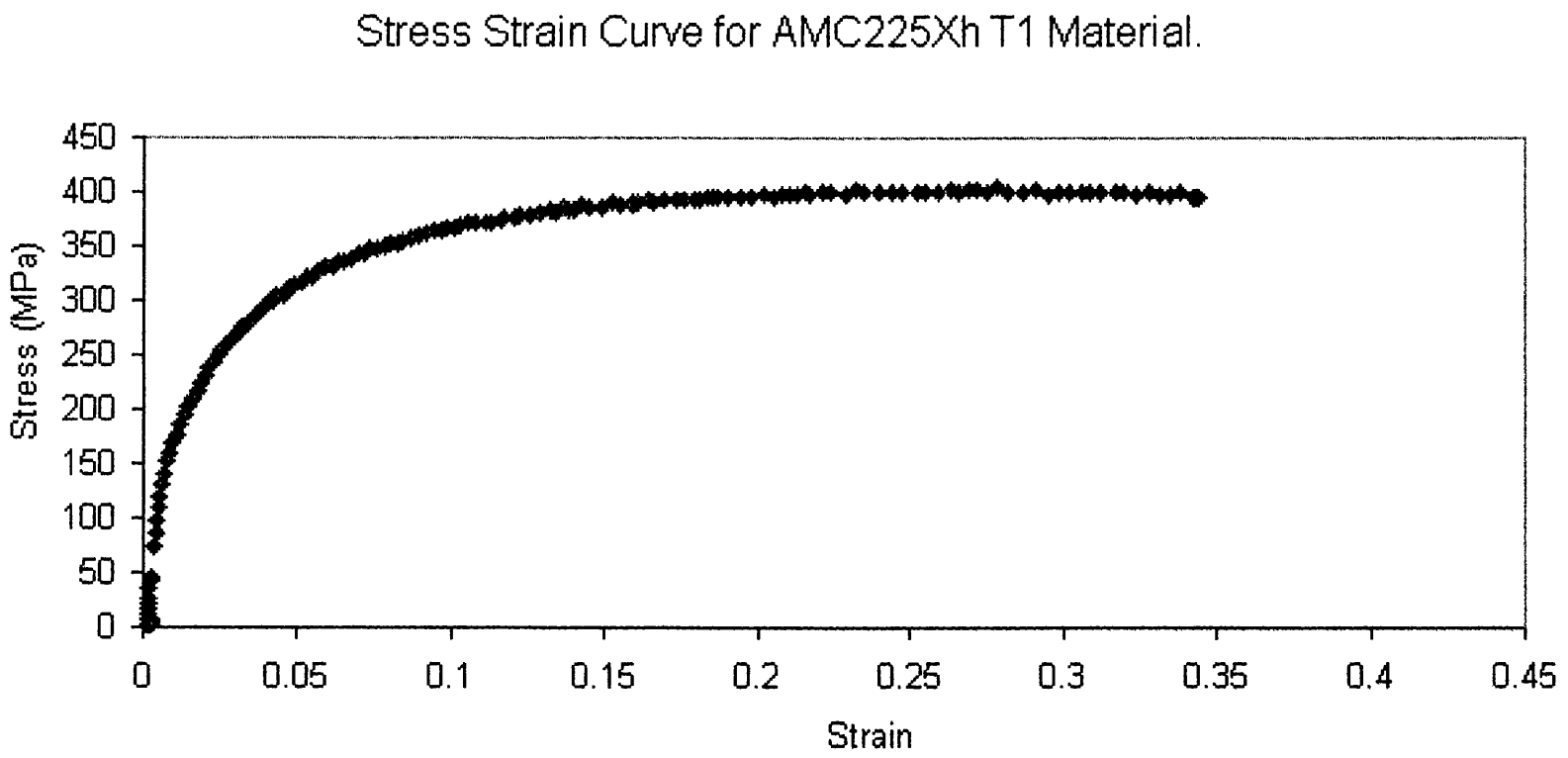

Appendix 1. Figure 1e.

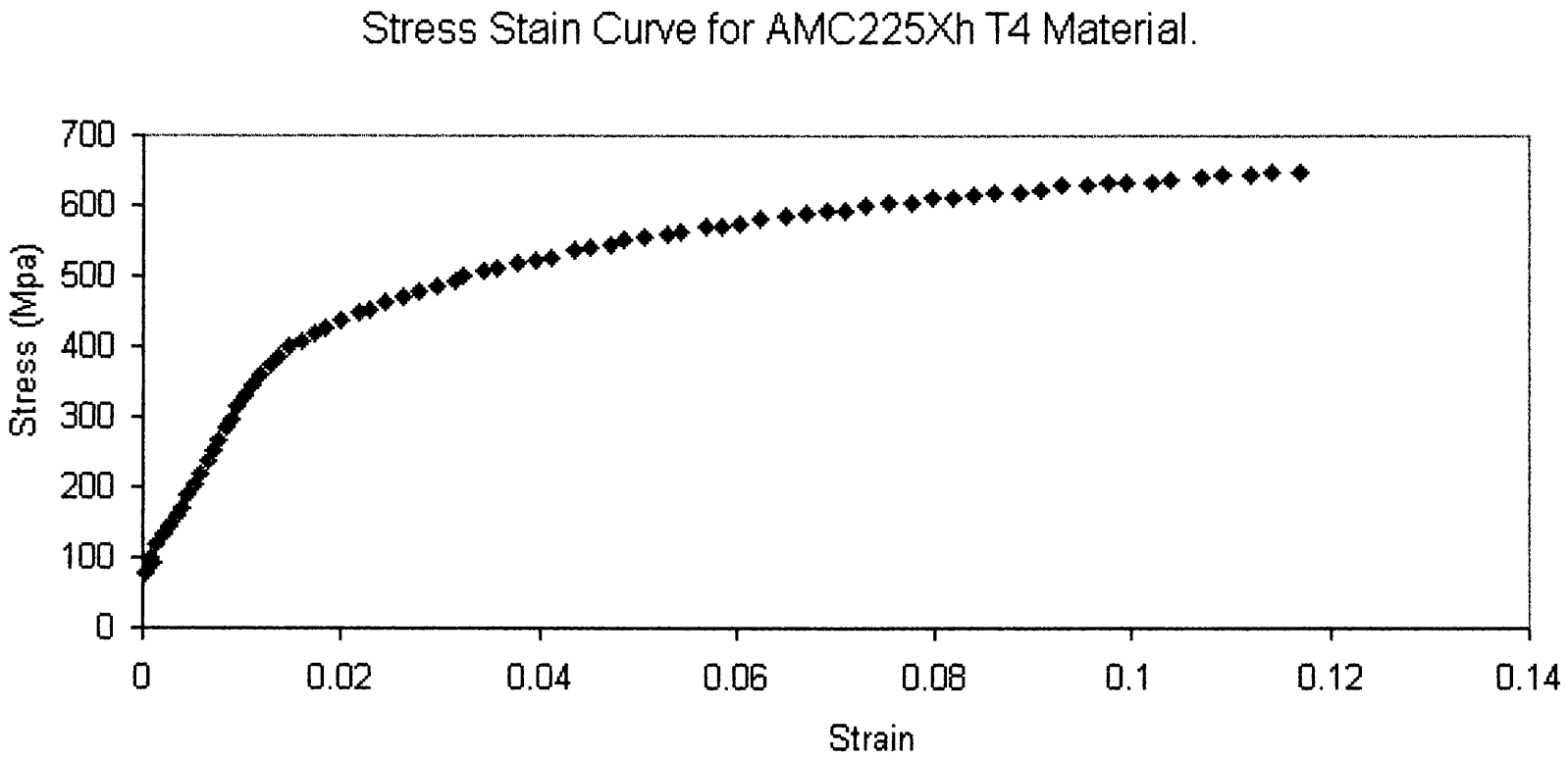

Appendix 1. Figure 1f.

Acknowledgements.

This work has been supported with EPSRC and MOD funding. Supervision of the programme by Dr Alan Shakesheff of the Structural Materials Centre, DERA, Farnborough is warmly acknowledged.

Professor John Evans as supervisor within the IRC Swansea, Martin Bache and Veronica are thanked for their time, expert advise and help in solving logistic problems and others.

Thanks to my family, especially my parents, for emotional support through the last three years and a special thanks to Daniel Shields for his patience and all round support in my final year (and the rest!!).

Bless the kids and pray they don't hold it against me (Abel and Sophie, sorry I haven't seen too much of you the last few months but, needs must!! Love you, honest.).

Just better say a quick sorry to Matthew, just call me Doc! Best of luck!!

19/03/03